From ab-initio thermodynamics to quasi-harmonic thermoelastic properties of crystals: A new workflow and selected applications

CRISTIANO MALICA

Advisor: Prof. Andrea Dal Corso

Inernational School for Advanced Studies

DECEMBER 2021

List of Publications

Journals

1. C. Malica and A. Dal Corso. Quasi-harmonic temperature dependent elastic constants: Applications to silicon, aluminum and silver. J. Phys.: Condens. Matter, **32** 315902 (2020) (Chapter 3 - Section 3.2 and Ref. [1]).

2. C. Malica and A. Dal Corso. Quasi-harmonic thermoelasticity of palladium, platinum, copper, and gold from first principles. J. Phys.: Condens. Matter, **33** 475901 (2021) (Chapter 3 - Section 3.3 and Ref. [2]).

3. C. Malica and A. Dal Corso. Temperature-dependent elastic constants and thermodynamic properties of BAs: An ab-initio investigation. J. Appl. Phys. **127** 245103 (2020) (Chapter 3 - Section 3.4 and Ref. [3]).

4. C. Malica and A. Dal Corso. Paper about finite-temperature atomic relaxations. *In preparation.* (Chapter 4).

5. C. Malica and A. Dal Corso. Temperature-dependent atomic B factor: An ab-initio calculation. Acta Crystallogr. A **75** 624 (2019). (Chapter 5 and Ref. [4]).

International Conferences

1. Poster Presentation: Temperature-dependent atomic B-factor: an ab-initio implementation - 19th International Workshop on Computational Physics and Material Science: Total Energy and Force Methods - ICTP (Italy) - Jan. 2019.

2. Poster Presentation: Temperature dependent elastic constants from first principles - 20th International Workshop on Computational Physics and Materials Science: Total Energy and Force Methods - ICTP virtual meeting (Italy) - Feb. 2021.

3. Oral Presentation: Temperature dependent elastic constants from first principles - APS March Meeting - Online - Mar. 2021.

Acknowledgements

During the years of my PhD I conserved many thanks that now have to be distributed.

First of all I would like to thank my supervisor Andrea who was always present for any kind of problem or discussion. Very precise in his work and, most important, very respectful for the works of others. He is the supervisor that I wish to all students.

Among the professors, in particular, I would like to thank Massimo Capone that was always kind and available for any problem.

Thanks to the people, friends and colleagues who were close to me, especially at the beginning of this experience.

Thanks to all excellent people that have contributed to my musical growth in these years. In particular Alessandra, Giorgio, Gianni, Gianluca. The energy gathered from this activity was really important for the PhD as well. I am also extremely grateful to the jury of the Opera Contest in Villazzano (Trento) who awarded me the first prize, last May.

Thanks to Marcello and Aldo that involved me in two different choirs in Trieste. These experiences allow me to meet many people from Trieste, learn a little bit of *triestino* and sometimes taste the *Teran* wine.

Thanks to Michela better known as Ginevra for her constant presence in these years.

Thanks to my parents and my most preferred uncle Gabriele, always present.

Thanks to Roberta: finally we have the same degree e posso smettere finalmente di darti del lei.

Introduction

Since its birth, density functional theory (DFT) [5] has been a reference point in the physics and chemistry of materials thanks to the development of efficient computational methods to calculate several ground-state properties of materials (at zero temperature), accounting for quantum effects with a modest computational workload. Among these properties, in the present thesis, we will focus on the elastic constants (ECs): they describe the strength of the chemical bonds between atoms and determine other properties such as the crystal stability, the hardness of materials and the speed of sound. DFT has been employed for several decades to estimate the ECs of materials at zero temperature and usually provides values within $\sim 10\%$ of the experiments [6–13].

The subsequent introduction of methods able to evaluate the lattice dynamics of materials, such as density functional perturbation theory (DFPT) [14] and Car-Parrinello molecular dynamics [15], allowed the extension of calculations to finite-temperature properties and, hence, the study of the thermodynamic properties of materials which have not only a significant fundamental interest, but also technological and applicative relevance. As a matter of fact, the nuclei constitute the majority of the mass of materials and their thermal motion determines properties, such as thermal expansion, heat capacity, or thermal conductivity. The theoretical treatment of the lattice vibrations is commonly based on the so-called harmonic approximation (HA) which assumes a parabolic dependence of the atomic potential on atomic displacements. This approximation is not sufficient to treat all physical properties, some of which are intrinsically anharmonic, i.e. due to the non-parabolic regions of the interatomic potential. For instance, the HA gives vanishing thermal expansion in solids. The anharmonic effects can be studied within the so-called quasi-harmonic approximation (QHA) for which the vibrational frequencies acquire a volume dependence (or, more generally, a dependence on the crystal parameters). The use of the QHA combined with the *ab-initio* methods (based on DFT) has demonstrated a remarkable effectiveness in the description of the thermodynamic properties at temperature not too close to the melting point were higher-order anharmonic effects start to be important (approximately until $\frac{2}{3}T_M$ where T_M is the

melting temperature [16]). At increasing pressures, the melting temperature increases as well: this extends the validity range of the QHA which becomes a valuable method to recover information about materials at conditions of temperature and pressures difficult or impossible to reach in experiments. The QHA has been applied in numerous fields: semiconductors and insulators, simple metals, hydrides, intermetallics, surfaces, and Earth materials of special interest in geophysics. Some of the most important works are summarized in Ref. [17]. The QHA is also a primary instrument for the study of materials which exhibit a negative thermal expansion [18]. See also the more recent works [19, 16] for the use of the QHA on thermodynamic properties. Several methods including the anharmonic effects beyond the QHA were also proposed [20, 21].

DFT ground-state properties such as electronic band structures, elastic properties at $T = 0$ K, and phonon dispersions have been computed and cataloged in large databases [22, 23]. To this end the so-called high-troughput methods are often used. They make simultaneous calculations of these properties for a large number of samples. This is possible also thanks to libraries of pseudopotentials [24–27] which allow to study different atomic species and functionals. Then, these databases are used to identify the best candidates which satisfy the required properties for the desired applications. Among all the calculated properties the thermodynamic ones are less extensive because they require more expensive calculations of lattice vibrations. However, some studies for metals and alloys needed for the comprehension of industrial and technological processes have been done within approximate methods [23, 28–30].

With the increase in power and number of CPUs of the modern computers, the thermodynamic calculations are becoming more affordable and common for a large class of materials, from isotropic crystals (with one lattice parameter) to the anisotropic crystals (with more lattice parameters) allowing the optimization of the properties at finite-temperature by considering the contribution due to the temperature dependence of all crystal parameters. However, until a few years ago well-defined workflows and codes providing directly such properties did not exist. Sometimes, the use of several programs, often complex, is required, and a big effort in the post-production stage is also required to arrive at the final result. This is especially true for the calculation of the temperature dependent elastic constants where the DFT

and phonon calculations have to be set in many strained configurations which increase with the complexity of the crystal. Hence, it is necessary to find a solution which, at the same time, automate the calculation, makes it simpler (accessible to non-specialists) and capable to take full advantage of the CPU resources available now and in the future, also in view of a possible high-throughput use.

One of the instruments which is under development, in this respect, for the calculation of the thermodynamic properties of materials is the `thermo_pw` [31] code. It is a driver of the `Quantum ESPRESSO` [32, 33] routines which exploits the basic parallelization levels of the latter adding a further level based on the so-called images that distribute the calculations for the different geometries on different CPUs and are also able to communicate with each other asynchronously to receive the next task to execute at the completion of the previous one. The program allows the calculation of numerous thermodynamic properties within the QHA with a simple definition of the variables for the control of the workflows and produces plots comparable with experiments. Recently, it has been used for the calculation of ECs at $T = 0$ K [34] and for the investigation of a few thermodynamic properties in hexagonal close-packed (h.c.p.) metals [35, 36]. Another similar workflow was recently presented [37].

In this thesis we present the general scheme of operation of `thermo_pw`, extending the calculation to the temperature dependent elastic constants. In particular, we investigate the two main methods present in the literature, both based on lattice-dynamics calculations. The quasi-static approximation (QSA) requires the calculation of the ECs at $T = 0$ K for various volumes and includes the effect of the variation of volume (or crystal parameters) due to the thermal expansion computed within the QHA. The QSA has been largely used in the literature. For example, Y. Wang *et al.* computed the TDECs of seven cubic metals [38] and S-L. Shang *et al.* [39] computed TDECs of α- and θ-Al_2O_3. K. Kádas *et al.* [40] used the same approximation for the TDECs of α-beryllium deriving the temperature dependence of the volume from the Debye model. The second approach consists in the use of the QHA to compute the ECs directly at finite-temperature (from the second derivatives of the Helmholtz free-energy with respect to strain). This method has been applied, for instance, to the TDECs of MgO [41], h.c.p. beryllium, cubic diamond and lonsdaleite [42], α-iron [43] and Fe_3Ga alloys [44]. Some other important works

are reported in Ref. [17]. We will compare the TDECs computed within the two approximations. Then, since the ECs enter in the thermal expansion of solids (when computed via mode-Grüneisen parameters), we will use the TDECs to compute it and compare the results with the thermal expansion obtained from the $T = 0$ K ECs, an approximation widely used in the literature. This study will be applied to Si, Al, and Ag.

In metals, the electronic excitations might give a non-negligible contribution to the thermodynamic properties. In this thesis we will also address this effect for the thermodynamics and TDECs of four elemental solids: Pd, Pt, Cu and Au. Moreover, since so far the effect of the exchange and correlation functional on the TDECs has not been addressed in detail, we do also a systematic comparison between the local density approximation (LDA) and the generalized gradient approximation (GGA) on the same metals Pd, Pt, Cu and Au.

In order to compute the ECs within the QHA we have to consider many deformed configurations which modify the bonds between atoms by changing their position. In some cases the atomic positions obtained by a uniform strain of the atomic coordinates are not equilibrium positions. Hence, it is necessary to allow the atomic coordinates to relax in the new equilibrium positions. In the calculations reported so far in the literature, the atoms are sometimes kept fixed in the uniformly strained positions introducing errors in the ECs. More often, the atoms are allowed to relax at $T = 0$ K by minimizing the total energy and these relaxations are used at all temperatures, neglecting the contribution of finite-temperature to the relaxation. This last contribution was primarily taken into account [45, 46] by estimating the derivatives of the free-energy with respect to internal displacements analytically. In this thesis we will estimate the effect of both approximations by computing the contribution to the ECs of the atomic relaxations at zero and finite temperatures, by arranging the atoms in the position that minimizes the energy and the free-energy, respectively. We will study this effect in two materials that present internal relaxations: Si and BAs.

The next chapters are divided as follows. Chapter 1 is a brief summary of the fundamental methods used, namely DFT for the calculation of the ground-state properties and density functional perturbation theory (DFPT) for the calculation of atomic vibrations. Only fundamental concepts are introduced focusing on the

methodological questions that are relevant for setting the computational parameters. Chapter 2 is an introduction to the thermodynamics of crystals and to the QHA. Chapter 3 presents the implementation of the calculation of the temperature dependent elastic constants in the `thermo_pw` code, showing the general workflow used to compute them and the other thermodynamic properties within the QHA. Then, some applications are presented on the elemental crystals Si, Al, Ag, Pd, Pt, Cu, Au and BAs. Chapter 4 deals with the problem of the finite-temperature atomic relaxations and how it affects the values of the TDECs of Si and BAs.

In Chapter 5, we will leave the discussion of the ECs and we consider another thermodynamic property of general interest: the mean square atomic displacements, or atomic B-factors (BFs). The BFs account for the effects of temperature and quantum fluctuations on the lattice dynamics and defines the Debye-Waller factor which, in turn, explains the temperature dependence of the intensities of X-ray or neutron diffraction peaks in crystallography. These quantities are generally computed at fixed geometry within the HA. We will test this approximation by comparing with the QHA for some elemental crystals. Since also for the BFs, the knowledge of the effect of the exchange and correlation functionals is rather limited we will present a systematic comparison of BFs computed with different functionals.

Finally, a few appendixes discuss some points relevant for the thesis that would make the text too long. Appendix A discuss the theory of elastic constants under a general stress. Appendix B includes the results for the zero-temperature ECs of some materials compared with the literature values. Appendix C reports examples of tests to converge the calculation of ECs. Finally, Appendix D reports a study of the anisotropic thermal expansion at finite pressure.

Contents

Abbreviations

APE	**A**rea **P**ercentage **E**rror
BF	**B** **F**actor
DFT	**D**ensity **F**unctional **T**heory
DFPT	**D**ensity **F**unctional **P**erturbation **T**heory
EC	**E**lastic **C**onstant
GGA	**G**eneralized **G**radient **A**pproximation
LDA	**L**ocal **D**ensity **A**pproximation
PAW	**P**rojector **A**ugmented **W**ave
QHA	**Q**uasi **H**armonic **A**pproximation
QSA	**Q**uasi **S**tatic **A**pproximation
TDEC	**T**emperature **D**ependent **E**lastic **C**onstant
TE	**T**hermal **E**xpansion

Chapter 1

Theoretical framework

In the present chapter we present the technique used in this thesis to compute the electronic ground state properties: Density-functional theory (DFT). DFT is a quantum mechanical approach used in physics as well as in chemistry and materials science to investigate the electronic structure of many-body systems, in particular atoms, molecules, and the condensed phases that focuses on the electron density and the ground-state energy instead of the many-body wavefunctions. It was originally formulated by Walter Kohn (1923-2016) which was awarded of the Nobel prize in Chemistry in 1998. In the second part of this chapter, we will discuss the method used to compute the vibrational properties of materials: Density-functional perturbation theory (DFPT). These two ingredients are finally coupled to statistical mechanics methods in the next chapter to address the thermodynamic properties of materials.

1.1 Density-functional theory

Within the *adiabatic approximation* the electronic and nuclear dynamics can be decoupled because the nuclear masses are much larger than the electronic ones, and the many-body wavefunction is factored in the electronic and nuclear parts. The many-body Schrödinger equation can be solved for the electrons in the external potential of the nuclei. The electronic wavefunction depends explicitly on the electronic positions while the nuclear coordinates enter as external parameters, and the ground-state energy of the electrons acts as the potential in the nuclear equation.

Let us consider a system with N_{el} interacting electrons in the potential of the nuclei. The quantum mechanical properties of the system are obtained by solving the many-body Schrödinger equation:

$$\hat{H}\psi(\mathbf{r}_1, ..., \mathbf{r}_{N_{el}}) = E\psi(\mathbf{r}_1, ..., \mathbf{r}_{N_{el}}), \tag{1.1}$$

with the Hamiltonian:

$$\hat{H} = -\sum_{i=1}^{N_{el}} \frac{\hbar^2}{2m}\nabla_i^2 + \sum_{i=1}^{N_{el}} V_{ext}(\mathbf{r}_i) + \frac{e^2}{8\pi\epsilon_0}\sum_{i\neq j}\frac{1}{\mid \mathbf{r}_i - \mathbf{r}_j \mid}, \tag{1.2}$$

where $\mathbf{r}_i$ is the position of electron i, ∇_i^2 is the Laplacian with respect to the coordinate $\mathbf{r}_i$ and $V_{ext}(\mathbf{r}_i)$ is the external potential acting on electrons that depends parametrically on the nuclear positions, ϵ_0 is the vacuum permittivity. The Eq. 1.2 is written according to the international system of units, however, electronic structure codes adopt atomic units (a.u.). In a.u. the unit of length is the Bohr radius ($a_B = 5.29177210903\times10^{-11}$ m), the unit of energy is the Hartree ($E_h = 4.3597447222072\times 10^{-18}$ J), the unit of mass is the electronic mass ($m = 9.093837015 \times 10^{-31}$ kg) and

the unit of charge is the electronic charge ($e = 1.602176634 \times 10^{-19}$ C). To get Eq. 1.2 in a.u. we have to set $\hbar = 1$, $m = 1$, and $e = 1$. In the following discussion we will always adopt the a.u. system.

The exact solution of Eq. 1.1 exists only for a few systems (such as hydrogen and hydrogen-like systems) while, in order to deal with more complicated systems, it is necessary to use suitable approximations and numerical methods. The DFT is one of these approximations that has been very successful to describe the properties of materials.

DFT was introduced in 1964 by Hohenberg and Kohn [47] who proved a one-to-one correspondence between the ground-state electronic density $\rho(\mathbf{r})$ and the external potential $V_{ext}(\mathbf{r})$. Since the external potential determines the many-body wave function in its ground state, the physical properties of the system in the ground state can be expressed as *functionals* of the charge density. Among these properties the *total ground state energy* of the system is of particular interest. It is the expectation value of the Hamiltonian on the ground state $|\Psi_0\rangle$. By expressing it as a functional of the electronic density we have:

$$E[\rho(\mathbf{r})] = \langle \Psi_0 | \hat{H} | \Psi_0 \rangle = F[\rho(\mathbf{r})] + \int_V V_{ext}(\mathbf{r}) \rho(\mathbf{r}) d^3r. \tag{1.3}$$

$F[\rho(\mathbf{r})]$ includes the kinetic energy and the electronic Coulomb energies, it is an universal functional (i.e. independent on V_{ext}) and its form is in general unknown. The integral is over the whole volume V of the system. The ground-state total energy is given by the minimization of $E[\rho(\mathbf{r})]$ with respect to the electronic density with the constraint of a fixed number of electrons N_{el}:

$$\int_V \rho(\mathbf{r}) d^3r = N_{el}. \tag{1.4}$$

In 1965 Kohn and Sham [5] introduced a suitable form of $F[\rho(\mathbf{r})]$ by introducing an auxiliary system of non-interacting electrons with the same ground-state electron density of the interacting system. If we call $|\psi_i(\mathbf{r})\rangle$ the single-particle wavefunctions of the non-interacting electrons, which are normalized as

$$\langle\psi_i(\mathbf{r})|\psi_j(\mathbf{r})\rangle = \delta_{ij}, \tag{1.5}$$

the electronic density is:

$$\rho(\mathbf{r}) = \sum_i f_i|\psi_i(\mathbf{r})|^2, \tag{1.6}$$

where f_i is the occupation factor for state i. The kinetic energy of the non-interacting electron gas can be written as:

$$T_0 = \sum_i f_i\langle\psi_i(\mathbf{r})| - \frac{1}{2}\nabla^2|\psi_i(\mathbf{r})\rangle, \tag{1.7}$$

and the Hartree term, due to the classical interactions between electrons, as:

$$E_H = \frac{1}{2}\iint_V \frac{\rho(\mathbf{r}_1)\rho(\mathbf{r}_2)}{|\mathbf{r}_1 - \mathbf{r}_2|}d^3r_1 d^3r_2. \tag{1.8}$$

The functional $F[\rho(\mathbf{r})]$ is written in terms of these quantities as:

$$F[\rho(\mathbf{r})] = T_0 + E_H + E_{xc}[\rho(\mathbf{r})], \tag{1.9}$$

where $E_{xc}[\rho(\mathbf{r})] = F[\rho(\mathbf{r})] - T_0 - E_H$ defines the *exchange-correlation energy functional* which includes the many-body interactions not present in the other terms. So, the total energy can be rewritten as:

$$E[\rho(\mathbf{r})] = T_0[\rho(\mathbf{r})] + E_H[\rho(\mathbf{r})] + E_{xc}[\rho(\mathbf{r})] + E_{ext}[\rho(\mathbf{r})], \tag{1.10}$$

where E_{ext} is the integral of the external potential which is, using Eq. 1.6:

$$E_{ext} = \int_V V_{ext}(\mathbf{r})\rho(\mathbf{r})d^3r = \sum_i f_i \langle \psi_i(\mathbf{r})|V_{ext}|\psi_i(\mathbf{r})\rangle. \tag{1.11}$$

Since the electronic wavefunctions are normalized, the total energy can be minimized with the Lagrange multiplier technique. The minimization gives the Kohn-Sham equations [5]:

$$\left[-\frac{1}{2}\nabla^2 + V_{KS}(\mathbf{r})\right] |\psi_i(\mathbf{r})\rangle = \epsilon_i |\psi_i(\mathbf{r})\rangle, \tag{1.12}$$

where V_{KS} is the Kohn-Sham potential. It is a self-consistent mean-field potential that accounts for the external potential V_{ext} of the ions and the interaction with all other electrons. We have:

$$V_{KS}(\mathbf{r}) = V_{ext}(\mathbf{r}) + V_H(\mathbf{r}) + V_{xc}(\mathbf{r}), \tag{1.13}$$

where V_H is the Hartree potential

$$V_H(\mathbf{r}) = \int_V \frac{\rho(\mathbf{r}')}{|\mathbf{r} - \mathbf{r}'|} d^3r', \tag{1.14}$$

and V_{xc} the exchange-correlation potential

$$V_{xc}(\mathbf{r}) = \left.\frac{\delta E_{xc}[\rho]}{\delta \rho}\right|_{\rho=\rho(\mathbf{r})}, \tag{1.15}$$

which is the functional derivative with respect to the electronic density of the exchange-correlation energy, evaluated at the density in the point $\mathbf{r}$.

E_{xc} is not known and an approximation for it has to be specified. One of the most used is the local density approximation (LDA) in which the exchange-correlation energy is:

$$E_{xc}[\rho(\mathbf{r})] = \int_V \epsilon_{xc}^{hom}\left(\rho(\mathbf{r})\right)\rho(\mathbf{r})d^3r \tag{1.16}$$

where $\epsilon_{xc}^{hom}\left(\rho(\mathbf{r})\right)$ is the exchange-correlation energy density of a *homogeneous* electron gas with uniform charge density ρ and, for each point $\mathbf{r}$ is evaluated at the *local* charge density of the non-uniform system $\rho\left(\mathbf{r}\right)$. It has been calculated by Quantum Monte Carlo methods and interpolated with several functional forms. In our LDA calculations we adopt the form proposed by Perdew and Zunger [48].

LDA is efficient in systems with a slowly-varying spatial density but, typically, it overestimates the binding energies and, consequently, the bond lengths are underestimated, phonon frequencies and elastic constants overestimated. An other approach is the generalized gradient approximation (GGA) where the exchange-correlation energy density depends not only on the charge density $\rho(\mathbf{r})$ but also on its gradient $\nabla\rho(\mathbf{r})$ at the point $\mathbf{r}$. The gradient introduces a non-local dependence on $\rho(\mathbf{r})$ and for this reason these functionals are often called *semi-local*. The exchange-correlation energy within GGA is:

$$E_{xc}[\rho(\mathbf{r})] = \int_V \epsilon_{xc}^{GGA}\left(\rho(\mathbf{r}), \nabla\rho(\mathbf{r})\right)\rho(\mathbf{r})d^3r. \tag{1.17}$$

In this thesis, calculations are presented with the GGA functional proposed by Perdew, Burke and Ernzerhof (PBE) [49] and its correction, PBEsol, for densely packed solids [50]. Compared to LDA, PBE provides smaller binding energy, often over-correcting the LDA estimates. Hence, the bond lengths are larger and, tipically,

phonon frequencies and elastic constants underestimated. PBEsol physical properties are generally located between LDA and PBE estimates often giving a better agreement with experiment for densely packed solids.

1.1.1 Self-consistent cycle

The effective potential $V_{KS}(\mathbf{r})$ in the Eq. 1.12 depends on the solution of the equation itself through the density 1.6. So, the problem is solved self-consistently, starting from an initial guess of the density $\rho^0_{in}(\mathbf{r})$ (for instance, from a superposition of atomic densities) which determines, in turn, the potential 1.13. Then, the Kohn-Sham Hamiltonian 1.12 is diagonalized giving a new set of wavefunctions and a new density $\rho^0_{out}(\mathbf{r})$. From a linear combination of $\rho^0_{in}(\mathbf{r})$ and $\rho^0_{out}(\mathbf{r})$, a new tentative density $\rho^1_{in}(\mathbf{r})$ and, consequently, a new V_{KS} are generated. The Kohn-Sham Hamiltonian is diagonalized again to obtain $\rho^1_{out}(\mathbf{r})$ and the procedure is iterated until the quantity

$$\int_V |\rho^n_{out}(\mathbf{r}) - \rho^n_{in}(\mathbf{r})|^2 d^3r, \tag{1.18}$$

at the n-th iteration, gets below a given accuracy threshold.

1.1.2 Periodic solids and plane waves

We consider an extended three-dimensional crystal made by N cells with N_{at} atoms in the unit cell. The nuclei in crystals are arranged periodically in space, their equilibrium positions are:

$$\mathbf{R}_I = \mathbf{R}_\mu + \mathbf{d}_s, \tag{1.19}$$

$\mathbf{R}_\mu$ indicates a Bravais lattice vector

$$\mathbf{R}_\mu = n_1\mathbf{a}_1 + n_2\mathbf{a}_2 + n_3\mathbf{a}_3, \tag{1.20}$$

where the $\mathbf{a}_1$, $\mathbf{a}_2$ and $\mathbf{a}_3$ are three linearly independent vectors forming the basis of the considered Bravais lattice and n_1, n_2 and n_3 are three integer numbers identifying a site of the lattice. The vector $\mathbf{d}_s$ is specified by

$$\mathbf{d}_s = d_{1s}\mathbf{a}_1 + d_{2s}\mathbf{a}_2 + d_{3s}\mathbf{a}_3, \tag{1.21}$$

where $0 \leq d_{is} < 1$ are the fractional coordinates. The volume of the unit cell is given by:

$$\Omega = \mathbf{a}_1 \cdot (\mathbf{a}_2 \times \mathbf{a}_3). \tag{1.22}$$

The potential of the nuclei V_{ext} has the same periodicity of the Bravais lattice:

$$V_{ext}(\mathbf{r} + \mathbf{R}) = V_{ext}(\mathbf{r}). \tag{1.23}$$

The electronic charge density arranges around the nuclei following the same periodicity and, hence, also V_{KS} shows the same periodicity:

$$\begin{aligned} \rho(\mathbf{r} + \mathbf{R}) &= \rho(\mathbf{r}), \\ V_{KS}(\mathbf{r} + \mathbf{R}) &= V_{KS}(\mathbf{r}). \end{aligned} \tag{1.24}$$

Therefore, the Bloch theorem allows us to write the single-particle wavefunctions as:

$$\psi_{\mathbf{k}v}(\mathbf{r}) = e^{i\mathbf{k}\cdot\mathbf{r}} u_{\mathbf{k}v}(\mathbf{r}), \tag{1.25}$$

where $u_{\mathbf{k}v}(\mathbf{r})$ are lattice periodic functions, v is the band index and $\mathbf{k}$ is a three-dimensional vector defined in the reciprocal space. With the *Born-von Kármán* periodic boundary conditions (PBCs), the solid is modeled as a system consisting of N_j unit cells in the direction of the lattice vectors $\mathbf{a}_j$ where $j = 1, 2, 3$:

$$\psi_{\mathbf{k}v}(\mathbf{r} + N_j\mathbf{a}_j) = \psi_{\mathbf{k}v}(\mathbf{r}). \tag{1.26}$$

Imposing the PBCs to the wavefunctions 1.25 we have:

$$e^{iN_j\mathbf{k}\cdot\mathbf{a}_j} = 1, \tag{1.27}$$

implying a finite set of allowed $\mathbf{k}$ vectors:

$$\mathbf{k} = \sum_{j=1}^{3} \frac{m_j}{N_j}\mathbf{b}_j, \tag{1.28}$$

where m_j are integer numbers such that $0 \leq m_j < N_j$. The $\mathbf{b}_j$ are the primitive vectors of the reciprocal lattice such that $\mathbf{a}_i \cdot \mathbf{b}_j = 2\pi\delta_{ij}$. The reciprocal lattice of a crystal is a Bravais lattice defined by the lattice vectors:

$$\mathbf{G} = n_1\mathbf{b}_1 + n_2\mathbf{b}_2 + n_3\mathbf{b}_3. \tag{1.29}$$

The unit cell of the reciprocal Bravais-lattice is the Brillouin zone where the $\mathbf{k}$ vectors are confined. If $N = N_1N_2N_3$ is the total number of cells in the crystal then we have the same number of $\mathbf{k}$ vectors inside the Brillouin zone. The number of occupied bands depends on the number of electrons per unit cell N_{el}: $N_{el}/2$ bands are sufficient for a non-magnetic insulator while for metals more bands have to be computed and occupation numbers must be introduced. If $u_{\mathbf{k}v}$ is expanded in plane

waves then the wavefunctions read as:

$$\psi_{\mathbf{k}v}(\mathbf{r}) = \frac{1}{\sqrt{V}} \sum_{\mathbf{G}} c_{\mathbf{k}+\mathbf{G},v} e^{i(\mathbf{k}+\mathbf{G})\cdot\mathbf{r}}, \tag{1.30}$$

where $\mathbf{G}$ is a reciprocal lattice vector and the plane wave coefficients $c_{\mathbf{k}+\mathbf{G},v}$ are normalized:

$$\sum_{\mathbf{G}} |c_{\mathbf{k}+\mathbf{G},v}|^2 = 1. \tag{1.31}$$

If we insert the wavefunctions 1.30 into the Kohn-Sham equation 1.12 we get the eigenvalue problem:

$$\sum_{\mathbf{G}} \left[\frac{1}{2} |\mathbf{k}+\mathbf{G}|^2 \delta_{\mathbf{G}\overline{\mathbf{G}}} + V_{KS}(\mathbf{G}-\overline{\mathbf{G}}) \right] c_{\mathbf{k}+\overline{\mathbf{G}},v} = \epsilon_{\mathbf{k}v}\ c_{\mathbf{k}+\mathbf{G},v} \tag{1.32}$$

where $V_{KS}(\mathbf{G})$ is the Fourier transform of the Kohn-Sham potential:

$$V_{KS}(\mathbf{G}) = \frac{1}{V} \int_V V_{KS}(\mathbf{r}) e^{-\mathbf{G}\cdot\mathbf{r}} d^3r \tag{1.33}$$

over the volume V of the crystal. The solutions of 1.32 can be obtained by linear algebra routines which give the coefficients of the wavefunctions 1.30. In principle the sum over the $\mathbf{G}$ vectors is infinite but in practical calculations a finite number of $\mathbf{G}$ vectors is chosen by introducing a cut-off for the kinetic energy:

$$\frac{1}{2} |\mathbf{k}+\mathbf{G}|^2 \leq E_{cut}. \tag{1.34}$$

If written in Rydberg units, the previous equation (without the factor $\frac{1}{2}$) describes a sphere in reciprocal space, centered in the $\mathbf{k}$ point with radius $\sqrt{E_{cut}}$. Only the $\mathbf{G}$-vectors inside the sphere are considered in the calculation. The electronic density

can be rewritten by inserting the plane-wave expansion of wavefunctions 1.30 into Eq. 1.6. We obtain:

$$\rho(\mathbf{r}) = \frac{1}{V}\sum_{\mathbf{k}v}\sum_{\mathbf{G}\overline{\mathbf{G}}} f_{\mathbf{k}v} c^*_{\mathbf{k}+\overline{\mathbf{G}},v} c_{\mathbf{k}+\mathbf{G},v} e^{i(\mathbf{G}-\overline{\mathbf{G}})\cdot\mathbf{r}}, \tag{1.35}$$

if $\overline{\mathbf{G}} = -\mathbf{G}$ we get the maximum possible reciprocal vector $2\mathbf{G}$ for the electronic charge density. Hence, the radius of the cutoff-sphere for the charge density $\sqrt{E^{\rho}_{cut}}$ will be doubled with respect the one for the wave-functions: $\sqrt{E^{\rho}_{cut}} = 2\sqrt{E_{cut}}$ and the charge-density energy cutoff itself will be four times the one for the wave-functions.

In electronic structure calculations a finite mesh of **k**-points has to be defined in order to perform various integrals over the Brillouin zone that define usually the physical properties of interest. Such sums are typically performed in a subset of **k**-points that are not equivalent by rotations and each point must acquire a weight that is proportional to the number of **k**-points in the star of equivalent points in the Brillouin zone. This subset of inequivalent points defines the irreducible Brillouin zone (IBZ). The **k**-points grid as well as the variable E_{cut} has to be converged for each property of interest.

1.1.3 Smearing for metals

In metals the occupation factors in Eq. 1.6 are:

$$f_i \rightarrow f_{\mathbf{k}v} = \theta(\epsilon_F - \epsilon_{\mathbf{k}v}) \tag{1.36}$$

where θ is a step function which is 0 if the eigenvalues $\epsilon_{\mathbf{k}v}$ are larger then the Fermi energy ϵ_F, 1 otherwise. So, only the occupied states are included. The Fermi energy can be determined by the condition:

$$2\sum_{\mathbf{k}v}\theta(\epsilon_F-\epsilon_{\mathbf{k}v})=NN_{el}, \tag{1.37}$$

which gives the total number of electrons in the N unit cells of the solid. In the self consistent procedure, the step function could be a source of problems. For example, in consecutive iterations the eigenvalues close to ϵ_F could be slightly above or slightly below ϵ_F itself. This implies a sudden change of the charge density making the calculation unstable. To avoid this problem, the step function is replaced by a smeared function that depends on a smearing parameter σ. In this way the value 1 of the function under ϵ_F, is smoothly connected with the value 0 of the function above ϵ_F. This change takes place in a region of size σ. It follows that the charge density as well as the total energy will depend on σ and the result of interest is obtained in the limit $\sigma\to 0$. There are many recipes for the form of the smoothed step function that allow to use a σ as large as possible and, hence, a small number of $\mathbf{k}$ points giving the result corresponding to the zero broadening limit. The simplest way is to introduce the occupation factor:

$$f_{\mathbf{k}v}=\frac{1}{2}\left[1-\mathrm{erf}\left(\frac{\epsilon_{\mathbf{k}v}-\epsilon_F}{\sigma}\right)\right], \tag{1.38}$$

given by $\int_{-\infty}^{\epsilon_F}\tilde{\delta}(x-\epsilon_{\mathbf{k}v})dx$ where $\tilde{\delta}$ is a gaussian with variance σ. Unfortunately, this approach gives a total energy quadratic with σ, requiring a quite small σ and, hence, a large grid of $\mathbf{k}$-points to converge the calculation. A more efficient method is the one proposed by Methfessel and Paxton [51] giving a total energy quartic in σ. They corrected the previous method multiplying the gaussian by a Hermite polynomial of order one: in this way, even for large σ, the zero broadening limit is obtained with a smaller grid of $\mathbf{k}$-points. Another approach is to use the Fermi-Dirac distribution for the occupation factor. The smearing parameter in this case is the broadening

due to the electronic temperature. The Fermi-Dirac occupations are:

$$f_{\mathbf{k}v} = \left[\exp\left(\frac{\epsilon_{\mathbf{k}v} - \epsilon_F}{k_B T}\right) + 1\right]^{-1}. \tag{1.39}$$

In this case, the charge density $\rho(\mathbf{r}, T)$ acquires the temperature dependence of the Fermi-Dirac occupations. It enters in the self-consistent cycle, determines the Hamiltonian and thus the wavefunctions $\psi_{\mathbf{k}v} = \psi_{\mathbf{k}v}[\rho(\mathbf{r}, T)]$.

When the smearing approach is used, an auxiliary electronic free-energy at temperature T is minimized instead of the total energy alone:

$$F^{el}(T) = E^{el}(T) - TS^{el}(T), \tag{1.40}$$

where E^{el} is the total energy and S^{el} is the auxiliary electronic entropy. When the Fermi-Dirac occupations are used, Eq. 1.40 represents the physical free-energy of the electrons and the smearing parameter in Eq.1.39 $\sigma_{FD} = k_B T$, where k_B is the Boltzmann constant, is related to the physical broadening at temperature T. For sufficiently small smearing, the zero temperature limit can be obtained. In the next chapter we will address another method to compute the electronic free-energy for finite range of temperatures combining DFT band structure calculations and the Sommerfeld method.

1.1.4 Pseudopotentials

The treatment of all the electrons in the calculation require a very large number of plane waves in order to describe the rapid oscillations of the wavefunctions near the nuclei. This problem can be avoided freezing the core electrons in their atomic

ground state and considering only the valence electrons which are those that determine the chemical bonds. For this purpose the concept of *pseudopotential* is introduced to describe the interactions between valence electrons and *pseudoions* formed by the nuclei and the core electrons. The corresponding pseudo-wavefunctions $|\tilde{\psi}_{\mathbf{k}v}\rangle$ of valence electrons are considerably smoother near the nucleus but reproduce the behaviour of the real wavefuntions outside the core region. Many methods have been developed to generate pseudopotentials. They provide additional terms in the density, in the energy and in the Kohn-Sham equations that we will not discuss in details. We mention only that in the ultra-soft (US) pseudopotentials the charge density has the following form:

$$\rho(\mathbf{r}) = \sum_{\mathbf{k}v} f_{\mathbf{k}v} \left[|\tilde{\psi}_{\mathbf{k}v}(\mathbf{r})|^2 + \sum_{Imn} Q^I_{mn}(\mathbf{r}) \langle \tilde{\psi}_{\mathbf{k}v} | \beta^I_m \rangle \langle \beta^I_n | \tilde{\psi}_{\mathbf{k}v} \rangle \right] \tag{1.41}$$

where the new term contains the *augmentation charges* $Q^I_{mn}(\mathbf{r})$ and the projectors $|\beta^I_m\rangle$ of atom I. A similar expression can be derived for pseudopotential within the projector augmented wave (PAW) formalism [52], mainly adopted in this thesis. The additional term in the electronic charge density translates into a E^{ρ}_{cur} larger than $4E_{cut}$. Therefore also E^{ρ}_{cur} is a parameter that enters in the calculation and its convergence must be carefully checked.

1.2 Ab-initio lattice dynamics

Within the adiabatic approximation the nuclei move in a potential energy given by the DFT ground-state total-energy E of the system of electrons with nuclei clamped in their positions $\mathbf{R}_I$. Within the framework of the harmonic approximation we

assume small displacements from the equilibrium positions. If we call the displacement, at time t, $\mathbf{u}_I$ then the position of atom I (i.e. the atom s in the cell μ) becomes:

$$\mathbf{R}_I \rightarrow \mathbf{R}_I + \mathbf{u}_I, \tag{1.42}$$

and we can expand the total-energy up to second order as:

$$E(\mathbf{R}_I + \mathbf{u}_I) = E_0(\mathbf{R}_I) + \sum_{I\alpha} \frac{\partial E}{\partial u_{I\alpha}} u_{I\alpha} + \frac{1}{2} \sum_{I\alpha, J\beta} \frac{\partial^2 E}{\partial u_{I\alpha} \partial u_{J\beta}} u_{I\alpha} u_{J\beta}, \tag{1.43}$$

where the derivatives are computed at $\mathbf{u}_I = 0$ and α and β indicate the three Cartesian coordinates. At equilibrium $\frac{\partial E}{\partial u_{I\alpha}} = 0$ and the Hamiltonian of the ions becomes:

$$H = \sum_{I\alpha} \frac{P_{I\alpha}^2}{2M_I} + \frac{1}{2} \sum_{I\alpha, J\beta} \frac{\partial^2 E}{\partial u_{I\alpha} \partial u_{J\beta}} u_{I\alpha} u_{J\beta}, \tag{1.44}$$

where $P_{I\alpha}$ is the momenta and M_I the mass of the nuclei which, by applying the Hamilton equations ($\dot{u}_{I\alpha} = \frac{\partial H}{\partial P_{I\alpha}}$ and $\dot{P}_{I\alpha} = -\frac{\partial H}{\partial u_{I\alpha}}$), leads to the following equations of motion:

$$M_I \ddot{u}_{I\alpha} = -\sum_{J\beta} \frac{\partial^2 E}{\partial u_{I\alpha} \partial u_{J\beta}} u_{J\beta}, \tag{1.45}$$

with $N \times 3N_{at}$ solutions $u_{I\alpha}(t)$, $3N_{at}$ is the number of modes indicated with the index ν. We look for solutions in the form of a phonon:

$$u_{\mu s\alpha}(t) = \frac{1}{\sqrt{M_s}} \mathrm{Re}\left[u_{s\alpha}^{\nu}(\mathbf{q}) e^{i(\mathbf{q}\mathbf{R}_\mu - \omega_{\mathbf{q}\nu} t)}\right], \tag{1.46}$$

$\omega_{\mathbf{q}\nu}$ is the angular frequency of the lattice vibration at wave vector $\mathbf{q}$ and mode ν, $u^{\nu}_{s\alpha}(\mathbf{q})$ is the complex amplitude of the phonon mode. If we insert Eq. 1.46 into Eq. 1.45 we get:

$$\omega^2_{\mathbf{q}\nu} u^{\nu}_{s\alpha}(\mathbf{q}) = \sum_{s'\beta} D_{s\alpha s'\beta}(\mathbf{q}) u^{\nu}_{s'\beta}(\mathbf{q}) \tag{1.47}$$

where

$$D_{s\alpha s'\beta} = \frac{1}{\sqrt{M_s M_{s'}}} \sum_{\eta} \frac{\partial^2 E}{\partial u_{\mu s\alpha} \partial u_{\eta s'\beta}} e^{i\mathbf{q}(\mathbf{R}_\eta - \mathbf{R}_\mu)} \tag{1.48}$$

is the dynamical matrix of the solid. To compute the second derivatives of the total-energy we can start from the Hellmann-Feynmann theorem which leads to the following expression for the first derivative with respect to the external parameter λ:

$$\frac{\partial E}{\partial \lambda} = \int \frac{\partial V_{ext}}{\partial \lambda} \rho(\mathbf{r}) d^3r + \frac{\partial U_{II}}{\partial \lambda}, \tag{1.49}$$

and derive with respect to a second parameter μ to get the second derivative:

$$\frac{\partial^2 E}{\partial \mu \partial \lambda} = \int \frac{\partial^2 V_{ext}}{\partial \mu \partial \lambda} \rho(\mathbf{r}) d^3r + \int \frac{\partial V_{ext}}{\partial \lambda} \frac{\partial \rho(\mathbf{r})}{\partial \mu} d^3r + \frac{\partial U_{II}}{\partial \lambda \partial \mu}. \tag{1.50}$$

In our case the external parameters λ and μ are the atomic displacements. Eq. 1.50 requires, in addition to the electronic charge density $\rho(\mathbf{r})$, its linear response to a distortion of the nuclear geometry $\frac{\partial \rho(\mathbf{r})}{\partial \mu}$:

$$\frac{\partial \rho(\mathbf{r})}{\partial \mu} = 2 \sum_{i} \left[\frac{\partial \psi^*_{\mathbf{k}v}(\mathbf{r})}{\partial \mu} \psi_{\mathbf{k}v}(\mathbf{r}) + \psi^*_{\mathbf{k}v}(\mathbf{r}) \frac{\partial \psi_{\mathbf{k}v}(\mathbf{r})}{\partial \mu} \right]. \tag{1.51}$$

The derivative $\frac{\partial \psi_{\mathbf{k}v}(\mathbf{r})}{\partial \mu}$ can be evaluated by linearizing the Kohn-Sham potential, the single-particle wavefunctions, and the eigenvalues for a given perturbation μ:

$$
\begin{aligned}
V_{KS}(\mathbf{r},\mu) &= V_{KS}(\mathbf{r},\mu=0) + \frac{\partial V_{KS}}{\partial \mu}\mu \ , \\
\psi_{\mathbf{k}v}(\mathbf{r},\mu) &= \psi_{\mathbf{k}v}(\mathbf{r},\mu=0) + \frac{\partial \psi_{\mathbf{k}v}}{\partial \mu}\mu \ , \\
\epsilon_{\mathbf{k}v}(\mu) &= \epsilon_{\mathbf{k}v}(\mu=0) + \frac{\partial \epsilon_{\mathbf{k}v}}{\partial \mu}\mu.
\end{aligned}
\tag{1.52}
$$

Inserting these equations into the Kohn-Sham equation 1.12 and keeping only the first order in μ we have:

$$
\left[-\frac{1}{2}\nabla^2 + V_{KS}(\mathbf{r}) - \epsilon_{\mathbf{k}v}\right]\frac{\partial \psi_{\mathbf{k}v}(\mathbf{r})}{\partial \mu} = -\frac{\partial V_{KS}}{\partial \mu}\psi_{\mathbf{k}v}(\mathbf{r}) + \frac{\partial \epsilon_{\mathbf{k}v}}{\partial \mu}\psi_{\mathbf{k}v}(\mathbf{r}) \tag{1.53}
$$

where $\frac{\partial V_{KS}}{\partial \mu} = \frac{\partial V_{ext}}{\partial \mu} + \frac{\partial V_H}{\partial \mu} + \frac{V_{xc}}{\partial \mu}$ with

$$
\begin{aligned}
\frac{\partial V_H}{\partial \mu} &= \int \frac{1}{|\mathbf{r}-\mathbf{r}'|}\frac{\partial \rho(\mathbf{r}')}{\partial \mu} d^3r', \\
\frac{\partial V_{xc}}{\partial \mu} &= \frac{\delta V_{xc}}{\delta \rho}\frac{\partial \rho(\mathbf{r})}{\partial \mu},
\end{aligned}
\tag{1.54}
$$

that depend self-consistently on the charge density induced by the perturbation. The induced charge density can be shown to be only dependent on $P_c\frac{\partial \psi_{\mathbf{k}v}}{\partial \mu}$ where P_c is the projector on the conduction bands. Therefore the linear system of Eq. 1.53 can be rewritten as:

$$
\left[-\frac{1}{2}\nabla^2 + V_{KS}(\mathbf{r}) - \epsilon_{\mathbf{k}v}\right]\mathrm{P_c}\,\frac{\partial \psi_{\mathbf{k}v}(\mathbf{r})}{\partial \mu} = -\,\mathrm{P_c}\,\frac{\partial V_{KS}}{\partial \mu}\psi_{\mathbf{k}v}(\mathbf{r}). \tag{1.55}
$$

While the response to the charge density is:

$$
\frac{\partial \rho(\mathbf{r})}{\partial \mu} = 2\sum_{\mathbf{k}v}\left[\left(\mathrm{P_c}\,\frac{\partial \psi_{\mathbf{k}\nu}(\mathbf{r})}{\partial \mu}\right)^* \psi_{\mathbf{k}v}(\mathbf{r}) + \psi^*_{\mathbf{k}v}(\mathbf{r})\,\mathrm{P_c}\,\frac{\partial \psi_{\mathbf{k}v}(\mathbf{r})}{\partial \mu}\right]. \tag{1.56}
$$

Having the response to the charge density, the second derivatives of the energy 1.50 and the dynamical matrix 1.48 can be addressed to compute the phonon frequencies. The above method to obtain the electron-density linear response from DFT is usually referred as density-functional perturbation theory (DFPT). The previous treatment is valid for insulators: further details about it and its modifications for dealing with metals are explained in Ref. [14]. Moreover, the details of the implementation depend upon the given pseudopotential: in this thesis we make use mainly of PAW pseudopotential whose DFPT-extension is given in Refs. [53, 54].

Chapter 2

Elements of thermodynamics of crystals

The knowledge of the total-energy of a solid and of its phonon frequencies allows to model the thermodynamic potentials, i.e. the Helmholtz free-energy from which it is possible to derive several physical properties at finite temperature. These two ingredients are computed within the theoretical frameworks of DFT and DFPT summarized in the previous chapter. Here, we give a general introduction to the basic relations of harmonic and quasi-harmonic thermodynamics.

2.1 Thermal energy of phonons

The energy associated with an harmonic phonon of angular frequency $\omega_{\mathbf{q}\nu}$ of mode ν and reciprocal lattice vector $\mathbf{q}$ depends on the occupation number $n_{\mathbf{q}\nu}$, i.e the number of phonons in that mode, and is given by:

$$E_{\mathbf{q}\nu} = \hbar\omega_{\mathbf{q}\nu}\left[\frac{1}{2} + n_{\mathbf{q}\nu}\right]. \tag{2.1}$$

The complete set of occupation numbers $\{n_{\mathbf{q}\nu}\}$ for each mode describes the state of the system. We indicate a particular state with i: hence, a given index i corresponds to a set $\{n_{\mathbf{q}\nu}\}$. The vibrational energy associated with such a state is indicated with E_i and is the sum of the energies of the occupied phonon states:

$$E_i = \sum_{\mathbf{q}\nu} \hbar\omega_{\mathbf{q}\nu} \left[\frac{1}{2} + n_{\mathbf{q}\nu}\right]. \tag{2.2}$$

From statistical mechanics it is known that at temperature T, the probability $P(E_i)$ of having the system with energy E_i is:

$$P(E_i) = \frac{1}{Z} e^{-\beta E_i}, \tag{2.3}$$

where $\beta = (k_B T)^{-1}$, k_B is the Boltzmann constant and Z is the partition function of the system:

$$Z = \sum_i e^{-\beta E_i} = \prod_{\mathbf{q}\nu} \left(\sum_{n=0}^{\infty} e^{-\beta(n+\frac{1}{2})\hbar\omega_{\mathbf{q}\nu}} \right), \tag{2.4}$$

where in the last equality we make use of Eq. 2.2 and the properties of exponentials. Summing over n and taking the logarithm we have:

$$\ln Z = -\beta \sum_{\mathbf{q}\nu} \frac{\hbar\omega_{\mathbf{q}\nu}}{2} - \sum_{\mathbf{q}\nu} \ln\left[1 - e^{-\beta\hbar\omega_{\mathbf{q}\nu}}\right]. \tag{2.5}$$

The definition of the Helmholtz free-energy is $F = -\frac{1}{N}\frac{1}{\beta}\ln Z$ (where N is the number of unit cells in the crystal): by inserting the vibrational partition function of Eq. 2.5 we get the vibrational free-energy F_{vib}:

$$F_{vib} = \frac{1}{N} \sum_{\mathbf{q}\nu} \frac{\hbar\omega_{\mathbf{q}\nu}}{2} + \frac{1}{N}\frac{1}{\beta} \sum_{\mathbf{q}\nu} \ln\left[1 - e^{-\beta\hbar\omega_{\mathbf{q}\nu}}\right]. \tag{2.6}$$

The internal energy per cell U is defined as the sum of the single state energies E_i

weighted by the probability of each state $P(E_i)$. Considering this definition, Eq. 2.3 and the second side of Eq. 2.4 we have:

$$U = \frac{1}{N}\sum_i E_i P(E_i) = -\frac{1}{N}\frac{\partial \ln Z}{\partial \beta}. \tag{2.7}$$

Hence, the vibrational contribution to the internal energy reads as:

$$U_{vib} = \frac{1}{N}\sum_{\mathbf{q}\nu}\frac{\hbar\omega_{\mathbf{q}\nu}}{2} + \frac{1}{N}\sum_{\mathbf{q}\nu}\frac{\hbar\omega_{\mathbf{q}\nu}}{e^{\beta\hbar\omega_{\mathbf{q}\nu}}-1}, \tag{2.8}$$

which shows that the mean occupation number is:

$$n_{\mathbf{q}\nu} = \frac{1}{e^{\beta\hbar\omega_{\mathbf{q}\nu}}-1}. \tag{2.9}$$

The Eqs. 2.6 and 2.8 can be rewritten in terms of the phonon density of states per cell $g(\omega)$

$$g(\omega) = \frac{1}{N}\sum_{\mathbf{q}\nu}\delta(\omega-\omega_{\mathbf{q}\nu}), \tag{2.10}$$

in the following forms:

$$F_{vib} = \frac{1}{\beta}\int_0^\infty d\omega g(\omega)\ln\left[2\sinh\left(\frac{\beta\hbar\omega}{2}\right)\right], \tag{2.11}$$

$$U_{vib} = \int_0^\infty d\omega g(\omega)\frac{\hbar\omega}{2} + \int_0^\infty d\omega g(\omega)\frac{\hbar\omega}{e^{\beta\hbar\omega}-1}. \tag{2.12}$$

Then the entropy S can be derived from the relation $F = U + TS$.

The internal vibrational energy can be used to calculate the phonon contribution to the isochoric heat capacity $C_V = \left(\frac{\partial U_{vib}}{\partial T}\right)_V$. From Eq. 2.8 we have:

$$C_V = \frac{k_B}{N} \sum_{\mathbf{q}\nu} \left(\frac{\hbar\omega_{\mathbf{q}\nu}}{k_B T}\right)^2 \frac{e^{\beta\hbar\omega_{\mathbf{q}\nu}}}{(e^{\beta\hbar\omega_{\mathbf{q}\nu}} - 1)^2}, \tag{2.13}$$

while by using Eq. 2.12 we have:

$$C_V = k_B \int_0^\infty d\omega g(\omega) e^{\beta\hbar\omega} \left(\frac{\beta\hbar\omega}{e^{\beta\hbar\omega} - 1}\right)^2. \tag{2.14}$$

The previous equations allows to compute the fundamental harmonic thermodynamic properties of solids. In the next section we generalize the expression of the harmonic free-energy in order to get informations about anharmonic properties as the thermal expansion.

2.2 Equilibrium properties from volume-temperature variables

Let us consider a crystal at temperature T, pressure P, and volume Ω. If its volume changes of $d\Omega$, the work done by the solid against the pressure is $-P\ d\Omega$. To keep the temperature T constant, the solid absorbs the heat dQ that, for the second law of thermodynamics, is equal to TdS where dS is the change of entropy. Then from the first law of thermodynamics the change in the internal energy dU is the difference between the absorbed heat and the work done by the solid $dU = TdS - Pd\Omega$. Hence, the pressure must be:

$$P = -\left(\frac{dU}{d\Omega}\right)_T + T\left(\frac{dS}{d\Omega}\right)_T = -\left(\frac{dF}{d\Omega}\right)_T, \tag{2.15}$$

where $F = U + TS$ is the Helmholtz free-energy, a function of the temperature T and the volume Ω. At temperature T and $P = 0$, Eq. 2.15 becomes $\left(\frac{\partial F}{\partial \Omega}\right)_T = 0$, so the solid is in equilibrium at the volume Ω that minimizes the free-energy. Minimizing F at each T we get the temperature dependent volume $\Omega(T)$.

Within the DFT framework the Helmholtz free-energy can be written as

$$F(\Omega, T) = U_0(\Omega) + F_{vib}(\Omega, T) + F_{el}(\Omega, T), \tag{2.16}$$

where $U_0(\Omega)$ is the total-energy of the static lattice (the DFT total-energy) at volume Ω, F_{vib} is the vibrational free-energy of Eq. 2.6 or Eq. 2.11 at the same volume Ω, and F_{el} is the free-energy of the electronic thermal excitation that, until now, we have not considered. This contribution is negligible in insulators and semiconductors but it is often important in metals, in particular for the isobaric heat capacity C_P. In this section we neglect F_{el} but we will address it in Section 2.4. The volume dependence of F_{vib} is determined by means of the QHA for which the phonon normal mode angular frequencies acquire the dependence upon volume $\omega_{\mathbf{q}\nu} \rightarrow \omega_{\mathbf{q}\nu}(\Omega)$.

The variation of a phonon-mode angular frequency with respect to the volume is quantified by the mode-Grüneisen parameter:

$$\gamma_{\mathbf{q}\nu} = -\frac{\Omega_0}{\omega_{\mathbf{q}\nu}} \left(\frac{d\omega_{\mathbf{q}\nu}(\Omega)}{d\Omega}\right)_{\Omega=\Omega_0}, \tag{2.17}$$

where Ω_0 is the equilibrium volume at $T = 0$ K.

2.2.1 Bulk modulus and compressibility

The isothermal bulk modulus B^T is the inverse of the compressibility K^T:

$$\frac{1}{B^T} = K^T = -\frac{1}{\Omega}\left(\frac{\partial\Omega}{\partial P}\right)_T. \tag{2.18}$$

The bulk modulus B as well as its derivatives with respect to pressure B' and the equilibrium volume $\Omega = \Omega_0$ can be obtained as a function of temperature by fitting the Helmholtz free-energy with the Murnaghan equation of state at each temperature, where they enter as fitting parameters:

$$F(\Omega) = F(\Omega_0) + \frac{B\Omega}{B'}\left[\frac{1}{B'-1}\left(\frac{\Omega_0}{\Omega}\right)^{B'} + 1\right] - \frac{B\Omega_0}{B'-1}. \tag{2.19}$$

.

2.2.2 Volume thermal expansion

From $\Omega = \Omega(T)$ we can get the volume thermal expansion at temperature T defined as:

$$\alpha_{vol} = \frac{1}{\Omega}\left(\frac{d\Omega}{dT}\right)_P, \tag{2.20}$$

where P is the pressure.

2.2.3 Thermal expansion from mode-Grüneisen parameters

Starting from Eq. 2.20, the thermal expansion can be written as:

$$\alpha_{vol} = -\frac{1}{\Omega}\left(\frac{d\Omega}{dP}\right)_T\left(\frac{dP}{dT}\right)_\Omega = -\frac{1}{B^T}\left(\frac{\partial^2 F}{\partial T\partial\Omega}\right)_T, \tag{2.21}$$

where we used the definition of the isothermal bulk modulus B^T of Eq. 2.18. By taking the derivatives of Eq. 2.6 with respect T and Ω, α_{vol} becomes:

$$\alpha_{vol} = \frac{1}{B^T} \sum_{\mathbf{q}\nu} c_{\mathbf{q}\nu} \gamma_{\mathbf{q}\nu}, \tag{2.22}$$

where $\gamma_{\mathbf{q}\nu}$ are the mode-Grüneisen parameters of Eq. 2.17 and the $c_{\mathbf{q}\nu}$ are the mode contributions to the heat capacity:

$$c_{\mathbf{q}\nu} = \frac{\hbar\omega_{\mathbf{q}\nu}}{\Omega_0} \frac{\partial}{\partial T} \left(\frac{1}{e^{\beta\hbar\omega_{\mathbf{q}\nu}} - 1} \right). \tag{2.23}$$

2.2.4 Comparison with experiments

Once we have the volume thermal expansion α_{vol} (Eq. 2.20), the heat capacity C_V (Eq. 2.13 or Eq. 2.14) and the isothermal bulk modulus B^T (Eq. 2.18), we can address some properties measured in the experiments. The isobaric heat capacity C_P is given by:

$$C_P = C_V + \Omega B^T \alpha_{vol}^2. \tag{2.24}$$

From the C_P, the isoentropic bulk modulus B^S can be obtained from the isothermal one B^T with the following equation[1]:

$$\frac{1}{B^S} = \frac{1}{B^T} - \frac{T\Omega\alpha_{vol}^2}{C_P}. \tag{2.25}$$

[1]For the proofs of Eqs. 2.24 and 2.25 see Ref. [55] (pag. 7).

An overall measure of the anharmonicity of the system is given by the macroscopic Grüneisen parameter which is the average of the mode-Grüneisen parameters weighted by the mode contributions to the heat capacity of Eq. 2.23:

$$\gamma = \frac{\sum_{\mathbf{q}\nu} c_{\mathbf{q}\nu}\gamma_{\mathbf{q}\nu}}{\sum_{\mathbf{q}\nu} c_{\mathbf{q}\nu}} = \frac{\Omega\alpha_{vol}B^T}{C_V} = \frac{\Omega\alpha_{vol}B^S}{C_P}. \tag{2.26}$$

2.3 The general case: strain-temperature variables

The previous formulation can be easily applied to isotropic cubic crystals whose lattice is defined by one parameter, the lattice constant a, or equivalently by the volume Ω of the unit cell. This approach is still valid for anisotropic solids but, in this case, for each Ω we have additional crystal parameters: from two, for the hexagonal, tetragonal and trigonal systems, up to six, for the triclinic system. One widely-used option is to optimize all crystal parameters at $T = 0$ K for each volume and use the previous formulation. On the other hand we can, more accurately, write the Helmholtz free-energy as a function of the crystal parameters and optimize all of them at each temperature T. For this purpose, the formulation above must be generalized by introducing the concepts of strain and stress as we do in this section. Moreover, this formalism allow us to introduce the definition of the elastic constants of crystals.

2.3.1 Strain and stress

The strain applied to a solid is described by a 3×3 strain matrix ϵ_{ij}. Let us consider a crystal described by the three primitive vectors $\mathbf{a}_1$, $\mathbf{a}_2$, $\mathbf{a}_3$. The strain ϵ_{ij} transforms them into the strained lattice vectors $\mathbf{a}'_1$, $\mathbf{a}'_2$, $\mathbf{a}'_3$ as:

$$\mathbf{a}'_{ji} = \mathbf{a}_{ji} + \sum_{k=1}^{3} \epsilon_{jk}\ \mathbf{a}_{ki}, \tag{2.27}$$

where $\mathbf{a}_{ki}$ is a matrix having the unperturbed primitive vectors as columns. In general we consider only symmetric strains such that $\epsilon_{ij} = \epsilon_{ji}$.

The stress σ_{ij} is the *i-th* component of the force per unit of area that acts on the surface A_j of an element of volume of the solid (Fig. 2.1).

In a solid under a constant stress σ_{ij}, to change the strain by $d\epsilon_{ij}$, the solid must do a work $dW = \Omega \sum_{ij} \sigma_{ij} d\epsilon_{ij}$ where Ω is the unperturbed cell volume. Using the definition of the stress with the signs shown in Fig. 2.1, in the expression of dW

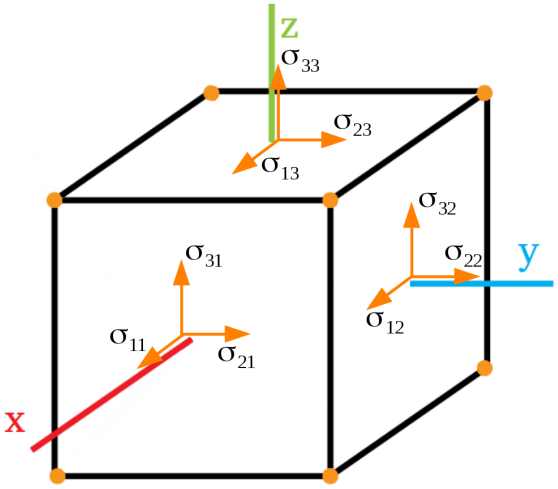

FIGURE 2.1: Volume element inside a stressed body. There are forces exerted on the surfaces of the element by the material surrounding it. These forces are proportional to area of the surface of the element, the force per unit area is the so-called "stress". We only consider homogeneous stresses where forces acting on the surface of an element of fixed shape and orientation do not depend on the position of the element in the body. The force exerted across each face of the cube can be divided into three components. For example the face perpendicular to the x axis is A_1 and the three relative components of the stress are σ_{11} (the normal component), σ_{21} and σ_{31}. Since the stress is homogeneous the forces applied to the opposite face is equal and opposite. The same statement holds for the other faces A_2 and A_3.

there is not the minus sign (differently from section 2.2) because by definition the component of the stress is $\sigma_{ii} = -P$. Then, the isotropic pressure is $P = -\frac{1}{3}\sum_i \sigma_{ii}$.

Following the same reasoning of Section 2.2 we write the variation of the internal energy of a solid at temperature T, under the stress σ_{ij} when the strain changes of $d\epsilon_{ij}$ and the solid adsorbs the heat TdS to keep T constant as: $dU = TdS + \Omega \sum_{ij} \sigma_{ij} d\epsilon_{ij}$, whence:

$$\sigma_{ij} = \frac{1}{\Omega}\left[\left(\frac{\partial U}{\partial \epsilon_{ij}}\right)_T - T\left(\frac{\partial S}{\partial \epsilon_{ij}}\right)_T\right] = \frac{1}{\Omega}\left(\frac{\partial F}{\partial \epsilon_{ij}}\right)_T . \tag{2.28}$$

The equilibrium configuration at temperature T is the one with $\sigma_{ij} = 0$ that is the one obtained by the free-energy minimization with respect to strain. In practice, the minimization is done with respect to strains that conserve the shape of the unit cell and the Bravais lattice. Therefore, this is equivalent to minimize the free-energy with respect to the crystal parameters.

2.3.2 Elastic constants at zero temperature

For sufficiently small strains the amount of stress is found to be proportional to the magnitude of the strain applied in a solid (Hooke's Law). Under this condition, the proportionality constants between stress and strain, for a given arrangement of their directions, define the elastic constants, or elastic stiffness, of the crystal:

$$C_{ijkl} = \left(\frac{\partial \sigma_{ij}}{\partial \epsilon_{kl}}\right)_0 , \tag{2.29}$$

where the subscript 0 means that the derivative are computed at zero strain: $\epsilon_{ij} = 0$. The C_{ijkl} form a fourth rank tensor with 81 entries but the actual number of

independent elastic constants is determined by the symmetry properties of the tensor and the crystal system under consideration. The symmetry of elastic constants are discussed in more details in the Appendix A and we will see later an example of application in cubic crystals.

Doing a strain on a solid that has energy E_0, we obtain a solid with energy $E(\{\epsilon_{ij}\})$ which can be Taylor expanded up to second order in the strain as:

$$E(\{\epsilon_{ij}\}) = E_0 + \sum_{ij} \left(\frac{\partial E}{\partial \epsilon_{ij}}\right)_0 \epsilon_{ij} + \frac{1}{2} \sum_{ijkl} \left(\frac{\partial^2 E}{\partial \epsilon_{ij} \partial \epsilon_{kl}}\right)_0 \epsilon_{ij}\epsilon_{kl}, \tag{2.30}$$

where the derivatives are computed at zero strain. The linear terms in the strain define the components of the initial stress:

$$\sigma^0_{ij} = \frac{1}{\Omega} \left(\frac{\partial E}{\partial \epsilon_{ij}}\right)_0, \tag{2.31}$$

the quadratic term defines the constants:

$$\tilde{C}_{ijkl} = \frac{1}{\Omega} \left(\frac{\partial^2 E}{\partial \epsilon_{ij} \partial \epsilon_{kl}}\right)_0, \tag{2.32}$$

that we have indicated with the *tilde* to differentiate them from the ECs of Eq. 2.29. As a matter of fact the relation between the two quantities is:

$$C_{ijkl} = \tilde{C}_{ijkl} - \frac{1}{2} \left(2\sigma^0_{ij}\delta_{kl} - \sigma^0_{ik}\delta_{jl} - \sigma^0_{il}\delta_{jk} - \sigma^0_{jl}\delta_{ik} - \sigma^0_{jk}\delta_{il}\right). \tag{2.33}$$

Hence, they are equal $C_{\alpha\beta\gamma\delta} = \tilde{C}_{\alpha\beta\gamma\delta}$ only if $\sigma^0_{ij} = 0$. If the initial stress is an isotropic pressure, i.e. $\sigma^0_{\alpha\beta} = -P\delta_{\alpha\beta}$, then:

$$C_{ijkl} = \tilde{C}_{ijkl} + \frac{1}{2} P \left(2\delta_{ij}\delta_{kl} - \delta_{il}\delta_{jk} - \delta_{ik}\delta_{jl}\right). \tag{2.34}$$

Eq. 2.33 and Eq. 2.34 tell us how to link the stress-strain ECs to the second derivatives of the energy for a generic stress or isotropic pressure. They are derived and discussed in more details in the Appendix A. Moreover, the atoms have to be allowed to relax in the positions that minimizes the total-energy for each strain.

2.3.3 Temperature dependent elastic constants

The theory of previous section applies at $T = 0$ K but it can be generalized to finite temperature expanding in Eq. 2.30 the Helmholtz free-energy F instead of the energy. In this manner we can study the effects of zero-point quantum motion and temperature. From the free-energy expansion, the second-order coefficients read as:

$$\tilde{C}^T_{\alpha\beta\gamma\delta} = \frac{1}{\Omega}\left(\frac{\partial^2 F}{\partial\epsilon_{\alpha\beta}\partial\epsilon_{\gamma\delta}}\right)_0, \tag{2.35}$$

where the superscript T means *isothermal* and are computed at zero strain. If the system is out of equilibrium, the Eq. 2.33 and Eq. 2.34 can be applied to get the stress-strain isothermal ECs at temperature T. The Helmholtz free-energy F has the same form of Eq. 2.16 but with the dependence upon volume Ω replaced by the strain ϵ dependence. Such dependence is inherited by the strain dependence of the phonon angular frequencies $\omega_\eta(\mathbf{q}, \epsilon)$ within the QHA.

The EC computed via Eq. 2.35 is a function of T and depends on the starting reference-configuration identified by the set of crystal parameters X_0, i.e. $C^T_{\alpha\beta\gamma\delta} = C^T_{\alpha\beta\gamma\delta}(X_0, T)$. In order to get ECs at the minimum of the free-energy at each temperature, the information of the temperature variation of crystal parameters $X(T)$ is used to obtain the $C^T_{\alpha\beta\gamma\delta}[X(T), T]$. In practice, this can be done by computing the second derivatives at zero strain 2.35 for a grid of crystal parameters X_i, correcting

with Eq. 2.34 the results at finite pressure, and interpolating the $C^T_{\alpha\beta\gamma\delta}[X_i, T]$ at the $X(T)$ and get the final TDECs $C^T_{\alpha\beta\gamma\delta}[X(T), T]$.

In the TDECs calculation as well, the atomic positions can be relaxed at $T = 0$ K for each strain: a method to estimate the effect of finite-temperature atomic relaxation will be introduced in Chapter 4.

2.3.3.1 Calculation for cubic solids

The symmetry of ECs reduces the 81 components into 21. For this reason the ECs are usually expressed in the so-called Voigt notation with only two indices and presented as 6×6 matrix (see Appendix A and Ref. [56]). The number of independent ECs is further reduced by the symmetry properties of the crystal structure. They depend on the so-called Laue class of the crystal obtained by adding inversion to the point group [56]. In cubic solids there are three independent ECs and the ECs matrix has the following form:

$$\begin{pmatrix} C_{11} & C_{12} & C_{12} & . & . & . \\ C_{12} & C_{11} & C_{12} & . & . & . \\ C_{12} & C_{12} & C_{11} & . & . & . \\ . & . & . & C_{44} & . & . \\ . & . & . & . & C_{44} & . \\ . & . & . & . & . & C_{44} \end{pmatrix}, \tag{2.36}$$

where a dot indicates a zero entry. If the system is under a pressure P the stress-strain ECs are given by Eq. 2.34 that, in this case, simplify into:

$$\begin{aligned} C_{11} &= \tilde{C}_{11}, \\ C_{12} &= \tilde{C}_{12} + P, \\ C_{44} &= \tilde{C}_{44} - \frac{1}{2}P. \end{aligned} \tag{2.37}$$

The second order contribution to the total energy of a strained crystal, in Voigt notation, is:

$$E = \frac{\Omega}{2} \sum_{ij} \epsilon_i \tilde{C}_{ij} \epsilon_j. \tag{2.38}$$

In order to derive the three independent ECs, the following strains can be used:

$$\begin{aligned} \epsilon_A &= \begin{pmatrix} \epsilon_1 & 0 & 0 \\ 0 & \epsilon_1 & 0 \\ 0 & 0 & \epsilon_1 \end{pmatrix}, \quad \epsilon_E = \begin{pmatrix} 0 & 0 & 0 \\ 0 & 0 & 0 \\ 0 & 0 & \epsilon_3 \end{pmatrix}, \\ \epsilon_F &= \begin{pmatrix} 0 & \epsilon_4 & \epsilon_4 \\ \epsilon_4 & 0 & \epsilon_4 \\ \epsilon_4 & \epsilon_4 & 0 \end{pmatrix}. \end{aligned} \tag{2.39}$$

The strain ϵ_A does not change the shape of the cubic cell, while ϵ_E transforms it into a tetragonal cell and ϵ_F into a rhombohedral cell. None of the strains is volume conserving.

Since the C_{ij} tensor (or equivalently the $\tilde{C}_{ij}$) has the form 2.36, applying Eq. 2.38 we obtain, for each type of strain, the following relations for the elastic energy:

$$\begin{aligned} E_A &= \frac{3\Omega}{2} \left(\tilde{C}_{11} + 2\tilde{C}_{12} \right) {\epsilon_1}^2, \\ E_E &= \frac{\Omega}{2} \tilde{C}_{11} {\epsilon_3}^2, \\ E_F &= \frac{3\Omega}{2} \tilde{C}_{44} {\epsilon_4}^2. \end{aligned} \tag{2.40}$$

Hence, the ECs can be computed by fitting the energy as a function of strain with a polynomial, and taking the analytic second derivatives. The same relation 2.38 is valid at finite temperature for the Helmholtz free-energy. So, at each temperature the ECs can be computed by fitting the free-energy with 2.40. The ECs are computed at different volumes Ω_i (or, equivalently, cubic lattice constants a_i) to get $\tilde{C}_{ij}(\Omega_i, T)$. They are converted with 2.34 into the stress-strain $C_{ij}(\Omega_i, T)$ and interpolated at the temperature dependent volume $\Omega(T)$. The details of this procedure and the workflow of the algorithm are discussed in more details in Chapter 3.

2.3.4 The thermal expansion tensor

The thermal expansion is defined as the strain $d\epsilon_{ij}$ induced by a unitary change of temperature dT at constant stress:

$$\alpha_{ij} = \left(\frac{\partial \epsilon_{ij}}{\partial T}\right)_{\sigma}. \tag{2.41}$$

It is a symmetric tensor. The previous definition can be written in terms of the crystal parameters of the solid considered. Let us introduce the versor $\mathbf{l} = (l_1, l_2, l_3)$ perpendicular to a set of lattice planes and write the thermal expansion in this direction $\alpha_{\mathbf{l}}$ as:

$$\alpha_{\mathbf{l}} = \sum_{ij} \alpha_{ij} l_i l_j. \tag{2.42}$$

Along the direction $\mathbf{l}$ the thermal expansion is

$$\alpha_{\mathbf{l}} = \frac{1}{d_{\mathbf{l}}} \left(\frac{d d_{\mathbf{l}}}{dT}\right)_{\sigma}, \tag{2.43}$$

where $d_{\mathbf{l}}$ is the interplanar distance for that set of lattice planes.

Cubic solids. We have only one crystal parameter. The thermal expansion tensor is $\alpha_{ij} = \alpha\delta_{ij}$. We consider the lattice planes perpendicular to $\mathbf{l} = (0, 0, 1)$ and the thermal expansion in this direction is $\alpha_{33} = \alpha$. The interplanar distance is $d_{\mathbf{l}} = a$ for the simple cubic structure and $d_{\mathbf{l}} = \frac{a}{2}$ for the body-centered and face-centered cubic structures. So, for all three cubic crystals the thermal expansion is:

$$\alpha = \frac{1}{a(T)}\frac{da(T)}{dT}. \tag{2.44}$$

Hexagonal solids. As an example of anisotropic solid we consider those belonging to the hexagonal system that have two crystal parameters a and c. The non-zero component of the thermal expansion are $\alpha_{11} = \alpha_{22}$ and α_{33}. We can consider the lattice planes perpendicular to $\mathbf{l} = (1, 0, 0)$ whose distance is $d_{\mathbf{l}} = \frac{a}{2}$. Hence, for this direction we have $\alpha_{\mathbf{l}} = \alpha_{11}$ and

$$\alpha_{11} = \alpha_{22} = \frac{1}{a(T)}\frac{da}{dT}. \tag{2.45}$$

Then we can consider the planes perpendicular to $\mathbf{l} = (0, 0, 1)$. The distance between these planes is c. Since $\alpha_{\mathbf{l}} = \alpha_{33}$ we have:

$$\alpha_{33} = \frac{1}{c(T)}\frac{dc}{dT}. \tag{2.46}$$

Instead of the parameter c, the parameter c/a is often used. Since $c(T) = a(T)\frac{c}{a}(T)$, then:

$$\frac{dc}{dT} = \frac{da}{dT}c/a\,(T) + a(T)\frac{d\ c/a}{dT}, \tag{2.47}$$

and:

$$\alpha_{33} = \frac{1}{a(T)}\frac{da}{dT} + \frac{1}{c/a\,(T)}\frac{dc/a}{dT}. \tag{2.48}$$

2.3.5 Thermal expansion tensor from mode-Grüneisen parameters: The role of elastic constants

From the thermal expansion tensor α_{ij} we can compute the volume thermal expansion α_{vol} as:

$$\alpha_{vol} = \frac{1}{\Omega}\left(\frac{d\Omega}{dT}\right)_P = \sum_{i=1}^{3}\left(\frac{\partial \epsilon_{ij}}{\partial T}\right)_\sigma = \sum_{i=1}^{3}\alpha_{ii}. \tag{2.49}$$

For a cubic crystal we have $\alpha_{vol} = 3\alpha$. So, by using Eq. 2.22, the thermal expansion coefficient for a cubic crystal, written in terms of the mode-Grüneisen parameters becomes:

$$\alpha = \frac{1}{3B^T}\sum_{\mathbf{q}\nu} c_{\mathbf{q}\nu}\gamma_{\mathbf{q}\nu}. \tag{2.50}$$

Starting from the thermal expansion defined in Eq. 2.41 we now derive an equivalent expression of Eq. 2.50 valid for a generic, possibly anisotropic, solid:

$$\begin{aligned}\alpha_{ij} = \left(\frac{d\epsilon_{ij}}{dT}\right)_\sigma &= -\sum_{kl}\left(\frac{d\epsilon_{ij}}{d\sigma_{kl}}\right)_T\left(\frac{d\sigma_{kl}}{dT}\right)_\epsilon = \\ &= -\frac{1}{\Omega}\sum_{kl} S^T_{ijkl}\left(\frac{\partial^2 F(\epsilon,T)}{\partial T\partial\epsilon_{kl}}\right)_T,\end{aligned} \tag{2.51}$$

where $S^T_{ijkl} = \left(\frac{d\epsilon_{ij}}{d\sigma_{kl}}\right)_T$ defines the elastic compliances, the inverse of the stress-strain elastic constants tensor[2]. So, the final expression for the anisotropic thermal expansion tensor coefficients is:

$$\alpha_{ij} = \sum_{kl} S^T_{ijkl} \sum_{\mathbf{q}\nu} c_{\mathbf{q}\nu} \gamma^{kl}_{\mathbf{q}\nu}, \tag{2.52}$$

where $c_{\mathbf{q}\nu}$ is the generalization of the mode-heat capacity of Eq. 2.23 where the frequencies are now allowed to depend on strain:

$$c_{\mathbf{q}\nu} = \frac{\hbar\omega_{\mathbf{q}\nu}(\epsilon)}{\Omega} \frac{d}{dT}\left(\frac{1}{e^{\beta\hbar\omega_{\mathbf{q}\nu}} - 1}\right). \tag{2.53}$$

While $\gamma^{kl}_{\mathbf{q}\nu}$ is the generalization of the mode-Grüneisen parameter of Eq. 2.17 defined as:

$$\gamma^{kl}_{\mathbf{q}\nu} = -\frac{1}{\omega_{\mathbf{q},\nu}} \frac{d\omega_{\mathbf{q},\nu}}{d\epsilon_{ij}}. \tag{2.54}$$

Eq. 2.52 describes for each temperature the thermal expansion curve. We point out that in many practical calculations the temperature-dependent elastic compliances S^T_{ijkl} are replaced by their constant zero-temperature value for all temperatures: we will address the effect of this approximation in Chapter 3.

The sum of the elastic compliances is related to the bulk modulus:

$$\frac{1}{B^T} = \sum_{ij} S^T_{iijj}, \tag{2.55}$$

[2]For cubic solids there is a simple relation between the entries of the elastic constants and elastic compliances tensors: $S_{11} + 2S_{12} = (C_{11} + 2C_{12})^{-1}$, $S_{11} - S_{12} = (C_{11} - C_{12})^{-1}$ and $S_{44} = C_{44}^{-1}$.

and an equivalent relation holds for the adiabatic case. For example, the isothermal bulk modulus for the thermal expansion in cubic solids of Eq. 2.50 can be written in terms of the ECs as:

$$B^T = \frac{1}{3}\left(C_{11}^T + 2C_{12}^T\right). \tag{2.56}$$

2.3.6 Comparison with experiments: The adiabatic elastic constants

The isothermal ECs (Eq. 2.35 and Eq. 2.34), the thermal expansion coefficient (Eq. 2.41) and the isochoric heat capacity (Eq. 2.13 or Eq. 2.14), give access to the calculation of adiabatic ECs, usually provided by experiments:

$$C_{ijkl}^S = C_{ijkl}^T + \frac{T\Omega b_{ij} b_{kl}}{C_V}, \tag{2.57}$$

where b_{ij} is the thermal stress, obtained from:

$$b_{ij} = -\sum_{kl} C_{ijkl}^T \alpha_{kl}. \tag{2.58}$$

2.4 The electronic contribution to the free-energy

So far we have neglected the electronic contribution F_{el} to the free-energy in Eq. 2.16. This contribution could be important for the thermodynamic properties of metals. It can be accounted for by the Mermin's approach discussed in section 1.1.3 of the previous chapter. Alternatively we compute F_{el} from fixed band structures, neglecting their change due to temperature. We use:

$$F_{el} = U_{el} - TS_{el}, \tag{2.59}$$

where U_{el} is the electronic excitation internal energy:

$$U^{el} = \int_{-\infty}^{+\infty} EN(E)fdE - \int_{-\infty}^{E_F} EN(E)dE, \tag{2.60}$$

and S_{el} is the electronic entropy:

$$S^{el} = -k_B \int_{-\infty}^{+\infty} \left[f \ln f + (1-f)\ln(1-f)\right] N(E)dE. \tag{2.61}$$

In Eqs. 2.60 and 2.61 $f(E, \mu, T)$ indicates the Fermi-Dirac occupations (depending on E, the temperature T, and the chemical potential μ), $N(E)$ is the electronic density of states and E_F is the Fermi energy. The chemical potential μ is calculated at each temperature to give the number of electrons per unit cell in the formula $N_{el} = \int_{-\infty}^{\infty} N(E)f(E, T, \mu)dE$.

Chapter 3

Temperature-dependent elastic constants

In the previous chapter we have introduced the basic physical relationships required to describe the thermodynamic and thermoelastic properties of a crystal. In this chapter we apply them to several elemental solids (Si, Al, Ag, Pd, Pt, Cu, Au) and to BAs. In particular we will focus on the TDECs, quantities that requires almost all the thermodynamic properties that we have introduced. The systems considered are paradigmatic examples of cubic semiconductors, transition and noble metals, and are chosen also on the basis of availability of experimental data for the TDECs or for the technological interest.

We start in Section 3.1 by describing the methods for the calculation of the TDECs: the quasi-static approximation (QSA), where only the effect of the thermal expansion on the EC is considered, and the QHA, more accurate, which accounts for the contribution of the vibrational free-energy in the strained configurations. The

general algorithm and the workflows that we discuss have been implemented in the `thermo_pw` code.

In Section 3.2 we investigate the TDECs of Si, Al and Ag and we use these systems as samples to perform various tests of the methodology. For them we compare the QSA and the QHA finding that, increasing temperature, the QHA gives almost the same percentage change of ECs as the experiment while the QSA gives a somewhat smaller softening. In these systems we compute the thermal expansion (TE) coefficient with the Grüneisen formulation (Eq. 2.50 and Eq. 2.56). We find that the QHA ECs allow to reproduce with remarkable accuracy the TE given by the differentiation of the temperature dependent lattice constants while the TE computed with the zero temperature ECs, a method widely used in literature, is more approximated, quite distant at large temperatures from experiments for the metals. This part of the thesis has been published in Ref. [1].

In Section 3.3 the TDECs of Pd, Pt, Cu, Au are investigated. The first two elements, Pd and Pt, present anomalies in the experimental TDECs that are not well understood, while the latter two are more regular. Already after the early measurements on Pd and Pt some models were put forward to explain the anomalous temperature dependence of their elastic constants [57–60] and recently a computational DFT study, based on the QSA, has supported this interpretation [61]. They pointed out that the TDECs of Pd and Pt are anomalous due to the partially filled d bands whose electrons contribute substantially to the free-energy. On the other hand, another theoretical study within the QSA finds a conventional temperature dependence for all the ECs of Pd, even considering the electronic thermal excitations [62]. Hence, in this section we extend the QHA implementation to include the effects of the electronic excitation on the TDECs (as well as the other thermodynamic quantities) and use it to account it for these metals. We find that

the electronic contribution, although smaller than the vibrational one, is relevant for the temperature dependence of the C_{44} ECs of Pd and Pt, where it improves the comparison with experiment, but it is not sufficient to reproduce in detail the anomalies. On the contrary, in Cu and Au, whose d shells are completely filled, the electronic contribution to the TDECs is negligible. Focusing on Pt we investigate also another possible source of anomalous behavior. Electronic excitations might change the phonon frequencies at high temperatures, so we calculate the effect of this change on the TDECs. We find no substantial contribution, not even at the highest studied temperature of $T = 1000$ K. Moreover, for these materials we also address the effect of the exchange and correlation functionals, not yet discussed in detail for the TDECs. We present a systematic comparison between LDA and GGA. We find that all functionals give similar softenings for increasing temperature, hence the functional that matches better the experimental ECs at $T = 0$ K turns out to be also the one that matches better the TDECs. This section of the thesis has been published in Ref. [2].

Finally, in Section 3.4 we investigate the thermodynamic and thermoelastic properties of a material of technological interest: BAs, a semiconductor that exhibits ultra-high thermal conductivity and is under investigation for thermal management in electronics. Although the growth of BAs was reported since 1950s, only recently high-quality samples have been synthesized with the measurement of an ultrahigh thermal conductivity up to 1300 W m^{-1} K^{-1} [63–66]. These measurements spurred the interest for this material so that many experiments and theoretical calculations have been carried out to investigate its physical properties. In the electronic devices boron arsenide could be an optimal heat sink. The knowledge of thermodynamic properties of the heatsink are crucial because they have to match those of the active electronic elements (usually made of Si) in order to avoid thermal stresses. We test

the consistency of our TDECs by computing the temperature dependent sound velocity of the longitudinal acoustic mode along the [111] direction and compare with experiment. Furthermore we present the room temperature phonon dispersions, the temperature dependent thermal expansion, isobaric heat capacity, and average Grüneisen parameter comparing with the most updated experiments and previous calculations when available. This work has been presented in the paper of Ref. [3].

3.1 Practical implementation

The TDECs calculation can be done with three different levels of approximations, namely (i) the QSA, the QHA at fixed geometry and (iii) the QHA at variable geometry (i.e. at the minimum of the free-energy).

In this chapter the internal coordinates are relaxed at $T = 0$ K. This approximation, used so far in the TDECs calculations available in the literature, affects only the C_{44} elastic constants of Si and BAs, because all the other systems considered are monoatomic. We discuss in the next chapter the importance of this approximation for Si and BAs.

3.1.1 Quasi-static approximation

The QSA is the simplest and more approximated method. It ignores the fine details of the dependence of the stresses with temperature, i.e. it neglects the contribution to the vibrational free-energy in the strained configurations, and takes into account only the volume-temperature dependence $\Omega(T)$. ECs are computed at different volumes at $T = 0$ K from the stress-strain derivatives (Eq. 2.29) or from the energy

derivatives (Eqs. 2.32 and 2.34)[1]. The energy-approach for cubic solids is detailed in Section 2.3.3.1 and requires the calculation of the total energy of the strained configurations, usually 6 strain magnitudes for each type of strain. This calculation is usually performed on 7 or 9 volumes. Then, once we get the ECs at different volumes, they are interpolated at the temperature dependent geometry $\Omega(T)$ (or $X(T)$ where X is the set of crystal parameters).

3.1.2 Quasi-harmonic approximation at fixed geometry

The QSA can be generalized taking into account the contribution of the vibrational free-energy (Eq. 2.6 or Eq. 2.11) for which we need the calculation of phonon dispersions in the strained geometries. For instance, in Fig. 3.1 we show the phonon dispersions for the three types of strains required for Si. The vibrational free-energy is added to the total-energy to build the Helmholtz free-energy. Then, the ECs at finite temperature are computed from the second derivatives of the free-energy with respect to strain 2.35: for cubic solids, this means to take the analytical derivative of the Helmholtz free-energies in the form of Eqs. 2.40. If a pressure is acting on the system, the Eq. 2.34 is applied to get the stress-strain ECs. This method provides the temperature-dependent ECs $C_{ij}(T, \Omega_0)$ where Ω_0 is the volume of the fixed reference geometry (or $C_{ij}(T, X_0)$ where X_0 is the set of crystal parameters of the reference geometry).

[1] If the stress of Eq. 2.29 is computed with the stress theorem [67], the two methods are independent and, the calculation of ECs with both of them provides a way to check the convergence of the computational parameters. This should be done for, at least, one geometry.

3.1.3 Quasi-harmonic approximation at variable geometry

The equilibrium configuration of a crystal changes with temperature, in the most common case the volume expands as the temperature increases. Since the derivatives

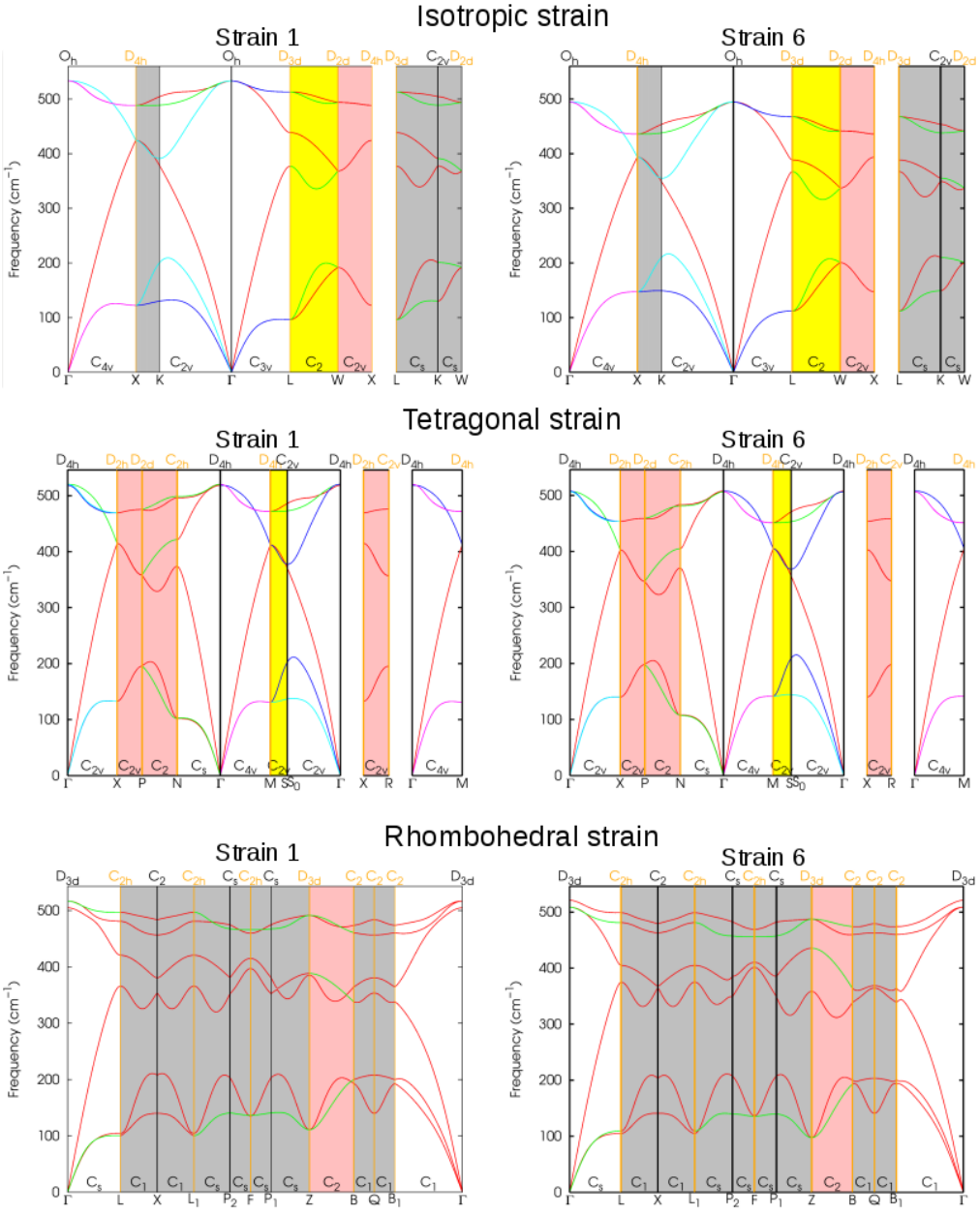

FIGURE 3.1: Phonon dispersions of Si for a TDECs calculation at fixed geometry within the QHA. In this example, the phonons of the first and last (6^{th}) strained configurations are shown for each type of strain (Eq. 2.39).

of Eq. 2.35 are evaluated at equilibrium (in the zero-strain reference configuration) we should, in principle, compute them at the corresponding thermal expanded reference configuration at each temperature, i.e. at the minimum of the free-energy. This would require an EC calculation at each temperature with the correct reference configuration and an unaffordable computational cost for calculations for continuous range of temperatures. In order to overcome this problem we perform the QHA calculation at fixed geometry for a set of volumes $\{\Omega_i\}$ (or crystal parameters $\{X_i\}$) of some reference geometries, getting $C_{ij}(T, \Omega_i)$. This ECs are fitted with polynomials depending on the crystal parameters and interpolatad at the temperature dependent geometry, i.e. $\Omega(T)$ or $a(T)$ in the case of cubic solids. In this way we get the TDECs at the minimum of the free-energy at each temperature, namely the ECs $C_{ij}\left[T, \Omega(T)\right]$. The scheme to perform this calculation, is presented in the next section.

3.1.4 The workflow

The calculation of the TDECs within the QHA with the `thermo_pw` code is divided in two parts as illustrated in Fig. 3.2. The first part (left) corresponds to the calculation of the TDECs (QHA at fixed geometry) for a grid of reference geometries centered on the input geometry. For each reference geometry all the strained geometries required for an elastic constant calculation are generated and phonons are computed for each strained configuration. All these calculations can be ran sequentially or in parallel. Having the phonon frequencies of each strained geometry it is possible to compute, within the harmonic approximation, the thermodynamic quantities that depend from them (in particular the vibrational free-energy of Eq. 2.6 and Eq. 2.11). Then the second derivatives of the free-energy with respect to strain are computed at each temperature and the results are corrected for finite pressure effects in order

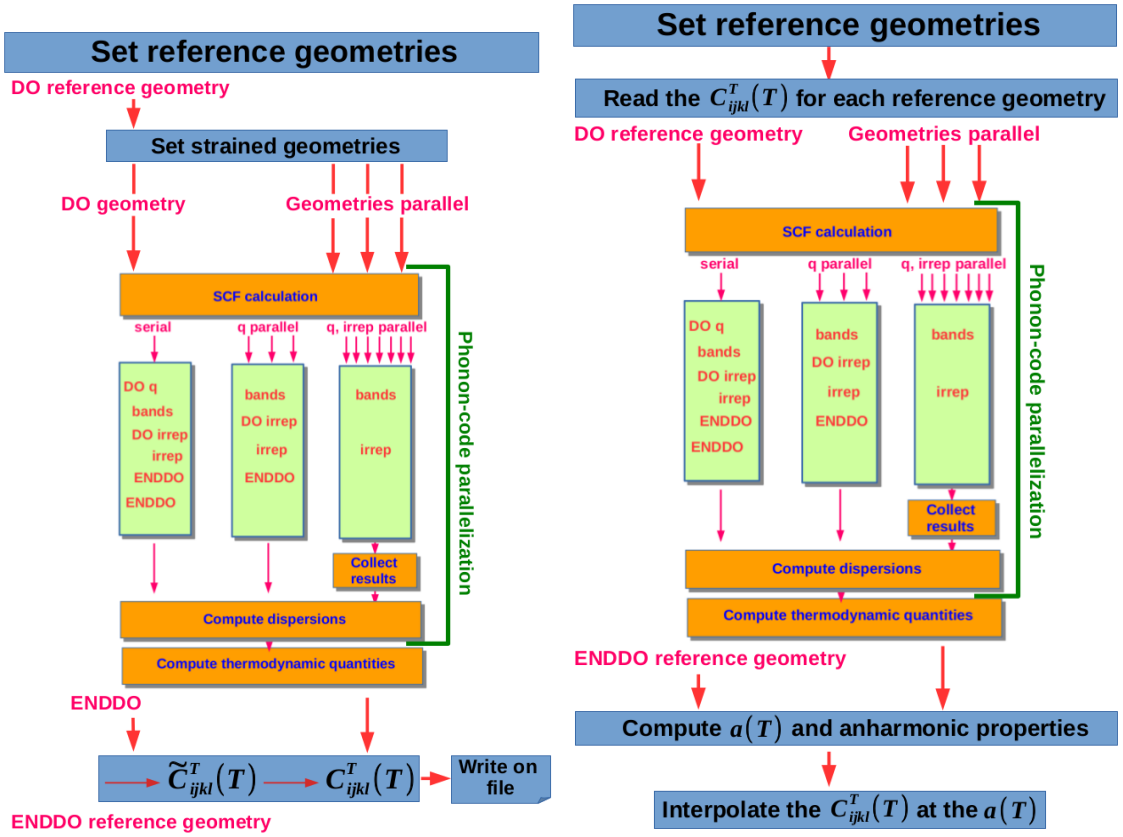

FIGURE 3.2: Flow-chart of the calculation of the TDECs within the QHA with the `thermo_pw` code. Left: calculation of the TDECs at the selected reference unperturbed geometries. Right: calculation of anharmonic properties and interpolation of the TDECs at the minimum of the free-energy.

to get the stress-strain ECs (Eq. 2.34). A file with the TDECs is written for each reference geometry.

The second part (right) is devoted to the computation of the anharmonic properties within the QHA. It needs the files of the TDECs at each reference geometry produced by the first part (left). The choice of the references geometries is the same as in the first part. The phonons and vibrational free-energy are computed at each reference geometry. For each reference geometry, at temperature T, the vibrational free-energy is added to the energy to get the Helmholtz free-energy. The free-energies at the various geometries are interpolated and minimized to get the $a(T)$, or the set of crystal parameters $X(T)$, and the thermal expansion. The TDECs at the various

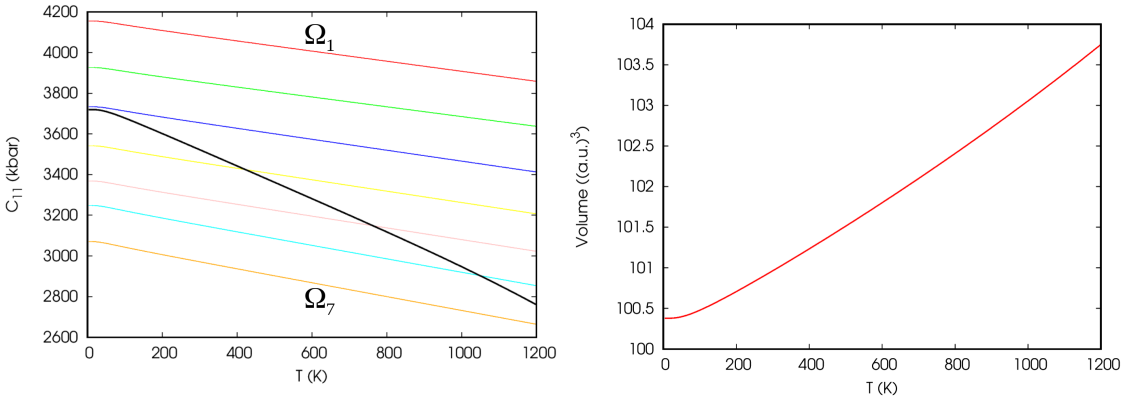

FIGURE 3.3: Interpolation of TDECs with the `thermo_pw` code. Left. Elastic constant $C_{11}(T, \Omega_i)$ of Pt for seven references geometries with volume Ω_i (colored thin lines) and interpolated elastic constants $C_{11}[T, \Omega(T)]$ (black line). Right. Temperature dependent unit-cell volume of Pt $\Omega(T)$ used to interpolate the $C_{11}(T, \Omega_i)$. In this example the electronic contribution to the free-energy is neglected.

geometries are interpolated and, at each temperature T, the value corresponding to the $a(T)$ or $X(T)$ is evaluated from the interpolation. All the interpolations are done by polynomials whose degrees can be set in input. In this way we obtain the final isothermal TDECs (computed at the minimum of the free-energy) and, by applying Eqs. 2.57 and 2.58, we compute the adiabatic TDECs. In this second part the parallelization is done as in the first part as shown in Fig. 3.2 although the number of required phonon dispersions is much smaller so that this part of the calculation takes only a small fraction of the total computational time.

In order to compute the TDECs within the QSA, the ECs are evaluated at $T = 0$ K at the different reference geometries and then they are saved on a different file for each geometry. The second part of Fig. 3.2 does not change provided that the files of the $T = 0$ K ECs are read instead of the TDECs.

3.1.4.1 Interpolation methods

In Fig. 3.3 an example of interpolation is reported. On the left the $C_{11}(T, \Omega_i)$ of Pt are in colored lines for seven reference geometries. They are fitted with a polynomial and interpolated at the temperature dependent volume (right). The final result $C_{11}[T, \Omega(T)]$ is the black line on the left.

In other works (see for instance Ref. [43]) the QHA ECs are evaluated with a slightly different procedure. First for each type of strain the Helmholtz free energy is fitted by a polynomial in a grid of the lattice constants and strain magnitudes and then the ECs are calculated as second derivatives of the Helmholtz free-energy with respect to the strain at the temperature dependent lattice constant. We have verified that the results obtained by this more conventional method are very similar to those obtained by our procedure and both approaches are available in `thermo_pw`. For this second approach, it is sufficient to run the first workflow of Fig. 3.2 by providing the file with the temperature dependent crystal parameters. The program will interpolate the isothermal ECs. This approach can be used to check the results given by the other metod.

3.2 Silicon, aluminum and silver

We validate our implementation by studying the TDECs of three elemental crystals: Si with the diamond structure and the face-centered cubic metals Al and Ag. The starting point is the calculation of the $T = 0$ K ECs that we will address in the following sections for these materials. Further tests of the $T = 0$ K ECs, also for different crystal systems, are discussed in the Appendix B.

3.2.1 Computational parameters

We perform all our calculations within DFT. The exchange and correlation functional is approximated by the LDA for Si [48] and the GGA of Perdew-Burke-Ernzerhoff modified for densely packed solids (PBEsol) [50] for Al and Ag. We took the exchange and correlation functionals that, on the basis of previous theoretical calculations, give a better agreement with the experiment for the TE and/or phonon dispersion curves. For Si we used the pseudopotential `Si.pz-nl-kjpaw_psl.1.0.0.UPF`, the cutoff for the wave functions was 60 Ry, the one for the charge density 640 Ry, and the **k**-points mesh was $16 \times 16 \times 16$. For Al we used the pseudopotential `Al.pbesol-n-kjpaw_psl.1.0.0.UPF`, the cutoff for the wave functions was 30 Ry, the one for the charge density 120 Ry, and the **k**-points mesh was $48 \times 48 \times 48$. For Ag we used the pseudopotential `Ag.pbesol-n-kjpaw_psl.1.0.0.UPF`, the cutoff for the wave functions was 70 Ry, the one for the charge density 300 Ry, and the **k**-points mesh was $64 \times 64 \times 64$. In the case of Al and Ag, the presence of the Fermi surface has been dealt with by the Methfessel-Paxton smearing approach [51] with a broadening $\sigma = 0.02$ Ry. The DFPT was used to calculate the dynamical matrices on a $8 \times 8 \times 8$ **q**-points grid for Si (corresponding to 29 special **q**-points for configurations strained with ϵ_A, 59 **q**-points for ϵ_E and 65 for ϵ_F) while for the metals we employed a $4 \times 4 \times 4$ **q**-points grid (corresponding to 8 **q**-points for configurations strained with ϵ_A and 13 **q**-points for those strained with ϵ_E and ϵ_F). These dynamical matrices have been Fourier interpolated on a $200 \times 200 \times 200$ **q**-points mesh to evaluate the free-energy. For the calculation of TDECs, we used 9 reference geometries for Si with lattice constants separated by $\Delta a = 0.05$ a.u., 7 for Al separated by $\Delta a = 0.07$ a.u., and 7 for Ag separated by $\Delta a = 0.085$ a.u.. The same grid is used for the calculation of the $a(T)$ and the TE. For all three materials we used 6 strained configurations for each type of strain with a strain interval $\delta\epsilon = 0.005$. In

total we computed the phonon dispersions for 162 geometries for Si and 126 geometries for Al and Ag in addition to those computed on the reference configurations required to compute the $a(T)$ and the TE. In order to fit the energy (for the QSA) or the free-energy (for the QHA) as a function of strain we used a polynomial of degree two. To fit the ECs computed at the various reference configurations at the temperature dependent geometry we used a polynomial of degree four.

3.2.2 Results

In Table 3.1 we report the theoretical lattice constants: the equilibrium values at $T = 0$ K with and without zero point energy and the values at $T = 300$ K. The latter is in good agreement with the room temperature experimental value [68]: for all three elements, the experimental values being slightly larger (with differences of 0.03 Å in Si, 0.01 Å in Al, and even less in Ag). In Table 3.2 we compare our ECs computed at $T = 0$ K with those obtained considering the zero point energy given by the QHA. We also report the comparison with experiment and other theoretical works.

TABLE 3.1: Theoretical lattice parameters (in Å) at different temperatures compared with experiment [68] at room temperature. ZPE indicates the zero point energy.

	T=0 K	T=0 K+ZPE	T=300 K	Expt.
Silicon (LDA)	5.40	5.41	5.41	5.4307
Aluminum (PBEsol)	4.01	4.03	4.04	4.04958
Silver (PBEsol)	4.06	4.07	4.08	4.0862

3.2.2.1 Silicon

In Figure 3.4 the LDA TDECs of Si computed by means of the QSA (blue curves) and the QHA (red curves) are shown. The dashed lines indicate isothermal ECs, the continuous lines the adiabatic ECs obtained by Eq. 2.57. The experimental points (black line) are adiabatic ECs obtained from ultrasonic experiments [73]. At

TABLE 3.2: ECs at $T = 0$ K compared with the results available in the literature. The exchange and correlation functionals are indicated in the first column. In addition to PBEsol used by us, the GGA functionals PBE [49] and PW [69] were used in the references. The equilibrium lattice constants (a_0) is in Å while the ECs are in kbar.

	a_0	C_{11}	C_{12}	C_{44}
Silicon				
LDA[a]	5.40	1618	640	761
LDA[b]	5.41	1580	639	746
LDA[c]	5.40	1590	610	850
LDA[d]	5.38	1621	635	773
LDA[e]	5.40	1610	650	760
PBE[e]	5.47	1530	570	740
PBEsol[e]	5.44	1560	620	740
Expt.[l]	5.43	1675	650	801
Aluminum				
PBEsol[a]	4.01	1192	643	365
PBEsol[b]	4.03	1146	632	353
LDA[g]	3.97	1222	608	374
LDA[h]	4.04	1104	545	313
PBE[f]	4.06	1093	575	301
PW[i]	4.05	1010	610	254
Expt.[m]	4.05	1143	619	316
Silver				
PBESOL[a]	4.06	1450	1067	540
PBESOL[b]	4.07	1425	1054	531
GGA[h]	4.02	1612	1191	581
PW[i]	4.16	1159	851	421
Expt.[n]	4.09	1315	973	511

[a] This work at $T = 0$ K, [b] This work at $T = 0$ K + ZPE, [c] Reference [70], [d] Reference [8], [e] Reference [71]
[f] Reference [11], [g] Reference [72], [h] Reference [9], [i] Reference [39],
[l] a_0 from Table 1 at $T = 300$ K. ECs at $T = 77$ K [73]
[m] a_0 from Table 1 at $T = 300$ K. ECs extrapolated at $T = 0$ K [74]
[n] a_0 from Table 1 at $T = 300$ K. ECs extrapolated at $T = 0$ K [75]

the temperature corresponding to the experimental points the difference between isothermal and adiabatic ECs C_{11} and C_{12} is quite small and it remains small also at higher temperatures. Between adiabatic and isothermal C_{44} of cubic solids with a diagonal TE tensor there is no difference.

In general the theoretical values are slightly below the experimental data (see also Table 3.2): in particular these differences are about 6 % for C_{11}, 2 % for C_{12}, and 7 % for C_{44} at the lowest experimental temperature $T = 77$ K. Our $T = 0$ K EC agrees with almost all LDA ECs reported in Table 3.2 with typical differences of about 2 %. Only Ref. [70] has larger discrepancies. The PBE and PBEsol values are lower than LDA and hence more distant from experiment. The experimental ECs decreases by $\approx 1.1\%$ for C_{11}, $\approx 1.8\%$ for C_{12}, and $\approx 0.7\%$ for C_{44} from 77 K to 300 K. The

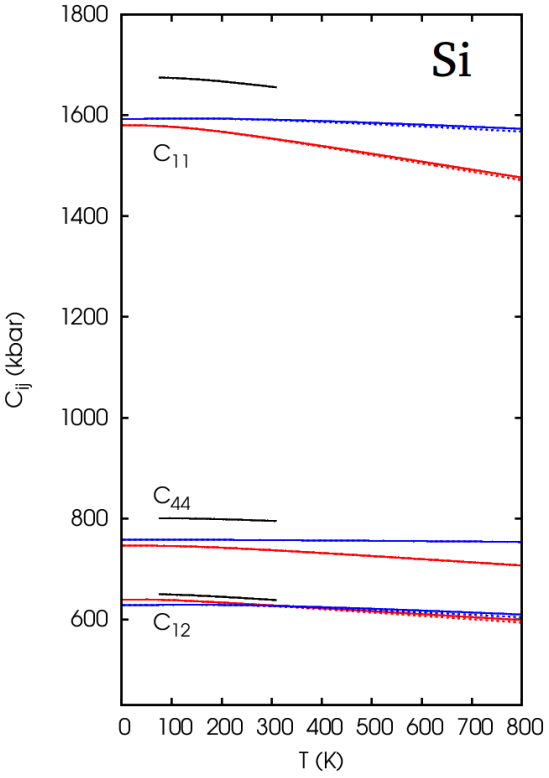

FIGURE 3.4: LDA temperature dependent elastic constants of Si. QHA (red curves) is compared with QSA (blue curves). The isothermal (dashed lines) and adiabatic (continuous lines) elastic constants are reported. Experimental data are taken from McSkimin [73] (black lines).

theoretical softening in the same temperature range are $\approx 1.6\%$ (QHA) and $\approx 0.1\%$ (QSA) for C_{11}, $\approx 1.9\%$ (QHA) and $\approx 0.3\%$ (QSA) for C_{12}, $\approx 1.2\%$ (QHA) and $\approx 0.1\%$ (QSA) for C_{44}. The theoretical QHA reproduces better the experimental trend than the QSA. Although in the experimental temperature range the decrease of the ECs is small, in the whole temperature range 0 K - 800 K considered in the plot, the QHA ECs have a not negligible variation: C_{11} and C_{12} decrease of about 7 % and C_{44} of 5 %. In Figure 3.5 we show the bulk modulus obtained from these TDECs. The comparison between theoretical and experimental adiabatic bulk moduli obtained from the experimental ECs using Eq. 2.56 (left) reflects the behavior of the ECs: the temperature dependence is more in agreement with QHA (red curve) than QSA (blue curve). Moreover, the QHA is much more in agreement with the bulk modulus obtained from the Murnaghan equation (orange curve) and differs from the experiment (black line) by an almost constant amount. Finally we present

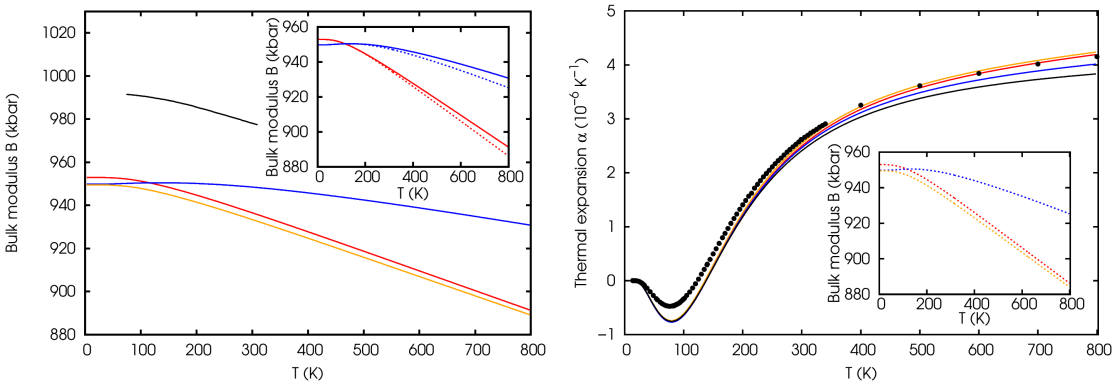

FIGURE 3.5: Left. Temperature dependent adiabatic bulk modulus of Si. QHA (red curves), QSA (blue curves) and experimental points [73]. The orange curve is the bulk modulus obtained from the Murnaghan equation. In the inset a comparison between the adiabatic (continuous lines) and the isothermal (dashed lines) bulk moduli. Right. Thermal expansion of Si: computed as in Eq. 2.44 (orange curve). The other curves are computed by using Eq. 2.50 with a bulk modulus derived from ECs (Eq. 2.56): TDECs computed via QHA (red curve) or QSA (blue curve) and $T = 0$ K ECs (black curve). The experimental points are taken from [76] and [77]. In the inset the isothermal bulk moduli are reported: QHA (red dashed line), QSA (blue dashed line) and obtained from Murnaghan equation (orange dashed line).

the TE calculated by the Grüneisen's formula (Eq. 2.50). In order to gauge our TDECs we take as reference the TE coefficient computed via Eq. 2.44. This curve is reported in the right side of Figure 3.5 (orange). The difference of the TEs with the reference is quantified by computing the area percentage error (APE) that is the percentage difference of the areas under the TE curves. The TE obtained with the isothermal bulk modulus derived from the Murnaghan equation (orange dashed line in the inset) differs by less than 0.04%. The TE derived from QHA almost overlaps with the previous one (it is slightly lower) since the two corresponding bulk moduli (orange and red dashed lines in the inset) are very close to each other: in this case the APE is about 1.7%. The isothermal QSA bulk modulus (blue dashed line in the inset) is larger so the corresponding TE is smaller at higher temperatures with an APE $\approx$ 4.4%. The black line is the TE computed with fixed ECs (T = 0 K without zero point contributions). It gives the smallest TE with an APE of about 7.5%. In general, in Si the different methods give very similar results, especially at temperature lower than $\approx$ 200 K for which an almost perfect overlap is found. Finally, the theoretical TEs are in good agreement with experimental points [76, 77] as already found in previous literature [78].

3.2.2.2 Aluminum

In Figure 3.6 we report the PBEsol TDECs of Al with the same meaning for the lines and colors as for Si. In Al there are several ultrasonic experiments which do not totally agree with each other. We report these experimental points in the same figure. Sutton data [79] are in the temperature range 63 K - 773 K (open triangles), Kamm and Alers [74] data are in the range 4.2 K - 300 K (full triangles), Gerlich and Fisher [80] data are in the range 293 K - 925 K (full circles), and Tallon and Wolfenden [81] data are in the range 273 K - 913 K (full circles). All

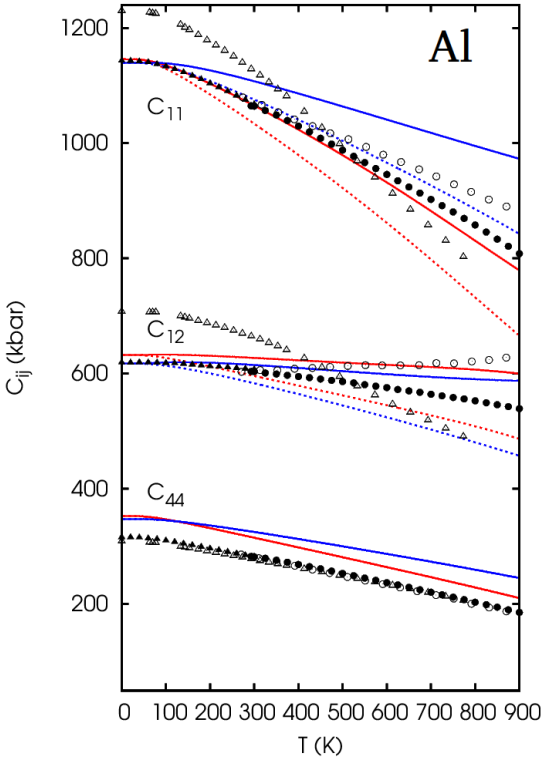

FIGURE 3.6: PBEsol temperature dependent ECs of Al. QHA (red curves) is compared with QSA (blue curves). The isothermal (dashed lines) and adiabatic (continuous lines) ECs are reported. Experimental data are taken from: Sutton [79] (open triangles), Kamm and Alers [74] (full triangles), Gerlich and Fisher [80] (full circles), Tallon and Wolfenden [81] (open circles).

experimental ECs are adiabatic and must be compared with the continuous lines. The temperature dependence and also the actual values measured by Sutton are quite distant from the other measurements for C_{11} and C_{12} (while the agreement improves for C_{44}). For this reason we do not further discuss these data in the rest of the paper. The QHA is in satisfactory agreement with both the data of Kamm and Alers, and Gerlich and Fisher. The data of Tallon and Wolfenden indicate less softening in C_{11} than Gerlich and Fisher and report a C_{12} which is approximately constant within the experimental errors, very similar to the theory in this case. Moreover, recent measurements of resonant ultrasound spectroscopy [82] of Young's modulus and shear modulus found good agreement with those derived from Gerlich and Fisher. On the other hand, the QSA shows a smaller softening in C_{11} and C_{44}

than the QHA, while smaller differences between the two approximations are present for C_{12}. The percentage differences between theoretical ECs (red continuous curves) and experimental points at $T = 0$ K (Kamm data) are -0.2 % (QHA) and 0.3 % (QSA) for C_{11}, -2 % (QHA) and 0.3 % (QSA) for C_{12}, -11 % (QHA) and -10 % (QSA) for C_{44}. The $T = 0$ K ECs are also reported in Table 3.2 and compared with previous literature. In the temperature range 0 K - 800 K the experiment of Kamm and Alers, and Gerlich and Fisher taken together show a softening of $\approx 25\%$ for C_{11}, $\approx 11\%$ for C_{12} and $\approx 36\%$ for C_{44}, while taking together the experiments of Kamm and Alers, and Tallon and Wolfenden in the same range of temperatures the percentage variations are: $\approx 20\%$ for C_{11}, $\approx -0.3\%$ for C_{12} and 36 % for C_{44}. The theoretical softening in the same temperature range are $\approx 28\%$ (QHA) and $\approx 13\%$ (QSA) for C_{11}, $\approx 4\%$ (QHA and QSA) for C_{12}, $\approx 35\%$ (QHA) and $\approx 25\%$ (QSA) for C_{44}. As for Si, in Sl the QHA reproduces better the experimental trend than QSA. Similar results have been obtained in Reference [82] with the PW functional.

We report in Figure 3.7 (left) the bulk modulus of Al computed with the different sets of ECs with the same meaning for the lines and colors as for Si. The adiabatic bulk modulus derived from the Murnaghan equation is also reported (orange curve): it is in good agreement with the bulk modulus computed from QHA TDECs (red curve) while larger differences are present with the QSA (blue curve) which remains higher at larger temperatures. In order to check the consistency of our ECs we calculate the TE by using Grüneisen's formula using the isothermal bulk modulus obtained from the TDECs (the comparison between adiabatic and isothermal bulk moduli is shown in the inset). We take as reference the TE coefficient computed from finite differences and compute the APE as done for Si. The TE obtained from mode-Grüneisen parameters (Eq. 2.50) with the bulk modulus derived from the Murnaghan equation (orange dashed line in the inset) gives an APE $\approx 0.01\%$.

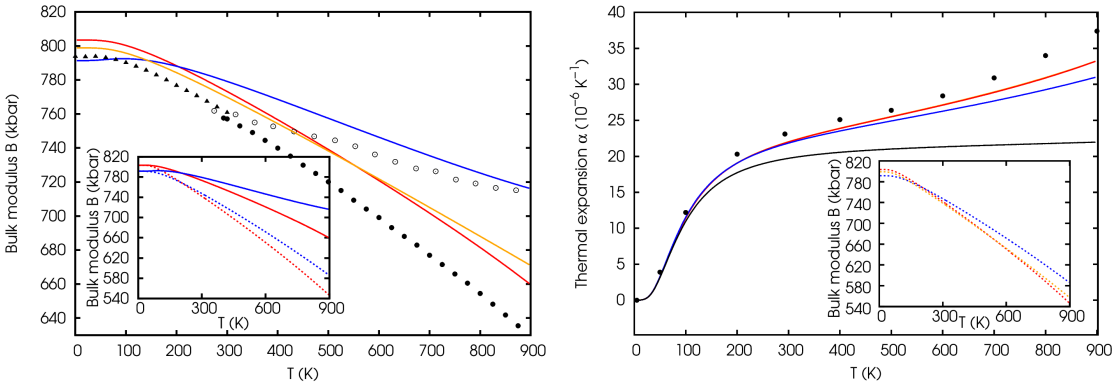

FIGURE 3.7: Left. Temperature dependent adiabatic bulk modulus of Al. QHA (red curves), QSA (blue curves) and experimental points: Kamm and Alers [74] (full triangles), Gerlich and Fisher [80] (full circles), Tallon and Wolfenden [81] (open circles). The orange curve is the bulk modulus obtained from the Murnaghan equation. In the inset a comparison between the adiabatic (continuous lines) and the isothermal (dashed lines) bulk moduli. Right. Thermal expansion of Al: computed as Eq. 2.44 (orange curve). The other curves are computed by using Eq. 2.50 with a bulk modulus derived from ECs (Eq. 2.56): temperature dependent ECs computed via QHA (red curve) or QSA (blue curve) and $T = 0K$ ECs (black curve). The experimental points are taken from [83]. In the inset the isothermal bulk moduli are reported: QHA (red dashed lines), QSA (blue dashed line) and obtained from Murnaghan equation (orange dashed line).

The result of the TE derived from QHA TDECs (red curve) gives a remarkable agreement with the reference with an APE $\approx 0.2\%$, while an APE $\approx 2.4\%$ is found using QSA. Finally, the calculation of the TE with a fixed bulk modulus obtained from the $T = 0$ K ECs has an APE $\approx 17.2\%$, even if the agreement remains good at temperature up to 100 K.

3.2.2.3 Silver

In Figure 3.8 we report the PBEsol TDECs of Ag with the same meaning for the lines and colors of previous plots. The points are taken from ultrasonic experiments that provide adiabatic ECs and must be compared with the continuous lines: reference [75] is in the range of temperatures 4.2 K - 300 K (full triangles), reference [84] is in the range 79 K - 298 K (open triangles) and reference [85] is in the range

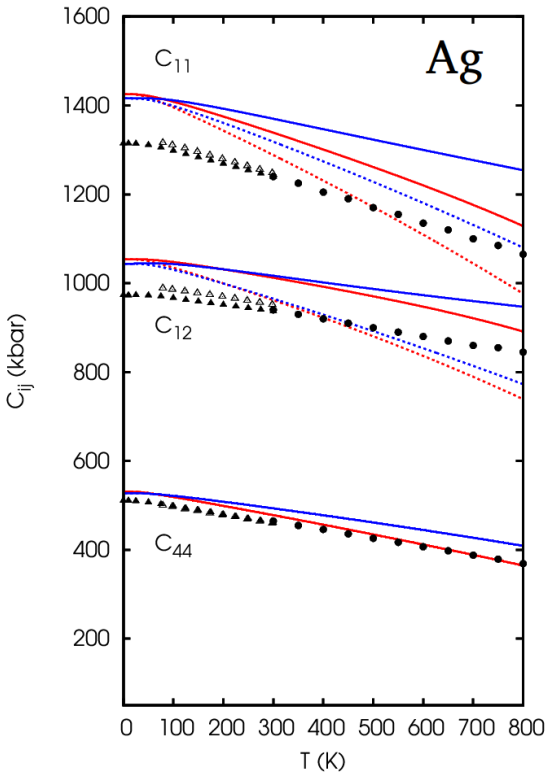

FIGURE 3.8: PBEsol temperature dependent elastic constants of Ag. Quasi-harmonic approximation (red curves) is compared with quasi-static approximation (blue curves). The adiabatic (continuous lines) and isothermal (dashed lines) elastic constants are reported. Experimental data are taken from Neighbours and Alers [75] (full triangles), Mohazzabi [84] (open triangles) and Chang and Himmel [85] (circles).

300 K - 800 K (circles). Since the two sets of data below room temperature are very similar, in the following we limit the comparison with the first one. The percentage differences between QHA ECs (red continuous curves) and experimental points at $T = 0$ K are about 8 % for C_{11} and C_{12} and 4 % for C_{44}. Almost the same values are found for QSA ECs. Our values of the $T = 0$ K ECs are between the ECs of Refs. [38] and Ref. [39] both using GGA functionals and are slightly closer to experiment (see Table 3.2). The experiments show a softening of $\approx 19\%$ for C_{11}, $\approx 13\%$ for C_{12}, and $\approx 28\%$ for C_{44} in the temperature range 0 K - 800 K. In the same range of temperatures the theoretical softening of the adiabatic ECs is $\approx 21\%$ (QHA) and $\approx 11\%$ (QSA) for C_{11}, $\approx 15\%$ (QHA) and $\approx 9\%$ (QSA) for C_{12} and $\approx 31\%$ (QHA)

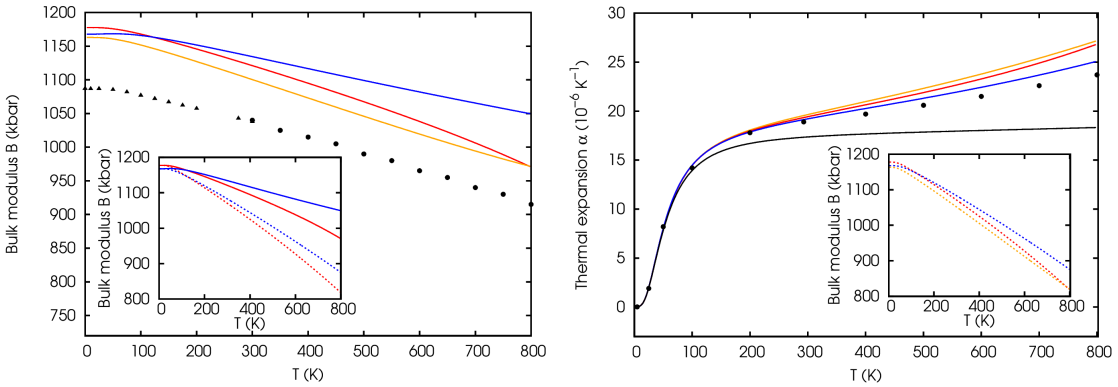

FIGURE 3.9: Left. Temperature dependent adiabatic bulk modulus of Ag. QHA (red curves), QSA (blue curves) and experimental points [75] (full triangles), [84] (open triangles) and [85] (circles). The orange curve is the bulk modulus obtained from the Murnaghan equation. In the inset we compare the adiabatic (continuous lines) and the isothermal (dashed lines) bulk moduli. Right. Thermal expansion of Ag: computed as Eq. 2.44 (orange curve). The other curves are computed by using Eq. 2.50 with a bulk modulus derived from ECs (Eq. 2.56): temperature dependent ECs computed via QHA (red curve) or QSA (blue curve) and T=0 ECs (black curve). The experimental points are taken from [83]. In the inset the isothermal bulk moduli are reported: QHA (red dashed line), QSA (blue dashed line) and obtained from Murnaghan equation (orange dashed line).

and $\approx 23\%$ (QSA) for C_{44}. As for Si and Al the QHA reproduces slightly better the experimental trend.

We report in Figure 3.9 (left) the adiabatic bulk modulus of Ag computed with the different sets of ECs and the one derived from the Murnaghan equation (orange curve). The QHA bulk modulus is the closest to the orange curve, even if a small artificial descent is present in the high temperature part of the red curve (> 600 K). This may be due to a not perfect convergence in the **k**-point sampling but since the variation is small and the selected **k**-point grid was already close to the largest one we could afford we have not investigated further this issue. Finally we check the consistency of our ECs by computing the TE using the Grüneisen's formula and the isothermal bulk modulus obtained from the TDECs (the comparison between adiabatic and isothermal bulk moduli is shown in the inset). The APE is computed as for the previous two materials. The TE computed using the isothermal

bulk modulus derived from the Murnaghan equation (orange dashed curve in the inset) has an APE of the order of -0.01%, being practically identical to the finite differences method. Also QHA TDECs give a very good agreement, the associated APE is $\approx 1.4\%$, while the QSA TE has slightly smaller values at higher temperatures with an APE of $\approx 4.2\%$. Finally, by using a temperature independent bulk modulus obtained from the $T = 0$ K ECs (black line) the TE is more distant from the reference with an APE $\approx 18.4\%$.

3.3 Platinum, palladium, copper and gold

In this section we apply the previous method to calculate the TDECs of the transition metals Pt and Pd and the noble metals Cu and Au. We will focus on the effects of electronic thermal excitation and the exchange-correlation functional. In Appendix C we report an example of convergence tests done for the $T = 0$ K ECs of these materials.

3.3.1 Accounting for thermal electronic excitation

The procedure for computing TDECs depicted in Fig. 3.2 is unchanged but we have to provide, in both calculations, the files with the electronic free-energy so that the program can add it to the Helmholtz free-energy for the TDECs calculation (Fig. 3.2 left) and for the calculation of the thermal expansion and other anharmonic properties (Fig. 3.2 right).

The files with the electronic free-energies (and the other electronic thermodynamic properties) are generated with the following two-steps procedure. For the TDECs, the electronic band structures at $T = 0$ K and density of states are computed for all

the strained geometries. For the thermal expansion calculation they are computed for all the reference configurations. Then, the electronic thermodynamic properties are computed via the Eqs. 2.59, 2.60, 2.61, printed in files and plotted.

3.3.2 Computational parameters

The exchange and correlation functional is approximated by the LDA [48] and the GGA-PBEsol [50] for all metals. For Cu we also use the GGA-PBE [49] functional (which, in this case, gives the best agreement with the experimental $T = 0$ K ECs). The pseudopotentials are reported in the note[2]. The cutoff for the wave functions (charge density) was 60 Ry (400 Ry) for Pd, 45 Ry (300 Ry) for Pt, 60 Ry (1200 Ry) for Cu and 60 Ry (400 Ry) for Au. The presence of the Fermi surface has been dealt with by a smearing approach [51] with a smearing parameter $\sigma = 0.005$ Ry for Pd and Pt and $\sigma = 0.02$ Ry for Cu and Au. The **k**-point mesh was $40 \times 40 \times 40$ (except for PBEsol Au, for which a mesh $48 \times 48 \times 48$ has been used). DFPT was used to calculate the dynamical matrices on a $8 \times 8 \times 8$ **q**-point mesh for Pd and Pt (corresponding to 29 special **q**-points for configurations strained with ϵ_A, 59 **q**-points for ϵ_E and 65 for ϵ_F) and $4 \times 4 \times 4$ **q**-point mesh for Cu and Au (corresponding to 8 **q**-points for configurations strained with ϵ_A and 13 **q**-points for those strained with ϵ_E and ϵ_F). For Pd and Pt a thicker **q**-points mesh was necessary due to the presence of Kohn anomalies [86]. For all materials the dynamical matrices have been Fourier interpolated on a $200 \times 200 \times 200$ **q**-point mesh to evaluate the vibrational free-energy. The grid of the reference geometries was centered at the minimum of the total energy as reported in Tab. 3.3 except for the LDA study of Pt that was

[2]For palladium we used `Pd.pz-n-kjpaw_psl.1.0.0.UPF` and `Pd.pbesol-n-kjpaw_psl.1.0.0.UPF`. For platinum `Pt.pz-n-kjpaw_psl.1.0.0.UPF` and `Pt.pbesol-n-kjpaw_psl.1.0.0.UPF`. For copper `Cu.pz-dn-kjpaw_psl.1.0.0.UPF`, `Cu.pbe-dn-kjpaw_psl.1.0.0.UPF` and `Cu.pbesol-dn-kjpaw_psl.1.0.0.UPF`. For gold we used `Au.pz-dn-kjpaw_psl.0.3.0.UPF` and `Au.pbesol-dn-kjpaw_psl.0.3.0.UPF`.

centered at $a_0 = 3.916$ Å. We used 7 reference geometries separated by $\Delta a = 0.07$ a.u. for all metals except for Pt where we used $\Delta a = 0.0233$ a.u. for LDA and $\Delta a = 0.03$ a.u. for PBEsol for the presence of unstable strained configurations with imaginary phonon frequencies at too large lattice constants. We used 6 strained configurations for each type of strain with a strain interval $\delta\epsilon = 0.005$. In total we computed the phonon dispersions on 126 geometries for each material and functional in addition to those computed on the reference configurations required to compute $a(T)$ and the thermal expansion. For the electronic calculation we computed the bands in all the reference configurations (to include the effect on $a(T)$) and in all the strained ones (to include it in the TDECs). The **k**-point mesh for the electronic DOS calculations was $48 \times 48 \times 48$. We use a Gaussian smearing with a smearing parameter of 0.01 Ry. In order to fit the free-energy as a function of the strain we used a polynomial of degree two because, although the use of a fourth-degree polynomial could introduce some differences, it requires higher cutoffs to converge the $T = 0$ K ECs. To interpolate the ECs computed at the different reference configurations and calculate them at the temperature dependent geometry we use a fourth-degree polynomial.

The DFPT finite-temperature approach was applied to evaluate the ECs of Pt at the temperatures $T_{FD} = 800$ K (with a Fermi-Dirac smearing $\sigma_{FD} \approx 0.005$ Ry) and $T_{FD} = 1000$ K ($\sigma_{FD} \approx 0.0063$ Ry). For this purpose the TDECs calculation was set in a single reference geometry with the lattice constant at the considered temperature: 7.429 a.u. for 800 K and 7.46 a.u. for 1000 K.

3.3.3 Results

In Tab. 3.3, we report the zero temperature lattice constants, elastic constants, and bulk moduli of the four metals calculated with different exchange and correlation functionals. We compare them with experiments and previous theoretical works. As usually found, PBEsol gives slightly larger lattice parameters than LDA and smaller $T = 0$ K ECs. PBEsol reproduces the experimental ECs of Pd and Pt better than LDA with errors smaller than $\approx 5\%$ for all the ECs, compared to LDA errors in the range $10 - 18\%$ in Pd and from $\approx 9\%$ (C_{11} and C_{44}) to $\approx 12\%$ (C_{12}) in Pt. On the other hand, the experimental ECs of Cu are well reproduced by PBE with errors equal or smaller than 3%, compared with errors larger than 15% for the other functionals. The LDA and PBEsol have almost the same accuracy in reproducing the $T = 0$ K C_{11} and C_{44} of Au (with errors of $\approx 5\%$ and $\approx 18\%$, respectively), while for C_{12} PBEsol has an error of $\approx 3\%$ and LDA an error of $\approx 10\%$. The differences found for the LDA ECs of Pd with respect to those of Ref. [62] are $\approx 2\%$ for C_{11}, $\approx 29\%$ for C_{12} and $\approx 10\%$ for C_{44}. For Pt, comparing our LDA ECs with the calculations of Ref. [88] we found differences of $\approx 4\%$ for C_{11}, $\approx 3\%$ for C_{12} and $\approx 8\%$ for C_{44}; while the comparison of our PBEsol ECs with the corrisponding PBEsol all-electrons calculation of Ref. [12] gives differences of $\approx 1\%$ for C_{11}, $\approx 5\%$ for C_{12} and C_{44}. The differences found for the LDA-ECs of Cu with respect to those of Ref. [9] are $\approx 28\%$ for all ECs, while the differences between our PBE ECs with the other GGA ECs of Refs. [90, 91] are smaller than $\approx 3\%$ for C_{11} and C_{12} and $\approx 5 - 6\%$ for C_{44}. Our PBEsol ECs of Au are close to the GGA estimates of Ref. [9] with differences of $\approx 5\%$ for C_{11} and C_{12} and $\approx 3\%$ for C_{44}. For reference, in Pd, Pt, and Au we report GGA ECs found in literature. As expected, they are smaller than our LDA and PBEsol ECs. They shows some differences with our PBE estimates, which are, however, very close to the PBE ECs reported in the Materials Project

TABLE 3.3: ECs at $T = 0$ K computed with LDA, PBEsol and PBE exchange and correlation functionals compared with previous theoretical works and experimental data. The equilibrium lattice constants (a_0) are in Å while the ECs and the bulk moduli B are in kbar. The bulk modulus is $B = \frac{1}{3}(C_{11} + 2C_{12})$.

	a_0	C_{11}	C_{12}	C_{44}	B
Palladium					
LDA	3.85	2696	2071	788	2279
PBEsol	3.88	2445	1861	740	2056
PBE	3.95	2010	1532	606	1690
LDA[a]	3.90	2743	1463	716	1890
GGA[b]	3.94	2548	1358	587	1755
Expt.[c]	3.8896(2)	2341(27)	1761(27)	712(3)	1954
Platinum					
LDA	3.90	3800	2759	802	3106
PBEsol	3.92	3553	2581	764	2905
PBE	3.98	3039	2234	615	2502
LDA[d]	3.91	3645	2665	736	2992
PBEsol[e]	3.91	3595	2456	858	2836
GGA[d]	3.99	3063	2133	730	2443
Expt.[f]	3.92268(4)	3487(130)	2458(130)	734(20)	2801(9)
Copper					
LDA	3.52	2349	1666	998	1894
PBEsol	3.56	2100	1480	938	1687
PBE	3.63	1775	1238	793	1417
LDA[g]	3.64	1678	1135	745	1316
GGA[h]	3.63	1745	1253	752	1417
GGA[i]	3.63	1800	1200	840	1400
Expt.[l]	3.596	1762.0	1249.4	817.7	1420.3
Gold					
LDA	4.05	2120	1873	373	1955
PBEsol	4.10	1926	1651	366	1743
PBE	4.16	1544	1327	268	1389
GGA[g]	4.07	2021	1742	379	1835
PBE[m]	4.19	1478	1435	387	1449
Expt.[n]	4.062	2016.3	1696.7	454.4	1803.2

[a] Ref. [62], [b] Ref. [87]
[c] Ref. [57] (room temperature a_0, $T = 0$K extrapolation of ECs),
[d] Ref. [88], [e] Ref. [12] (all electrons),
[f] Reference [89] (room temperature results, most recent work)
[g] Reference [9], [h] Reference [90], [i] Reference [91]
[l] Ref. [92] for a_0 and Ref. [93] for the ECs ($T = 0$K extrapolation),
[m] Ref. [94], [n] Ref. [92] for a_0 and Ref. [75] for the ECs ($T = 0$K extrapolation)

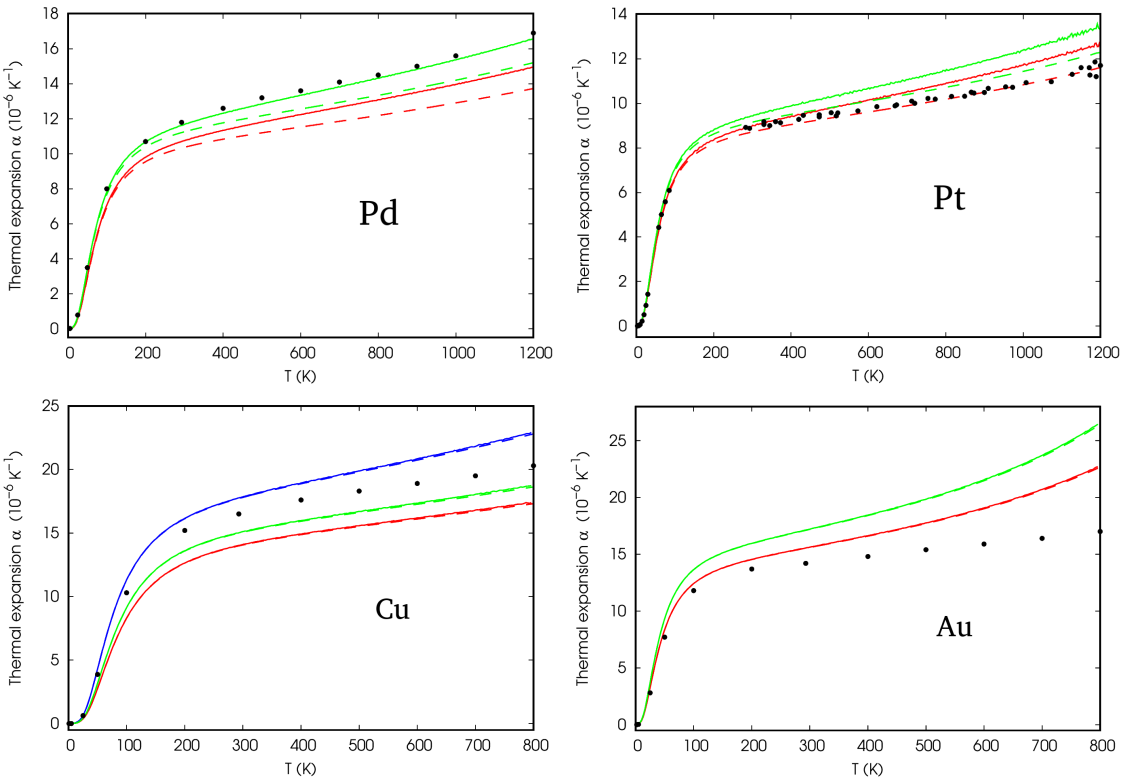

FIGURE 3.10: Thermal expansion coefficient of Pd (top-left), Pt (top-right), Cu (bottom-left) and Au (bottom-right). LDA (red curves) is compared with PBEsol (green curves) and, only for Cu, with PBE (blu curve). The results obtained with the total free energy (continuous line) are compared with those in which the contribution of electronic excitations is neglected (dashed lines). Experimental data from Ref. [83] (points).

database [22] and computed with the PAW method.

We pass now to describe the TE calculation where we estimate the effect of electronic excitations. The TE of the four metals are in Fig. 3.10 with the different exchange and correlation functionals: LDA (red), PBEsol (green) and PBE (blue). The TE computed including or not the electronic contribution is reported in continuous or dashed lines, respectively. For Pd, above RT, the PBEsol functional gives a very good agreement with the experimental points when the electronic effect is taken into account while the LDA estimates are smaller. For Pt, the LDA with the electronic effect is close to the experimental points (that are, however, more scattered) until about 400 K and, at larger temperature, it is larger. The PBEsol

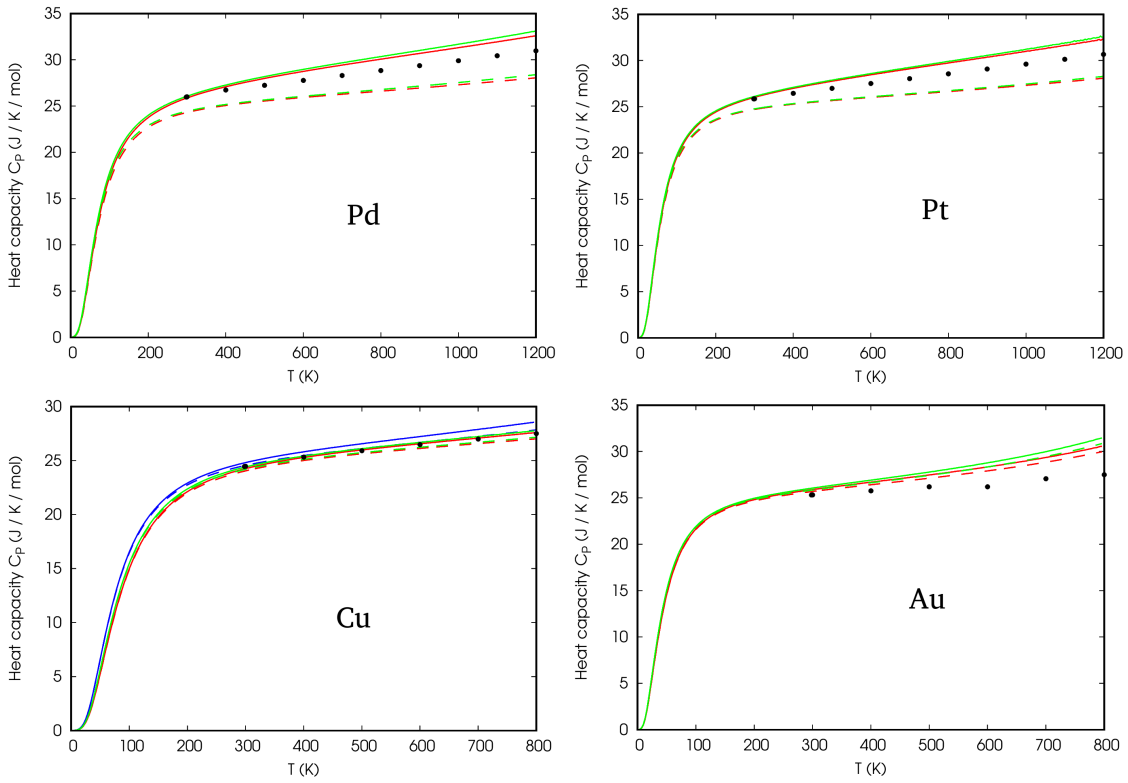

FIGURE 3.11: Isobaric specific heat of Pd (top-left), Pt (top-right), Cu (bottom-left) and Au (bottom-right). LDA (red curves) is compared with PBEsol (green curves) and, only for Cu, with PBE (blu curve). The results obtained with the total free-energy (continuous line) are compared with those in which the contribution of electronic excitations is neglected (dashed lines). Experimental data from Ref. [95] (points).

estimate is even larger. The electronic effect in the thermal expansion of Cu and Au does not produce any visible contribution in the scale of the plots. In Fig. 3.11 the isobaric heat capacity are reported and compared with the experimental data of Ref. [95]. The same convention of the TE for lines color and types is adopted. The different exchange and correlation functionals give almost the same temperature dependence in all cases. Again, the effect of thermal electronic excitation is strong in Pd and Pt, very small for Cu and Au. Both LDA and PBE TEs and heat capacities are in reasonable agreement with those of Ref. [29].

In Figs. 3.12, 3.13, 3.14, 3.15 we report the TDECs of the four metals. For each plot we follow the same color-line convention: Red indicates LDA estimates, green

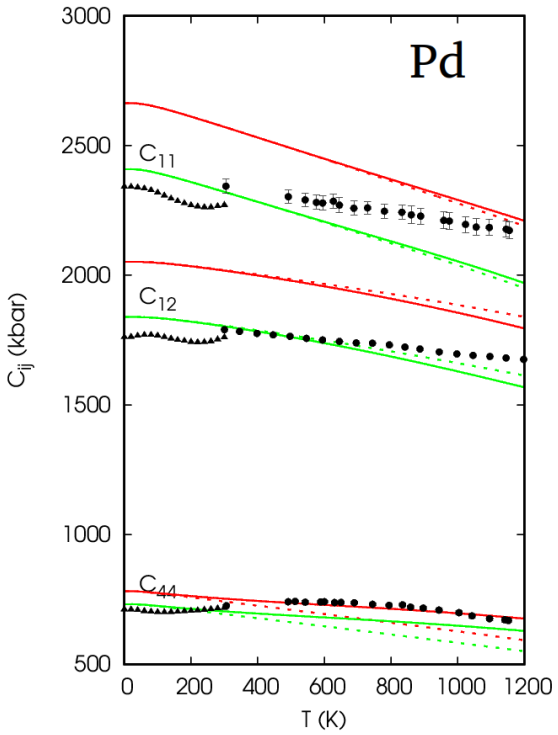

FIGURE 3.12: Quasi-harmonic adiabatic elastic constants of Pd. LDA (red curves) is compared with PBEsol (green curves). The results obtained with the total free energy (continuous lines) are compared with those in which the contribution of electronic excitations is neglected (dashed lines). Experimental data are taken from Rayne [57] (black triangles) and [59] (black circles).

PBEsol and blue, present only in Cu, PBE. The continuous lines are computed by considering all contributions in the Helmholtz free-energy, while the dashed lines are obtained neglecting the contribution of the electron thermal excitations. Black points are the experimental data.

The TDECs of Pd are shown in Fig. 3.12. Two experimental data-set are reported. The variation of the experimental ECs of Ref. [57] in the range $0-300$ K is 3% for C_{11}, about 0% for C_{12} and -1% for C_{44} with respect to the 0 K ECs. The corresponding LDA (PBEsol) variations in the same range of temperature are 3.7% (4.5%) for C_{11}, 2% (2%) for C_{12} and 3.8% (3.8%) for C_{44}. In the range $T = 300-1200$ K the variations in the data of Ref. [59] are 7.3% for C_{11}, 6.4% for C_{12} and 7.8%

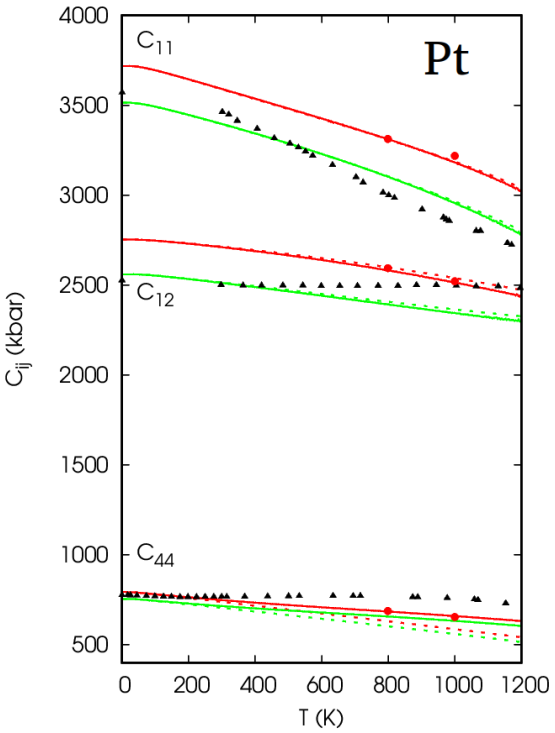

FIGURE 3.13: Quasi-harmonic adiabatic elastic constants of Pt. LDA (red curves) is compared with PBEsol (green curves). The results obtained with the total free-energy (continuous line) are compared with those in which the contribution of electronic excitations is neglected (dashed lines). The red circles at 800K and 1000K are computed within the LDA by using the Fermi-Dirac occupations. Experimental data are taken from Collard and McLellan [60] (black triangles).

for C_{44}, while the corresponding theoretical softenings are 15% for C_{11}, 13% for C_{12}, 11% for C_{44} for both functionals. Hence, both functionals give a similar temperature dependence. At room temperature the details of the experimental anomalies are not reproduced and above room temperature the theoretical softening is larger than the experimental one. The electronic effect is very small in C_{11} and C_{12} but leads to appreciable modifications of C_{44} which becomes closer to the experiment. As expected, the electronic contribution increases with temperature and influences the softening of C_{44} that without the electronic effect would be 20% in the range $300 - 1200$ K.

The TDECs of Pt are reported in Fig. 3.13. From $T = 0$ K to $T = 1200$ K the

experimental ECs decrease of about 24% for C_{11}, about 2% for C_{12} and about 6% for C_{44}. The corresponding theoretical softening for LDA (PBEsol) are 18% (20%) for C_{11}, 11% (10%) for C_{12} and 19% (19%) for C_{44}. Hence, the variation of C_{11} is well reproduced while the other two ECs softenings are overestimated. As found for Pd, the electronic contribution is important and improves the comparison with the experiment only for the C_{44} EC: without the electronic effect the softening would be $\approx 30\%$. However, it can not describe the anomalies. In order to further investigate the trend of the ECs of Pt we also considered the effect of the electronic excitation on the phonon frequencies for the temperatures $T = 800$ K and $T = 1000$ K with the method explained in the previous section (results are reported in red circles in the plot, only for the LDA case). The red points are exactly over our curves (apart for a slight deviation in the C_{11} at 1000 K). This fact points out that the electron-phonon interactions that modify the phonon frequencies has negligible consequences on the TDECs. We observe that our estimate of the electronic contribution is smaller than the one of Ref. [61] even for the C_{44}. In our calculation the largest contribution is the vibrational one which always decreases the ECs as the temperature increases.

The results of Cu are shown in Fig. 3.14. Since the two different experimental set of data are smoothly connected we report the whole softening in the range of temperature $T = 0 - 800$ K: 15% for C_{11}, 10% for C_{12} and 24% for C_{44}. The corresponding theoretical softening for LDA (PBEsol, PBE) are 13.5% (14%, 17%) for C_{11}, 7.6% (8.5%, 10.5%) for C_{12} and 21% (21%, 26%) for C_{44}. The temperature dependence is almost the same for LDA and PBEsol, slightly larger for PBE. The estimated softenings agree very well with the experiment. PBE results are the closest to the experiment, reflecting the trend of the $T = 0$ K ECs shown in Table 1. The electronic thermal excitations do not give any observable contribution in the whole range of temperature.

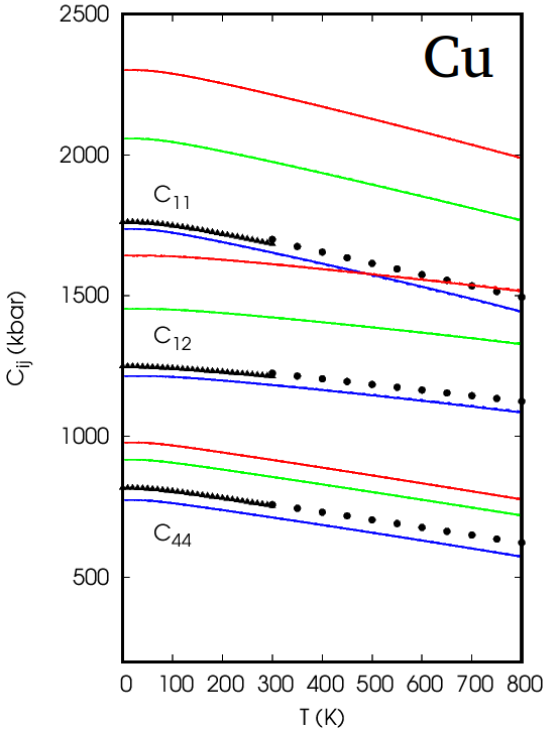

FIGURE 3.14: Quasi-harmonic adiabatic elastic constants of Cu. LDA (red curves), PBEsol (green curves) and PBE (blue) are compared. The results obtained with the total free-energy (continuous line) overlaps those in which the contribution of electronic excitation is neglected (dashed lines). Experimental data are taken from Overton and Gaffney [93] (black triangles) and Chang and Himmel [85] (black circles).

The TDECs of Au are shown in Fig. 3.15. As for Cu we consider the two experiments together: In the range of temperature from $T = 0$ K to $T = 800$ K the softenings are 13% for C_{11}, 11% for C_{12} and 22% for C_{44}. The corresponding softening for LDA (PBEsol) are 18% (22%) for C_{11}, 17% (20%) for C_{12} and 24% (29%) for C_{44}. The PBEsol softening is slightly larger than the LDA one and both functionals overestimate the experimental softening in particular for C_{11} and C_{12} with differences that increase from room temperature onward. As in Cu, the electronic thermal excitations do not give any observable contribution.

Finally, from the TDECs we can compute the bulk modulus by means of Eq. 2.56. The results are reported in Fig. 3.16.

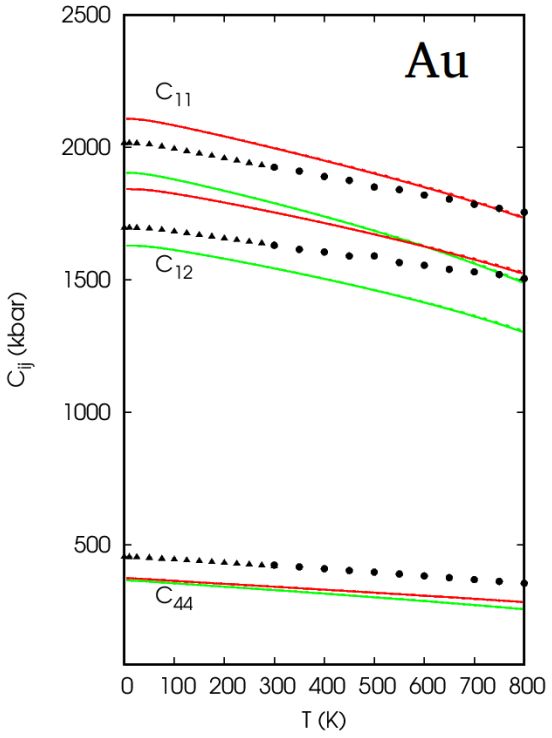

FIGURE 3.15: Quasi-harmonic adiabatic elastic constants of Au. LDA (red curves) and PBEsol (green curves) are compared. The results obtained with the total free-energy (continuous lines) overlaps with those in which the contribution of electronic excitation in neglected (dashed lines). Experimental data are taken from Neighbours and Alers [75] (black triangles) and Chang and Himmel [85] (black circles).

3.4 Boron arsenide

BAs has a zincblende cubic structure and belongs to the space group $F\bar{4}3m$ [64–66]. Recent measurements, supported by ab-initio calculations, range from the lattice constant and TE, to the band gap and refractive index, to the zero-temperature ECs and bulk modulus [96–98]. Here, we apply the tools presented in the previous sections to investigate the TDECs of BAs and its thermodynamic properties.

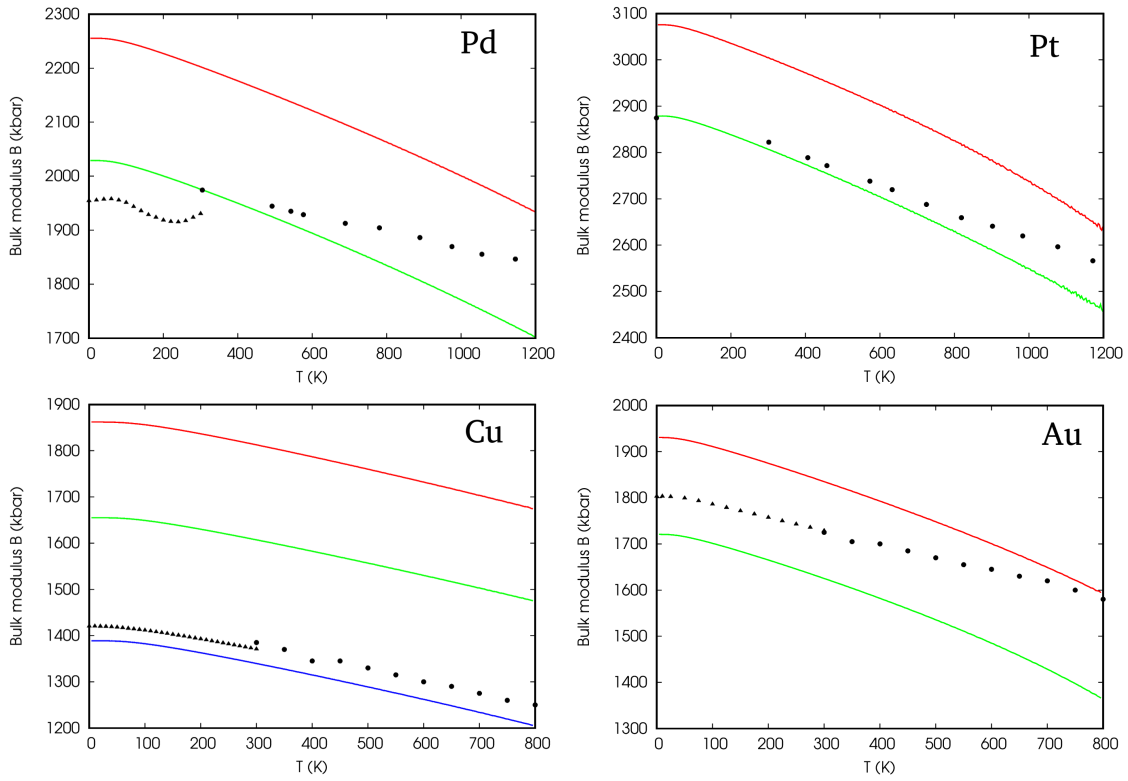

FIGURE 3.16: Bulk modulus of Pd (top-left), Pt (top-right), Cu (bottom-left) and Au (bottom-right). LDA (red curves) is compared with PBEsol (green curves) and, only for Cu, with PBE (blu curve). The results are obtained with the total free-energy including the electronic contribution. Experimental points (black) are adapted from those reported for the ECs.

3.4.1 Computational parameters

The exchange and correlation functional was approximated by the LDA which gives the best agreement between experimental and theoretical quantities especially for the $T = 0$ K ECs. We employed the PAW method and a plane waves basis set with pseudopotentials [52] from *pslibrary* [24]. The pseudopotentials `B.pz-n-kjpaw_psl.1.0.0.UPF` and `As.pz-n-kjpaw_psl.1.0.0.UPF` have been used for B and As, respectively. The wave functions (charge density) were expanded in a plane waves basis with a kinetic energy cut-off of 60 Ry (400 Ry), and a $16 \times 16 \times 16$ mesh of **k**-points has been used for the Brillouin zone integration. DFPT [14, 54]

was used to calculate the dynamical matrices on a $4 \times 4 \times 4$ **q**-points grid. The dynamical matrices have been Fourier interpolated on a $200 \times 200 \times 200$ **q**-points mesh to evaluate the free-energy. The grid of the reference geometries was centered at the $T = 0\ K$ lattice constant reported in Table 3.4. The number of reference geometries were 9 with lattice constants separated from each other by $\Delta a = 0.05\ a.u.$. In the ECs calculation the number of strained configuration was 6 for each type of strain with an interval of strains between two strained geometries of 0.005. In total we computed phonon dispersions for 162 geometries (in addition to the 9 phonon dispersions used for the $a(T)$ calculation). A second degree polynomial has been used to fit the energy (for the ECs at $T = 0$ K) or the free-energy (for the QHA TDECs) as a function of strain, while a fourth degree polynomial was used to fit at each temperature all the other quantities computed at the various reference geometries versus $a(T)$.

3.4.2 Results

In Table 3.4 we report the computed equilibrium lattice constant a_0 at $T = 0$ K both with and without the zero point energy (ZPE) and the RT value: the differences among them are of the order of hundredths of angstroms. The computed RT a_0 is in good agreement with the RT experiment [97] (the difference is smaller than $\approx$ 0.02 Å). The comparison with other computed a_0 is also reported: the LDA values agree within ≈ 1 %. This small differences depend primarily on the computational parameters chosen for the calculation and from the different pseudopotentials. The PBE values of a_0 are slightly larger than the LDA ones as usually found with the functionals that use the GGA. In Table 3.4 we also report the calculated values of the elastic constants together with other theoretical estimates available in the literature and the experimental values. The LDA values are closer to experiment, while the

TABLE 3.4: The computed ECs compared with some results available in the literature. The exchange and correlation functionals are indicated in the first column. The equilibrium lattice constant (a_0) is in Å while the ECs and the bulk modulus are in kbar. The experimental values are at T=298 K.

	a_0	C_{11}	C_{12}	C_{44}	B
LDA[a]	4.745	2897	768	1557	1477
LDA[b]	4.745	2897	768	1772	1477
LDA[c]	4.756	2828	759	1520	1449
LDA[d]	4.759	2807	754	1507	1438
LDA[e]	4.7444	2940	806	1770	1500
LDA[f]		3012.6	772.3	1638.7	1519.1
LDA[g]	4.779	2863.88	709.63	1575.03	1427.72
LDA[h]	4.743	2950	780	1770	1500
LDA[i]	4.721	2914	728	1579	1457
PBE[l]	4.817	2630	620	1430	1290
PBE[h]	4.812	2750	630	1500	1340
PBE[m]	4.784	2510	798	1270	1370
Expt.[e]	4.78	2850	795	1490	1480

[a] This work at $T = 0$ K, [b] This work at $T = 0$ K with frozen ions,
[c] This work at $T = 0$ K + ZPE,
[d] This work at $T = 300$ K (adiabatic ECs), [e] Ref. [97], [f] Ref. [99], [g] Ref. [100]
[h] Ref. [101], [i] Ref. [102], [l] Ref. [96], [m] Ref. [103]

PBE calculations give smaller ECs, as usually found with the GGA functionals. At $T = 0$ K, the softening due to the ZPE is $\approx 2.4\%$ for C_{11}, $\approx 1.2\%$ for C_{12} and $\approx 2.4\%$ in C_{44}. As mentioned before, in our calculation we relax the ionic positions for each strained configuration at $T = 0$ K to get the relaxed-ions ECs. This is relevant only for C_{44} while for C_{11} and C_{12} the ionic positions are determined by symmetry. The frozen-ions results, obtained by a uniform strain of the atomic positions but no further relaxation, are also shown in Tab. 3.4: C_{44} is ≈ 14 % larger than the relaxed-ions value. Our theoretical $T = 300$ K values are in good agreement with experiment: C_{11} is smaller of ≈ 1.5 %, C_{12} is smaller of ≈ 5.1 % and C_{44} is larger of ≈ 1 %.

In Figure 3.17 the TDECs and the bulk modulus are reported. The red lines are the adiabatic ECs (or bulk modulus), while the blue lines are the isothermal ECs. Evaluating the percentage softening of ECs due to temperature as $\frac{C_{ij}(T=0\text{K}) - C_{ij}(T=1800\text{K})}{C_{ij}(T=0\text{K})} \times$

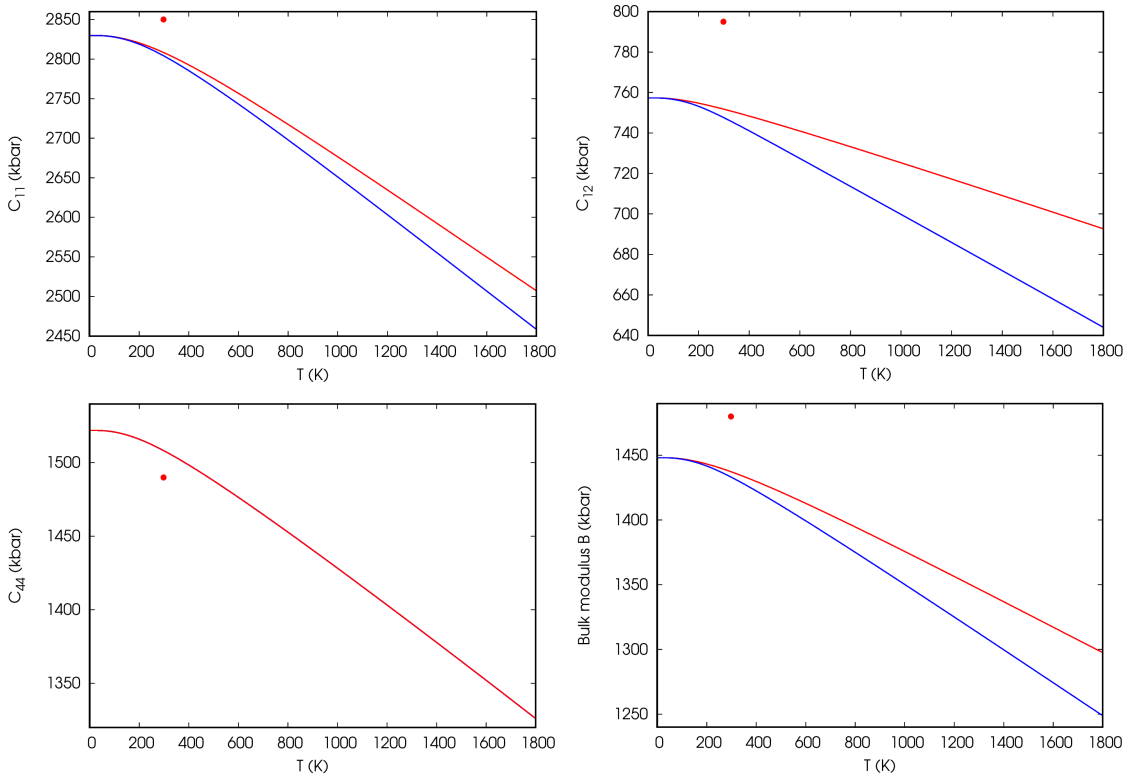

FIGURE 3.17: TDECs and bulk modulus of BAs: isothermal (blue) and adiabatic (red). RT experimental points from Ref. [97].

100, where the ZPE is included in $C_{ij}(T = 0\text{K})$ we find: ≈ 11 % (adiabatic) and ≈ 13 % (isothermal) for C_{11}, ≈ 9 % (adiabatic) and ≈ 15 % (isothermal) for C_{12} and ≈ 13 % for C_{44}. As far as we know, presently no experimental measurement of the TDECs is available to compare directly with our result, but in Ref. [97] the temperature dependence of the longitudinal sound velocity along the [111] direction was measured till ≈ 500 K. Using the adiabatic TDECs and the density ρ, this sound velocity can be written as [104]:

$$V_{long} = \left(\frac{C_{11} + 2C_{12} + 4C_{44}}{3\rho} \right)^{\frac{1}{2}}, \tag{3.1}$$

and in Fig. 3.18 we compare our theoretical estimate with experiment. We take into account the temperature dependence of the density due to TE effect. The use of a

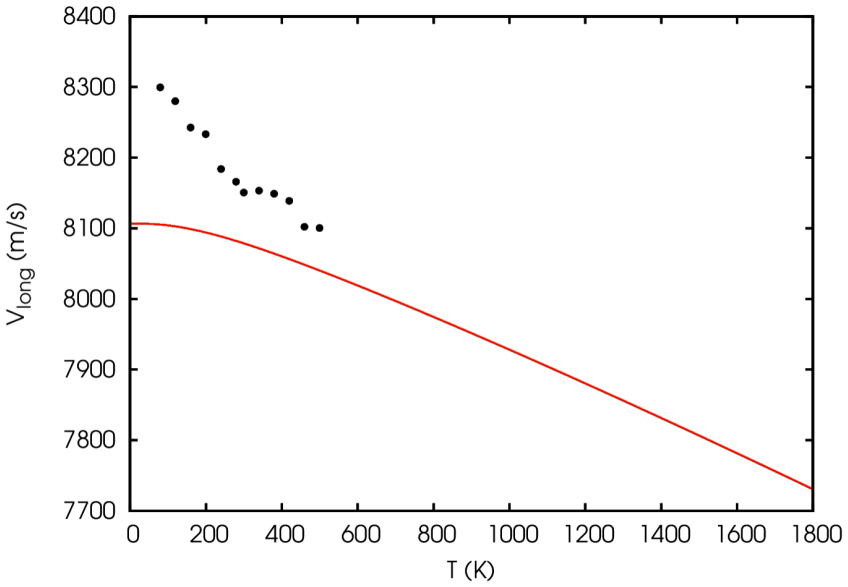

FIGURE 3.18: Longitudinal sound velocity in the [111] direction: experimental points (extrapolated from Ref. [97]) and this work (red curve).

temperature independent density in Eq. 3.1 (for instance the density at $T = 0$ K or $T = 300$ K) leads to an appreciably lower sound velocity above the room temperature (for instance at $T = 1500$ K the difference is ≈ 90 m/s). The theoretical values of the sound velocity as a function of temperature is in reasonable agreement with experiment in the analyzed range, but the experimental slope of the curve at low temperatures is not reproduced. The comparison improves above RT. We can also compare the TDECs of BAs with those of Si of Fig. 3.4 with the same functional LDA. ECs of Si are smaller, the $T = 0$ K values (with ZPE) are: $C_{11} = 1580$ kbar, $C_{12} = 639$ kbar and $C_{44} = 746$ kbar. In the range of temperature calculated for silicon ($0 - 800$ K) C_{11} and C_{12} decrease of about 7 % and C_{44} of 5 % (for both isothermal and adiabatic). In the same range of temperature the decrease of the ECs of BAs is slightly smaller: 3.8 % (adiabatic) and 4.5 % (isothermal) for C_{11}, 3.2 % (adiabatic) and 5.7 % (isothermal) for C_{12} and 4.5 % for C_{44}. We now present several other thermodynamic properties of BAs that have been calculated together with the TDECs. The TE and the temperature dependence of the lattice constant $a(T)$

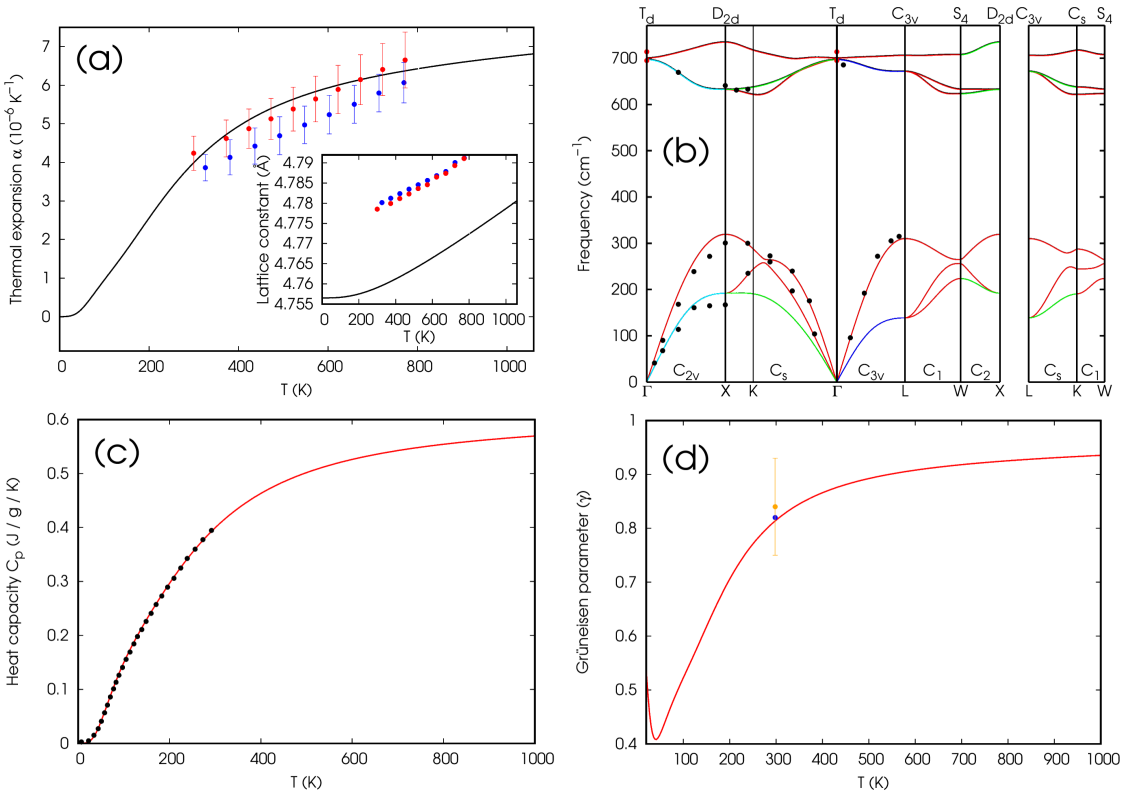

FIGURE 3.19: (a) Thermal expansion and temperature dependence of the lattice parameter (inset). Black lines represent this work, the points are experimental data: blue [97] and red [98]. (b) Phonon dispersion curves at $T = 300$ K (colored lines) and experimental points: black [105] and red [106]. The colours of the phonon branches indicate their symmetry (as explained in the thermo_pw documentation). Phonons curves at $T = 0$ K (black lines, barely visible only in the optical branches). (c) Computed isobaric heat capacity (red line) and comparison with experiment (points) adapted from Ref. [98]. (d) Average Grüneisen parameter: this work (red curve), experimental points from [97] (blue) and [98] (orange).

are shown in Figure 3.19 in the range of temperature $0 - 1100$ K. We compare our numerical result (black line) with two recent measurements in the temperature range $300 - 773$ K [98] (red points) and $321 - 773$ K (blue points) [97]. The experimental $a(T)$ is higher than the theoretical one by approximately 0.02 Å, but the temperature dependence is reproduced correctly as visible in the TE plot reported in the same figure. In the experimental temperature range, the experimental $a(T)$ are both linear with T but the slope of the red points is slightly larger and more in agreement with our calculation. This behavior is reflected in the TE: the TE of Ref. [98] agrees with

ours within experimental uncertainties while the TE of Ref. [97] has slightly smaller values (although within the error bar of Ref. [98]). In particular the RT TEs are $4.0\times10^{-6}K^{-1}$ (this work), $(4.2\pm0.4)\times10^{-6}K^{-1}$ [98] and $3.85\times10^{-6}K^{-1}$ [97]. Other DFT-LDA estimates are: $4.0\times10^{-6}K^{-1}$ [98], and $3.04\times10^{-6}K^{-1}$ [107]. Molecular dynamic simulations produced the result $4.1\times10^{-6}K^{-1}$ [108]. A much larger value has appeared recently $10.9\times10^{-6}K^{-1}$ [109] by using DFT method within the GGA, quite far from experiment. The phonon frequencies computed at the different geometries are interpolated at $T = 300$ K and the result is shown in Figure 3.19b (colored lines). The phonons are compared with RT measurements obtained from inelastic X-ray scattering [105] and Raman spectroscopy [106] (points). As already found in Refs. [107, 105] the agreement between theory and experiment is quite good. The difference between RT and $T = 0$ K phonons (black lines) is only barely visible in the optical branches. The isobaric heat capacity is shown in Figure 3.19c. The points indicate the temperature dependence of experimental data [98] that we extrapolated from the plot. The agreement is very good. The temperature dependence of the average Grüneisen parameter is reported in Figure 3.19d. We also report the RT experimental values of Refs [97] (blue point) and [98] (orange point). The experimental uncertainty of the first point is not known, but it is very close to our curve. The second point is in agreement with our estimate within the experimental error bar.

Chapter 4

Finite-temperature atomic relaxation

Si and BAs with diamond and zincblende structures, respectively, have two atoms per cell and, when a strain is applied to the solid and the atomic coordinates are uniformly strained, forces might appear on atoms. If not in high symmetry positions the atoms relax in a different configuration. In this case the *frozen-ions* elastic constants calculated by uniformly straining the atoms without further relaxation might differ from the *relaxed-ions* ECs where the atoms are allowed to relax. For diamond or zincblende crystals the rhombohedral strain ϵ_F (defined in section 2.3.3.1) allows an internal relaxation, providing a different value for the frozen-ions and relaxed-ions C_{44}. The differences introduced in the zero-temperature ECs are ~ 299 kbar (39%) for Si and ~ 212 kbar (14%) for BAs. In the previous calculations of the TDECs, this contribution was taken into account by allowing the atoms to relax at $T = 0$ K for each strained configuration. While this approach is consistent within the QSA, it is not within the QHA where the internal relaxation should be obtained from the minimum of the free-energy. In this chapter we present another method to estimate

the correction to the zero-temperature C_{44} by introducing the concept of internal strain that we will later extend to non-zero temperatures in order to evaluate the finite-temperature contribution of the internal relaxations in the TDECs of Si and BAs.

4.1 Internal strain at zero temperature

The total energy can be written as a function of both the atomic displacements $u_{s\alpha}$ and the strain $\epsilon_{\alpha\beta}$. If we consider a solid with vanishing initial forces on atoms and stress, its Taylor expansion in a.u. up to the second order is:

$$E(\{u_{s\alpha}\},\{\epsilon_{\alpha\beta}\}) = E_0 + \frac{1}{2}\sum_{s\alpha s'\beta} C_{s\alpha s'\beta} u_{s\alpha} u_{s'\beta} + \frac{\Omega}{2}\sum_{\alpha\beta\gamma\delta} C_{\alpha\beta\gamma\delta}\epsilon_{\alpha\beta}\epsilon_{\gamma\delta} - \sum_{s\alpha\beta\gamma} \Lambda_{s\alpha\beta\gamma} u_{s\alpha}\epsilon_{\beta\gamma}. \tag{4.1}$$

The second-order constants in the displacements define the interatomic force constants tensor[1]:

$$C_{s\alpha s'\beta} = \frac{\partial^2 E}{\partial u_{s\alpha}\partial u_{s'\beta}}, \tag{4.2}$$

related to the dynamical matrix $\frac{C_{s\alpha s'\beta}}{\sqrt{M_s M_{s'}}}$ at $\mathbf{q} = 0$. The term quadratic in the strain defines the elastic constants tensor of Eq. 2.32 and the mixed term in the displacement and strain defines the tensor:

$$\Lambda_{s\alpha\beta\gamma} = -\frac{\partial^2 E}{\partial u_{s\alpha}\partial \epsilon_{\beta\gamma}}, \tag{4.3}$$

whose components are called internal strain parameters.

[1]The interatomic force constants tensor $C_{s\alpha s'\beta}$ is not to be confused with the elastic constant tensor $C_{\alpha\beta\gamma\delta}$ in which there are not atomic labels indicated by the letters s or s'.

When $\Lambda_{s\alpha\beta\gamma}$ is non-zero the equilibrium displacement of atom s in the direction α is proportional to the strain:

$$u_{s\alpha} = \sum_{s'\beta\gamma\delta} C^{-1}_{s\alpha s'\beta} \Lambda_{s'\beta\gamma\delta} \epsilon_{\gamma\delta}, \tag{4.4}$$

where $C^{-1}_{s\alpha s'\beta}$ is the inverse of 4.2 that can be written as:

$$C^{-1}_{s\alpha s'\beta} = \sum_{\nu} \frac{e^{\nu}_{s\alpha} e^{\nu}_{s'\beta}}{\sqrt{M_s M_{s'}}\omega^2_{\nu}}. \tag{4.5}$$

The sum (related to $\mathbf{q} = 0$) is over all optical modes ν,[2] $e^{\nu}_{s\alpha}$ and $e^{\nu}_{s'\beta}$ are the α and β components of the eigenvectors of mode ν of atom s and s', respectively. M_s and $M_{s'}$ are the masses of atoms s and s', respectively. Finally, ω^2_{ν} are the eigenvalues relative to the mode ν. If we substitute the displacement 4.4 $u_{s\alpha}$ into the expansion 4.1 $E(\{u_{s\alpha}\}, \{\epsilon_{\alpha\beta}\})$ and we take the second derivatives with respect to strain, we get the ECs with the correction due to the internal strain relaxation:

$$C_{\lambda\mu\gamma\delta} = C^{FI}_{\lambda\mu\gamma\delta} - \Delta C_{\lambda\mu\gamma\delta}, \tag{4.6}$$

where

$$\Delta C_{\lambda\mu\gamma\delta} = \frac{1}{\Omega} \sum_{s\alpha} \Lambda_{s\alpha\lambda\mu} \Gamma_{s\alpha\gamma\delta}, \tag{4.7}$$

and

$$\Gamma_{s\alpha\gamma\delta} = \sum_{s'\beta} C^{-1}_{s\alpha s'\beta} \Lambda_{s'\beta\gamma\delta}. \tag{4.8}$$

The superscript FI in Eq. 4.6 means that the ECs are computed with the ions frozen in the uniformly strained configuration, the ECs without superscript are implicitly

[2] In principle the sum is extended aver all modes, including the zero-frequency acoustic ones for which the 4.5 diverges. We do not treat this divergence problem because the acoustic modes will not contribute in the rest of the formulation.

considered the ones computed with the relaxed ions. As defined before, Ω is the volume of the unit cell.

4.1.1 Zincblende structures

Now we consider the zincblende structure with two different atoms with masses M_1 and M_2 (the diamond case will be obtained for $M_1 = M_2$). For this crystal the following symmetry relation is valid for the internal strain tensor:

$$\Lambda_{1\beta\gamma\delta} = -\Lambda_{2\beta\gamma\delta} = \Lambda|\epsilon_{\beta\gamma\delta}|, \tag{4.9}$$

for which the internal strain of atom 1 is equal and opposite to the one of atom 2, Λ is a constant and $\epsilon_{\beta\gamma\delta}$ is the Levi-Civita tensor which is non-zero when all its indices are different from each other. Now, we expand the sum 4.8 over the two atoms and use the previous symmetry relation. We have:

$$\Gamma_{s\alpha\gamma\delta} = \sum_{\nu\beta} \frac{e^{\nu}_{s\alpha}}{\sqrt{M_s}\omega^2_{\nu}} \Lambda|\epsilon_{\beta\gamma\delta}| \left(\frac{e^{\nu}_{1\beta}}{\sqrt{M_1}} - \frac{e^{\nu}_{2\beta}}{\sqrt{M_2}} \right). \tag{4.10}$$

In the previous sum over the modes ν, only the optical modes at Γ contribute because within the acoustic modes the two atoms move in phase and are described by equal displacements ($\frac{e^{\nu}_{1\beta}}{\sqrt{M_1}} = \frac{e^{\nu}_{2\beta}}{\sqrt{M_2}}$) and, hence, the term in parenthesis is zero. In order to further develop the discussion we have to derive the components of the optical eigenvectors.

4.1.1.1 Displacement of optical modes

The atomic displacement (for atom s, mode ν and direction α) can be written as (at time $t = 0$):

$$u^{\nu}_{s\alpha} = A^{\nu} \frac{e^{\nu}_{s\alpha}}{\sqrt{M_s}}, \tag{4.11}$$

where A^{η} is the amplitude of the displacement with dimensions $[L] \times [M]^{\frac{1}{2}}$, M_s is the mass of atom s and $e^{\nu}_{s\alpha}$ is the eigenvector of the displacement. The motion of atoms at Γ within the optical phonon modes is opposite and proportional to the mass of the other atom. Moreover, the eigenvector $e^{\nu}_{s\alpha}$ satisfies the eigenvalues equation for this mode with angular frequency ω_{TO}:

$$\sum_{s'\beta} \frac{1}{\sqrt{M_s M_{s'}}} C_{s\alpha s'\beta} e^{\nu}_{s'\beta} = \omega^2_{TO} e^{\nu}_{s\alpha}. \tag{4.12}$$

To find analitically $e^{\nu}_{s'\beta}$ we can use the fact that the displacement is:

$$\mathbf{u}^{\eta} = u \cdot a \begin{pmatrix} M_2 \\ M_2 \\ M_2 \\ -M_1 \\ -M_1 \\ -M_1 \end{pmatrix}, \tag{4.13}$$

where u and a are adjustable parameters introduced to obtain the expression of the energy defined in Ref. [70] that we determine in the following. Starting from a generic eigenvector with equal components α for one atom and equal components β for the other atom, applying the normalization condition $3\alpha^3 + 3\beta^2 = 1$, and multiplying it by $\frac{A^{\eta}}{\sqrt{M_s}}$, we obtain the displacement and comparing with Eq. 4.13 we

get the following form for the eigenvector:

$$\mathbf{e}^{\eta}_{s\alpha} = \frac{1}{\sqrt{3}\sqrt{M_1+M_2}} \begin{pmatrix} \sqrt{M_2} \\ \sqrt{M_2} \\ \sqrt{M_2} \\ -\sqrt{M_1} \\ -\sqrt{M_1} \\ -\sqrt{M_1} \end{pmatrix}. \tag{4.14}$$

While the amplitude of the displacement is:

$$A^{\eta} = \sqrt{3}\sqrt{(M_1+M_2)(M_1M_2)}ua. \tag{4.15}$$

The vibrational energy of the mode is:

$$E = \frac{1}{2}\sum_{s\alpha s'\beta} u^{\eta}_{s\alpha} C_{s\alpha s'\beta} u^{\eta}_{s'\beta} = \frac{1}{2}|A^{\eta}|^2\omega^2_{TO}, \tag{4.16}$$

where the last expression is obtained with the substitution of the displacement 4.11 in the second term, the use of Eq. 4.12, and the normalization condition $\sum_{s\alpha}|e^{\eta}_{s\alpha}|^2 = 1$. Finally, by using Eq. 4.15, setting $a = \frac{1}{\sqrt{3}}\frac{1}{M_1+M_2}$, and defining the reduced mass $\mu = \frac{M_1M_2}{M_1+M_2}$, we get the energy in the form $E = \frac{1}{2}\mu\omega^2_{TO}u^2$ of Ref. [70]. With this

choice for a, the amplitude becomes $A^\eta = \sqrt{\mu}u$ and the displacement:

$$\mathbf{u}^\eta = \frac{u}{\sqrt{3}} \begin{pmatrix} \frac{M_2}{M_1+M_2} \\ \frac{M_2}{M_1+M_2} \\ \frac{M_2}{M_1+M_2} \\ -\frac{M_1}{M_1+M_2} \\ -\frac{M_1}{M_1+M_2} \\ -\frac{M_1}{M_1+M_2} \end{pmatrix}. \tag{4.17}$$

It is possible to shift the origin of the coordinates in such a way to fix the first atom in the origin. So, we subtract $\frac{M_2}{M_1+M_2}$ to the components of both atoms and we have:

$$\mathbf{u}^\eta = u' \begin{pmatrix} 0 \\ 0 \\ 0 \\ -1 \\ -1 \\ -1 \end{pmatrix} \tag{4.18}$$

where we also have defined $u' = \frac{u}{\sqrt{3}}$[3]. Hence, the internal relaxation of the system of two atoms can be described by keeping the first atom fixed and allowing the second to change its position.

4.1.1.2 Correction to elastic constants and extension to finite-temperature

Now, the expression of optical eigenvectors 4.14 can be substituted in Eq. 4.10. Rearranging the terms, and introducing the reduced mass μ we have:

[3]The original displacement 4.17 conserves the position of the center of mass $\mathbf{R}_{CM} = \frac{M_1\mathbf{u}_1+M_2\mathbf{u}_2}{M_1+M_2} = 0$, while in the case of the shifted displacements 4.18 we have $\mathbf{R}'_{CM} = \frac{-M_2\mathbf{u}_2}{M_1+M_2} \neq 0$.

$$\Gamma_{s\alpha\delta\epsilon} = \sum_{\nu\beta} \frac{e^{\eta}_{s\alpha}}{\sqrt{M_s}\omega^2_{\nu}} \frac{1}{\sqrt{3}} \Lambda |\epsilon_{\beta\gamma\delta}| \frac{1}{\sqrt{\mu}}. \tag{4.19}$$

Now, we insert it in Eq. 4.7, use 4.9, and the components of eigenvectors 4.14. We have:

$$\Delta C_{\lambda\mu\gamma\delta} = \frac{1}{3\Omega} \sum_{\alpha\beta\nu} \frac{\Lambda^2}{\omega^2_{\nu}\mu} |\epsilon_{\beta\gamma\delta}||\epsilon_{\alpha\lambda\mu}|. \tag{4.20}$$

The only non-zero correction is $\Delta C_{44} = \Delta C_{2323}$. In this case the sums in α and β of the module of the Levi-Civita tensor leads to unitary multiplicative factors, while the sum over the optical modes remains. The result is:

$$\Delta C_{44} = \frac{1}{3\Omega} \frac{\Lambda^2}{\mu} \sum_{\nu} \frac{1}{\omega^2_{\nu}} = \frac{\Lambda^2}{\Omega\ \mu\ \omega^2_{TO}}. \tag{4.21}$$

The previous equation gives the correction to the frozen-ions C_{44} elastic constant due to the atomic relaxation for diamond and zincblende cells with volume Ω with two atoms in the basis with reduced mass μ and transverse optical mode with angular frequency ω_{TO}. The internal strain Λ is given at $T = 0$ K by the derivatives of Eq. 4.3 of the total energy. We extend it at finite temperature by replacing in Eq. 4.3 the total-energy E with the Helmholtz free-energy F derived from phonons computed in the two dimensional grid of strains and displacements.

In literature the correction 4.21 is often written in terms of the so-called Kleinman parameter ξ. For example, by comparing the Eq. 4.21 with the correction ΔC_{44} reported in Ref. [70] in terms of ξ we have:

$$\xi = \frac{\Lambda}{\mu\ \omega^2_{TO} \frac{a_0}{4}}, \tag{4.22}$$

where a_0 is the lattice constant of the cubic crystal.

In the following sections we present our calculations of ΔC_{44} and ξ of Eqs. 4.21 and 4.22 by using the internal-strain formulation at $T = 0$ K for some materials with diamond and zincblende structures: Si, C, SiC, GaAs and BAs. Then, we compare with the ΔC_{44} calculated directly from atomic relaxation. Finally, we estimate the same correction at finite-temperature for the TDECs C_{44} of Si and BAs, computing the free-energy instead of the energy in the grid of strains and displacements.

4.2 Method and computational parameters

For the calculation of the internal strain Λ at $T = 0$ K (Eq. 4.3), the total-energy is computed in a two-dimensional grid of displacements and strains and is fitted with a second degree polynomial. The second derivative of the polynomial is evaluated analytically. The grid for the entries of the strain ϵ_F was $(-0.01, -0.005, 0, 0.005, 0.01)$ for all materials. The first atom is fixed in the origin and the displacements are set moving the second atom: the grid of displacements is centered at the equilibrium bond-length between the two atoms in the unstrained cubic cell $\frac{\sqrt{3}}{4}a_0$, where a_0 is the equilibrium lattice constant listed in Table 4.1, 5 displacements are chosen with distance $\Delta u = 0.05$ a.u.. We change simultaneously all the 6 components of the strain ϵ_F and all the 3 components of the second atom position along the direction [111] and compute the derivative of the total energy with respect these changes, getting the quantity Λ', different from the derivative 4.3 which is, instead, computed with respect to the change of the single components[4]. This translates in a multiplicative

[4]We compute the derivative with respect to the bond length $l = \sqrt{3}u_{21}$, $\frac{\partial E}{\partial l} = \frac{\partial E}{\partial u_{21}}\frac{\partial u_{21}}{\partial l} = \frac{1}{\sqrt{3}}\frac{\partial E}{\partial u_{21}}$: hence, a factor $\sqrt{3}$ is introduced. The other factor, introduced in the derivative with respect to strain, is given by the energy-strain expansion ϵ_F: $E(\epsilon_F) = E_0 + \sum_{ij}\frac{\partial E}{\partial \epsilon_{ij}}\epsilon_{ij} = E_0 + 6\frac{\partial E}{\partial \epsilon_{23}}\epsilon_{23}$.

factor such that: $\Lambda = \frac{\sqrt{3}}{6}\Lambda' = \frac{1}{2\sqrt{3}}\Lambda'$.

For this study, the exchange and correlation functional is approximated by the LDA [48] for all materials. The pseudopotentials used for each atomic species are reported in the note[5]. For all materials the cutoff for the wave functions (charge density) was 90 Ry (1300 Ry). The **k**-point mesh was $16 \times 16 \times 16$.

The finite-temperature correction was applied to Si and BAs for which the contribution of the vibrational free-energy is added in the calculation of Λ. Phonons dispersions are computed in the same two-dimensional grid of strains and displacements defined before. For both materials, DFPT [14, 54] was used to calculate the dynamical matrices on a $4 \times 4 \times 4$ **q**-points grid. The dynamical matrices have been Fourier interpolated on a $200 \times 200 \times 200$ **q**-points mesh to evaluate the free-energy. The grids of reference geometries for the TDECs calculation were centered at the $T = 0$ K lattice constant reported in Table 4.1 and set in the same way as done for the QHA TDECs (9 reference geometries with lattice constants separated from each other by $\Delta a = 0.05$ a.u.). The finite-temperature internal-strain calculation is done for all the reference configurations, the grid of displacements was centered in the new equilibrium position for each geometry. A second degree polynomial has been used to fit the Helmholtz free-energy as a function of the strain and displacements to determine Λ at each geometry and temperature. Λ is used to get the correction ΔC_{44} for the frozen-ions TDECs. For the calculation of ΔC_{44} we used the ω_{TO} corresponding to the considered volume $\{\Omega_i\}$. Then, a fourth degree polynomial was used to interpolate the $C_{44}(T, \Omega_i)$ at the $\Omega(T)$.

[5] We used pseudopotentials `Si.pz-nl-kjpaw_psl.1.0.0.UPF`, `C.pz-n-kjpaw_psl.1.0.0.UPF`, `Ga.pz-dnl-kjpaw_psl.1.0.0.UPF`, `As.pz-n-kjpaw_psl.1.0.0.UPF`, and `B.pz-n-kjpaw_psl.1.0.0.UPF`.

TABLE 4.1: Correction to the C_{44} EC: ΔC_{44}^{rel} is computed via direct atomic relaxation, ΔC_{44}^{IS} and ξ are computed by using the internal-strain formalism. C_{44}^{FI} is the frozen-ions EC. The lattice constant a_0 is in a.u., C_{44}^{FI} and ΔC_{44} are in kbar and ξ is dimensionless.

	a_0	C_{44}^{FI}	ΔC_{44}^{rel}	ΔC_{44}^{IS}	ξ
Si	10.2065	1060	299	299	0.54
C	6.6821	5971	72	74	0.13
SiC	8.1835	2840	313	320	0.42
GaAs	10.6085	799	218	209	0.55
BAs	8.9660	1772	212	213	0.38

4.3 Results

In Table 4.1 the equilibrium lattice constants a_0 of Si, C, SiC, GaAs and BAs are reported. The calculation of the correction ΔC_{44}^{rel} computed directly from atomic relaxation is in good agreement with the one computed with the internal-strain formalism: the largest difference is 9 kbar, found for GaAs. Also our Kleinman parameters are in reasonable agreement with those found in the literature. For Si we have $\xi = 0.54$ in good agreement with the calculation of Ref. [70] $\xi = 0.53$. Slightly larger differences for GaAs for which we have $\xi = 0.55$ while Ref. [70] reports $\xi = 0.48(2)$. Our estimate for SiC is $\xi = 0.42$ and is in between the results of Ref. [110] ($\xi = 0.38$) and of Ref. [111] ($\xi = 0.49$).

Now, we pass to describe the results obtained from the internal strain formalism at finite temperatures. In Fig. 4.1 we compare the C_{44} EC of Si as a function of temperature computed with frozen ions (blue line), with relaxed ions at $T = 0$ K (red line) reported in the plots of previous chapter and the new estimate with the ions relaxed at finite temperature (yellow line). The largest effect of the frozen-ions approximation is in the zero-temperature EC with a difference of ~ 300 kbar with respect the relaxed-ions case. A non-negligible effect is shown in the temperature dependence of the ECs as well. Indeed, the temperature dependence of the frozen-ions estimate (light-blue line) is larger than the other estimates showing a softening

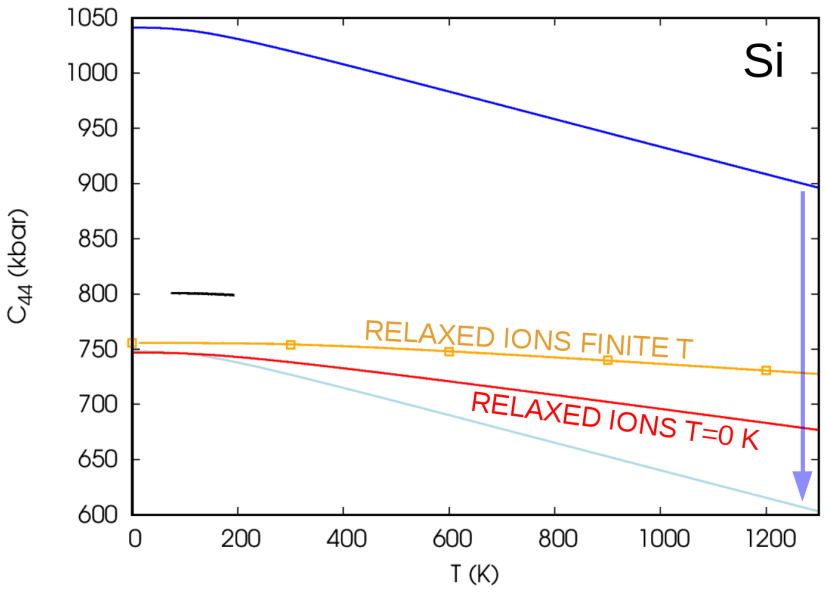

FIGURE 4.1: Temperature-dependent C_{44} elastic constant of Si within the QHA computed with frozen-ions (blue), relaxed-ions at $T = 0$ K (red) and relaxed-ions at finite T (yellow). The frozen-ions result is translated below (light-blue curve) to compare the temperature dependence with the relaxed-ions results. Experimental data are taken from McSkimin [73] (black line).

of $\sim$ 13% in the range of temperature $0 - 1200$ K, compared to $\sim$ 8.6% for the relaxed-ions at $T = 0$ K estimate, and $\sim$ 4.5% for the finite-temperature relaxed-ions estimate. There is a visible difference in the TDECs computed with zero-temperature and finite-temperature atomic relaxations that produces a difference in the softening of $\sim$ 4% in the range of temperatures considered. We also note that the differences introduced by the finite-temperature atomic relaxation increases with temperature.

In Fig. 4.2 we report the C_{44} EC of BAs, the colors have the same meaning as before. In the range of temperature $0 - 1200$ K the softening of the C_{44} EC is: $\sim$ 10% with frozen-ions, $\sim$ 8% with the zero-temperature atomic relaxation and $\sim$ 7% for the finite-temperature one. Hence, the effect of finite-temperature relaxation is smaller than the one found for Si but it is still visible and increases with temperature.

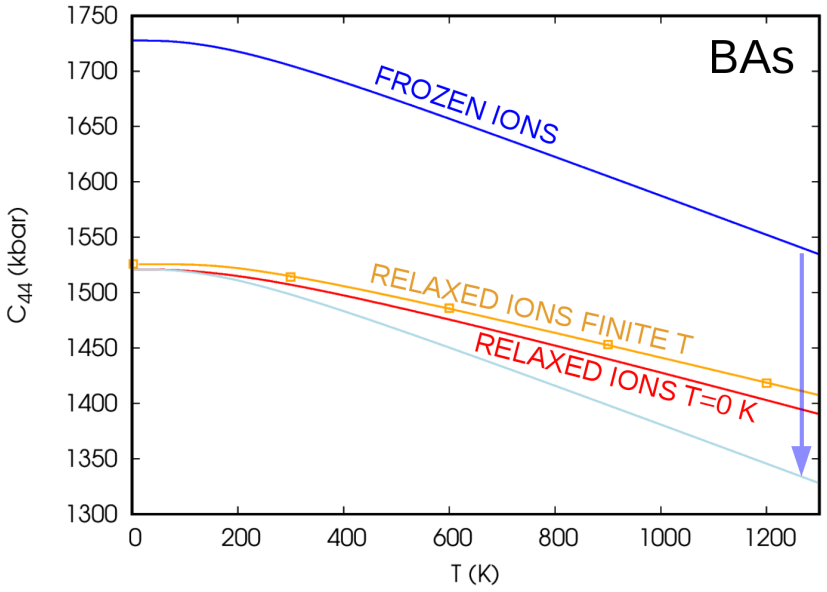

FIGURE 4.2: Temperature-dependent C_{44} elastic constant of BAs within the QHA computed with frozen-ions (blue), relaxed-ions at $T = 0$ K (red) and relaxed-ions at finite T (yellow). The frozen-ions result is translated below (light-blue curve) to compare the temperature dependence with the relaxed-ions results.

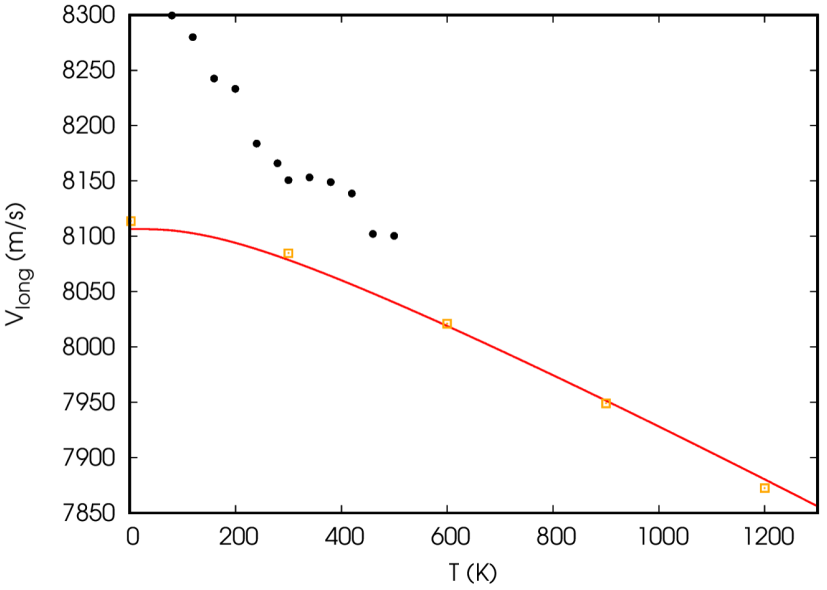

FIGURE 4.3: Longitudinal sound velocity in the 111 direction of BAs computed from TDECs (Eq. 3.1) with relaxed-ions at $T = 0$ K (red line) and at finite T (orange points). The experimental data is also reported (black points, extrapolated from Ref. [97]).

With the new C_{44} EC of BAs we can compute the longitudinal sound velocity of Eq. 3.1, compare with the previous calculation, and compare with experiment. In Fig. 4.3 we report the data of Fig. 3.1 with the new velocity (orange points). The differences are very small for the range of temperature considered.

From the difference between the frozen-ions ECs curves (blue) and the finite-temperature relaxed-ions ones (yellow) we get the correction $\Delta C_{44}(T)$ at the minimum of the free-energy. Then by comparing Eq. 4.21 with the one written in terms of ξ of Ref. [70] we can write ξ in terms of $\Delta C_{44}(T)$ and and hence get the $\xi(T)$ as:

$$\xi(T) = \frac{2}{\omega_{TO}(T)} \sqrt{\frac{a(T)\Delta C_{44}(T)}{\mu}} \tag{4.23}$$

where ω_{TO} is obtained by the interpolation of frequencies at the $\Omega(T)$ and $a(T) = [4\,\Omega(T)]^{\frac{1}{3}}$. The temperature-dependent Kleinman parameters are reported in Fig. 4.4. It decreases as temperature increases. Hence, in Si the difference with the experiment $\xi = 0.74(4)$ [70] increases as temperature increases as well.

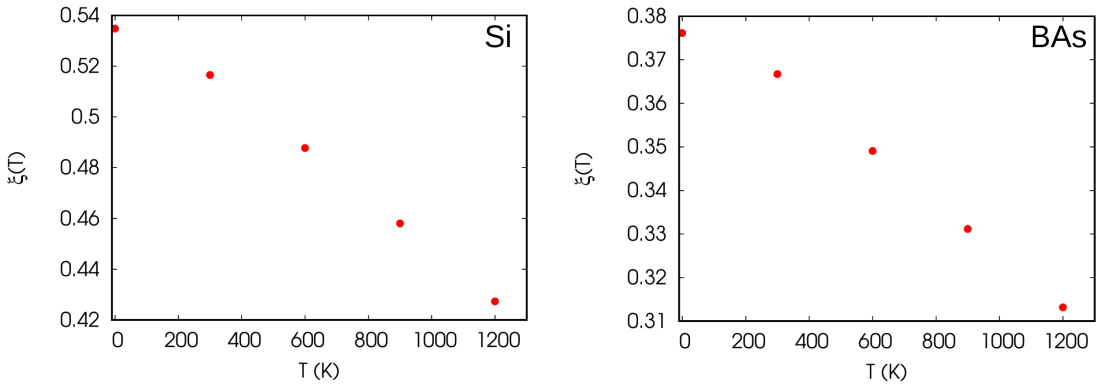

FIGURE 4.4: Temperature-dependent Kleinman parameter for Si (left) and BAs (right).

Chapter 5

Temperature-dependent atomic B-factor

In this chapter we pass to investigate another thermodynamic property of general interest: the atomic B-factor (BF). The BFs are defined in terms of the B-matrix whose elements $B_{\alpha\beta}$ are mean square atomic displacements in different directions. They account for the effects of temperature and quantum fluctuations on the lattice dynamics and define the Debye-Waller factor (DWF) which explains the temperature dependence of the intensities of X-ray or neutron diffraction peaks.

5.1 Introduction

The DWF accounts for the effect of lattice vibrations on Bragg-peak intensities of X-ray diffraction patterns of crystals and is responsible for their temperature dependence [112] and is a key ingredient for the simulation of Transmission Electron Microscopy (TEM) images [113]. The DWFs can be expressed in terms of the BF,

a quantity proportional to the mean-square atomic displacements that account for both temperature and zero point quantum effects. Experimentally, the BFs are known for many elemental crystals and compounds. They can be measured directly, for instance from X-ray single crystal or powder diffraction methods, or derived from the experimental phonon density states. Gao and Peng [114] presented the temperature dependence of BFs for 68 elemental crystals and 17 compounds with the zincblende structure. For 46 elemental crystals the BFs are derived from the measured phonon density of states, while for the others they are estimated within the Debye model.

BFs can be calculated from the phonon frequencies and the dynamical matrix eigenvectors of a solid, therefore *ab-initio* methods can be applied to calculate them as well. Lee and Gonze [115] calculated the BFs of SiO_2 α-quartz and stishovite with DFPT. Rignanese *et al.* [78] calculated the BF of Si as a function of temperature, showing that in this material the BF is determined mostly by the acoustic branches. Schowalter *et al.* computed the BFs for some group IV, III-V, and II-VI semiconductors with the zincblende [113] or the wurtzite structure [116] with the all-electron frozen phonon scheme and with the DFPT pseudopotential method. They also derived a fitting function for the temperature dependence of the BFs, and recently addressed more complex semiconductors containing B, Bi, or Tl [117]. Considerable theoretical efforts have been made in the field of molecular crystals where the BFs have been computed by DFT-based methods; we mention for instance Madsen *et al.* [118] that studied crystalline urea, crystalline benzene, urotropine, and L-alanine and George *et al.* [119] that focused on pentachloropyridine (C_5NCl_5). Recently, the BFs of nonperiodic structures have been derived from molecular dynamics simulations [120] devising an appropriate potential for the alloy AlGaN.

There are also materials, in particular anisotropic ones (i.e. h.c.p. metals), where

the experimental information are less complete. In these solids, the anisotropic BFs are obtained from the X-Ray diffraction intesities and in some cases only the room-temperature data is available. For instance Krishna *et al.* [121] and Narayana *et al.* [122] presented room-temperature mean square atomic displacements for some h.c.p. elements derived from powder-diffraction experiments, while Watanabe *et al.* [123] used single-crystal diffraction method to compute BFs for Cd, Mg, and Mg_3Cd at four different temperatures. Theoretical calculations on these systems are more rare although some rationalizations have been tried. For instance, in hcp metals a correlation has been found between the c/a ratio of the crystal parameters and the BF anisotropy [123].

Rather limited is also the knowledge of the effect of the exchange and correlation functionals on the BFs, although some tests have been presented [113]: the LDA describes the BFs of III-V and IV-IV semiconductors better than the GGA while the opposite has been found in II-VI semiconductors.

In this chapter, we investigate the BF of Si and study its dependence on the exchange and correlation functional. Moreover, we address the h.c.p. metals Ru, Mg, and Cd. Ab-initio lattice dynamics correctly predicts that Ru and Mg have a much smaller anisotropy than Cd and consistently improves upon the Debye model when comparison with experiments is possible. However the agreement is still not complete and the details depend on the exchange and correlation functional. Finally, we compare the BF calculated at the theoretical equilibrium geometry at zero temperature with the BF calculated accounting, within the QHA, for thermal expansion. We find that the effect is rather small in Si that has low thermal expansion, starts to be noticeable in Ru, and becomes more significant above room temperature in Mg whose thermal expansion is $5-6$ times larger than for Si.

5.2 Some definitions

The DWF is defined by:

$$e^{-2W(s)} = \exp\left(-\sum_{\alpha\beta} B_{\alpha\beta}(s) G_\alpha G_\beta\right), \tag{5.1}$$

where the label s identifies the atom in the unit cell, G_α and G_β are Cartesian components of the scattering wave vector (a reciprocal lattice vector of the solid) and $B_{\alpha\beta}(s)$ is the mean-square displacement matrix of the atom s:

$$B_{\alpha\beta}(s) = \frac{\hbar}{2NM_s} \sum_{\mathbf{q}\nu} \coth\left[\frac{\hbar\,\omega_\nu(\mathbf{q})}{2k_BT}\right] \frac{u^\nu_{s\alpha}(\mathbf{q}) u^\nu_{s\beta}(\mathbf{q})^*}{\omega_\nu(\mathbf{q})}, \tag{5.2}$$

where M_s is the mass of s-th atom, N is the number of cells in the crystal, $\omega_\nu(\mathbf{q})$ is the angular frequency, and $u^\nu_{s\alpha}(\mathbf{q})$ is the $s\alpha$-th component of the dynamical matrix eigenvector of the mode ν with wave-vector $\mathbf{q}$. k_B is the Boltzmann constant, $\hbar$ is the Planck constant divided by 2π, and T is the temperature. Eq. 5.2 can be rewritten in terms of the generalized density of states $g_{\alpha\beta}(s,\omega)$:

$$g_{\alpha\beta}(s,\omega) = \frac{1}{N} \sum_{\mathbf{q}\nu} u^\nu_{s\alpha}(\mathbf{q}) u^\nu_{s\beta}(\mathbf{q})^* \delta\left(\omega - \omega_\nu(\mathbf{q})\right), \tag{5.3}$$

which is normalized so that $\int_0^\infty g_{\alpha\beta}(s,\omega) d\omega = \delta_{\alpha\beta}$, as:

$$B_{\alpha\beta}(s) = \frac{\hbar}{2M_s} \int_0^\infty \coth\left[\frac{\hbar\,\omega}{2k_BT}\right] \frac{g_{\alpha\beta}(s,\omega)}{\omega} d\omega. \tag{5.4}$$

Eqs. 5.2 and 5.4 have been implemented in the `thermo_pw` software. In particular, in the case of Eq. 5.2, the code computes the quantity $\tilde{B}_{\alpha\beta}(s)$ restricting the sum over $\mathbf{q}$ to the irreducible Brillouin zone and introducing normalized weights $w_\mathbf{q}$ proportional to the number of points in the star of $\mathbf{q}$. $B_{\alpha\beta}(s)$ is obtained from $\tilde{B}_{\alpha\beta}(s)$ using the

following formula:

$$B_{\alpha\beta}(s) = \frac{1}{N_S} \sum_S \sum_{\gamma\delta} S^{-1}_{\alpha\gamma} S^{-1}_{\beta\delta} \tilde{B}_{\alpha\beta}(\bar{s}), \tag{5.5}$$

where N_S is the total number of symmetries of the point group of the solid, S are the rotation matrices and $\bar{s}$ is the index of the atom in which the rotation S transforms the atom s. The generalized density of states (Eq. 5.3) is computed and symmetrized at each ω with a similar formula so that $B_{\alpha\beta}(s)$ computed from Eq. 5.4 does not require any further symmetrization. Moreover, by applying Eq. 5.5 the symmetry restrictions on the BF matrices [124] are obtained automatically.

In the crystallographic literature, for cubic solids, it is common to use the Bragg condition to write the modulus of the scattering wave vector $|G|^2 = 16\pi^2 \sin^2\theta/\lambda^2$ in terms of the scattering angle θ and the X-ray wavelength λ. Therefore, the DWF becomes

$$e^{-2W(s)} = \exp\left(-\frac{2\bar{B}(s)\sin^2\theta}{\lambda^2}\right), \tag{5.6}$$

where $\bar{B}(s) = 8\pi^2 B_{xx}(s)$. We follow the same convention also for anisotropic solids plotting $\bar{B}_{\alpha\beta}(s) = 8\pi^2 B_{\alpha\beta}(s)$ and calling them BFs.

5.3 Computational parameters

The phonon calculations are made using DFPT as implemented in the Quantum Espresso package [32, 33]. The exchange and correlation functional is approximated by the LDA [48], the PBE [49] or the PBEsol functional [50]. We used PPs from `pslibrary` [24]. For Si we employed the PAW [52] PPs `Si.dft-nl-kjpaw_psl.1.0.0.UPF`, with `dft` equal to `pz`, `pbe`, and `pbesol`. The kinetic energy cut-off was set to 50 Ry for the wavefunctions and to 300 Ry for the charge density (for all three PPs). The

integrations over the Brillouin zone (BZ) were performed using a 8×8×8 Monkhorst-Pack **k**-point mesh. DFPT [14, 54] was used to calculate the dynamical matrix on a 8×8×8 **q**-points mesh. These dynamical matrices have been Fourier interpolated on a 300×300×300 **q**-points mesh to evaluate the BFs. For Ru we employed the ultrasoft (US) [125] PPs, `Ru.dft-spn-rrkjus_psl.1.0.0.UPF`. With all PPs, kinetic energy cut-offs were 70 Ry and 280 Ry for the wavefunctions and the charge density, respectively. The presence of a Fermi surface has been dealt with the smearing approach [51] with $\sigma = 0.02$ Ry and a mesh of $24 \times 24 \times 16$ **k**-points. For Mg we used the US PPs `Mg.dft-spn-rrkjus_psl.1.0.0.UPF`. Kinetic energy cut-offs for the wavefunctions and the charge density were 110 Ry and 440 Ry, respectively. The smearing parameter was $\sigma = 0.02$ Ry and the **k**-points mesh was $20 \times 20 \times 14$. For QHA calculations we used a mesh $32 \times 32 \times 24$. For Cd we used the US PPs `Cd.dft-n-rrkjus_psl.1.0.0.UPF`. Kinetic energy cut-offs of 70 Ry and 380 Ry for LDA PP, and 60 Ry and 1080 Ry for PBE and PBEsol PPs were used for the wavefunctions and the charge density, respectively. The smearing parameter was $\sigma = 0.02$ Ry and the **k**-points mesh was $18 \times 18 \times 12$. In the three metals, the DFPT phonon calculation used a **q**-point mesh $6 \times 6 \times 4$. The dynamical matrices on these points have been interpolated in a $300 \times 300 \times 190$ **q**-point mesh to calculate the BFs.

5.4 Results

5.4.1 Silicon

We start by presenting in Fig. 5.1 the LDA BF of Si at the equilibrium lattice constant 5.402 Å (expt. 5.431 Å). The BF matrices of the two Si atoms in the

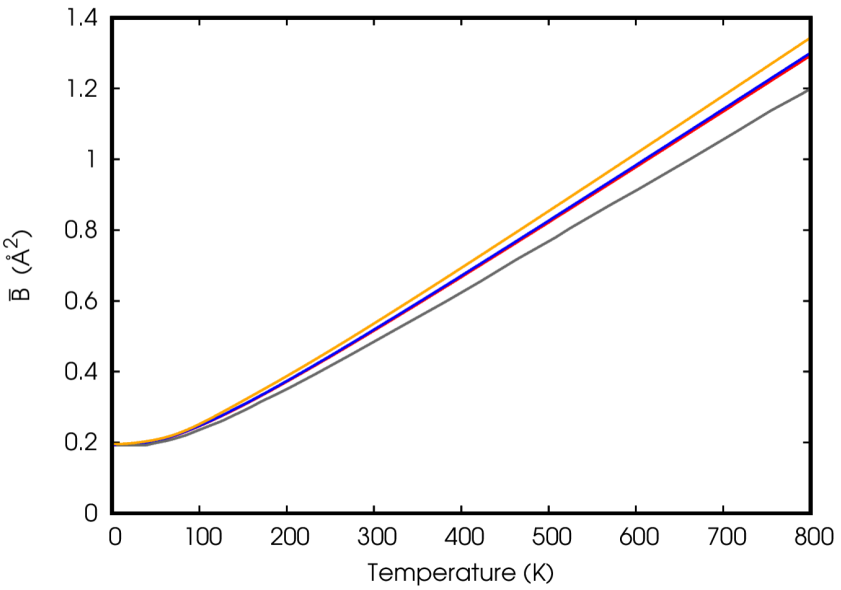

FIGURE 5.1: The LDA BF of Si computed using Eq. 5.2 (red) and Eq. 5.4 (blue). The theoretical data reported in Rignanese *et al.* [78] (gray) and in Schowalter *et al.* [113] (yellow) are shown for comparison.

unit cell are diagonal, $\bar{B}_{\alpha\beta} = \bar{B}\delta_{\alpha\beta}$, and equal. $\bar{B}_{xx}(1)$ obtained by Eq. 5.2 and Eq. 5.4 are both shown, but on the scale of the figure the two curves are almost indistinguishable. Since this holds also for the other materials studied here, in the following discussion we show only the BFs obtained by Eq. 5.4. In the same plot, we report the LDA BF from Ref. [78] using a norm conserving PP at the equilibrium lattice constant 10.18 a.u. $\approx$ 5.39 Å and the parameterization of Schowalter *et al.* [113]. The former finds a BF smaller than ours, while the latter finds slightly larger values.

In Fig. 5.2 we compare the BF obtained by the three exchange and correlation functionals (LDA, PBE, and PBEsol). Each BF is calculated at the equilibrium lattice constant (5.470 Å for PBE and 5.434 Å for PBEsol). In agreement with previous works [129] LDA slightly underestimates the lattice constant while PBE overestimates it. PBEsol is in between the two, still slightly larger than experiment. BFs are larger for PBEsol and smaller for PBE while LDA is in between. This

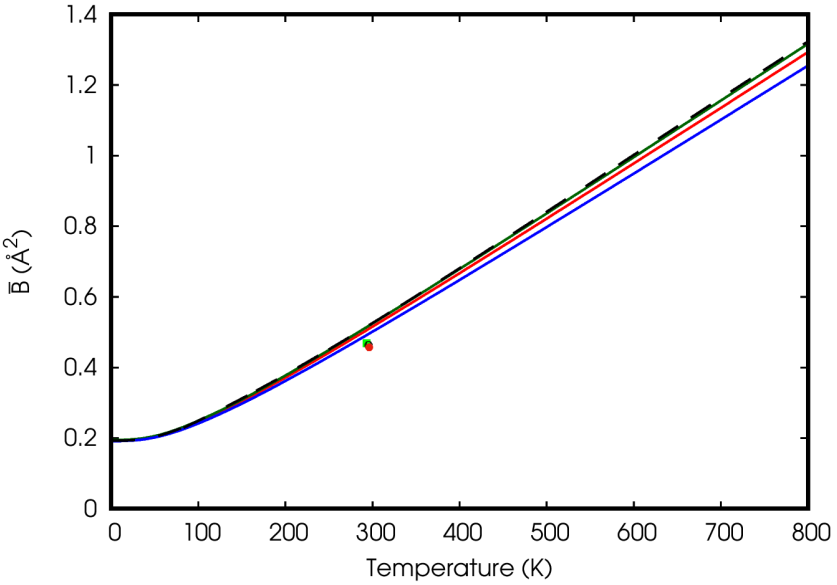

FIGURE 5.2: The BF of Si for different exchange and correlation functionals (LDA red, PBE blue, and PBEsol green) compared with the BF derived from the experimental phonon density of states [114] (dashed line) and three points at room temperatures discussed in the literature: green square [126], black circle [127] and red circle [128] (note that errorbars are smaller than the size of the points).

trend can be understood by analyzing the phonon dispersion curves (reported in Fig. 5.3) and noticing, as in Ref. [78], that in Si the main contribution to the BF comes from the acoustic modes. This is illustrated in Fig. 5.4 where we show the contributions of the different modes to the BF. The largest ones are those of the two lower acoustic modes (1 and 2), while the third acoustic mode (3) and the optical modes give smaller contributions. PBEsol has the lowest frequency of the acoustic modes 1 and 2 and hence the largest BF. In Fig. 5.2 some experimental data are also reported. The parameterization of Gao and Peng [114] is in excellent agreement with the PBEsol BF. Room-temperature experimental BFs derived from Pendellösung method [128] and high resolution charge-density studies [127] are also reported for comparison. Moreover, we note that several lattice-dynamical models have been used to compute the BF of Si: the different studies produce a quite large spread of BF values [131]. In this analysis we quote the data reported in a more

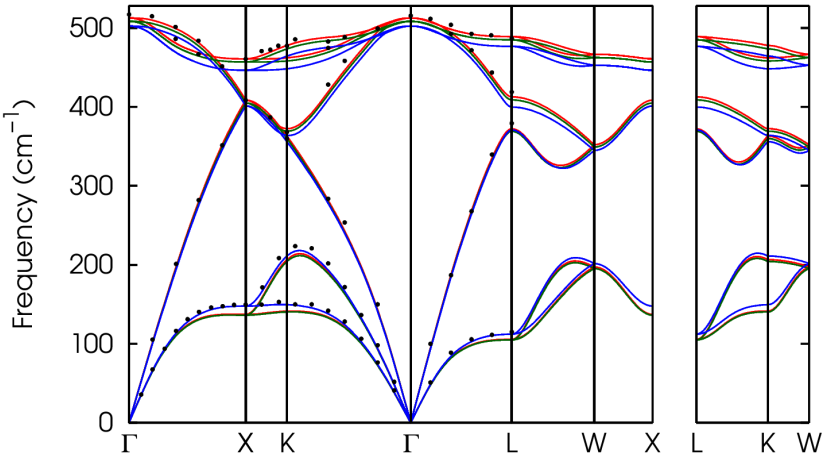

FIGURE 5.3: Si phonon dispersions calculated with different exchange and correlation functionals (LDA red, PBE blue, and PBEsol green) compared with experimetal inelastic neutron scattering data [130] (points) measured at $T = 296$ K.

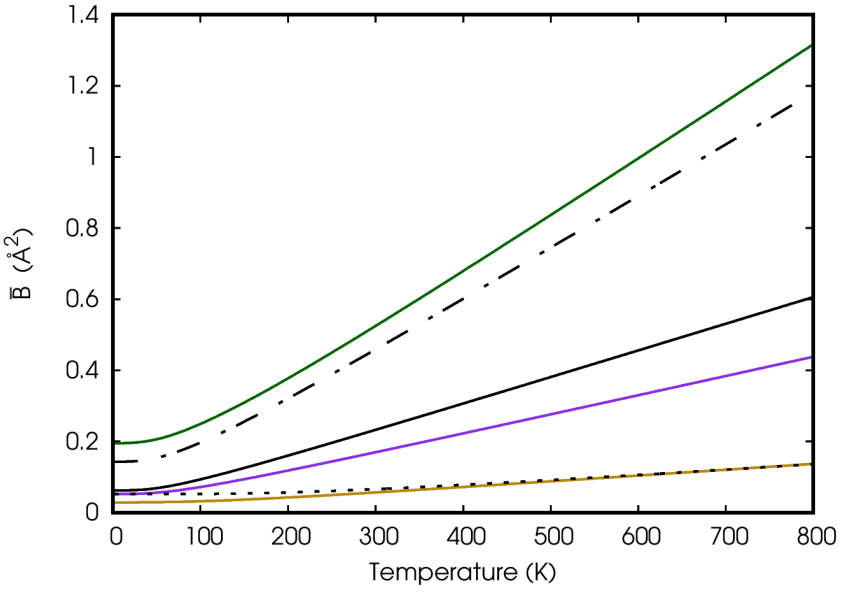

FIGURE 5.4: Contribution of the different modes to the BF of Si: mode 1 (black), mode 2 (violet) and mode 3 (yellow). The modes are ordered according to the frequency, from the lowest to the highest. We show also the contribution of all acoustic modes (1, 2, and 3) (dash-dotted line) and of all optical modes (dotted line).

TABLE 5.1: Theoretical lattice parameters of the h.c.p. metals at T=0 K compared with the experimental data [132].

	Ruthenium		Magnesium		Cadmium	
	a (Å)	c/a	a (Å)	c/a	a (Å)	c/a
LDA	2.678	1.578	3.139	1.622	2.915	1.867
PBESOL	2.693	1.578	3.180	1.623	2.961	1.865
PBE	2.723	1.577	3.199	1.624	3.026	1.906
Expt.	2.704	1.584	3.209	1.624	2.979	1.886

recent work based on Born-von Kármán force constants model [126]. The three experimental points are in good agreement but slightly smaller than theoretical curves and Gao and Peng parameterization.

5.4.2 h.c.p. metals

In this section, we present the harmonic BFs of h.c.p. metals Ru, Mg, and Cd, at the equilibrium crystal parameters reported in Tab. 5.1. In these systems, the BFs matrices of the two atoms in the unit cell are diagonal and equal. Two diagonal elements coincide $\bar{B}_{xx} = \bar{B}_{yy}$, while $\bar{B}_{zz}$ might differ.

In Fig. 5.5 we report $\bar{B}_{xx}$ and $\bar{B}_{zz}$ for the three functionals. For each functional, $\bar{B}_{zz}$ is larger than $\bar{B}_{xx}$ and the anisotropy is increasing with temperature. PBE gives the largest BFs, followed by PBEsol and LDA, in agreement with the trend of the phonon frequencies shown in reference [35]. Experimetal points at (295 ± 3) K are also reported [122]. The theoretical curves slightly overestimate the experimental data. A second experimental point for Ru has been reported by Krishna and Sirdeshmukh [121][1] at the same temperature and refers to the average BF $\langle \bar{B} \rangle = (2\bar{B}_{xx} + \bar{B}_{zz})/3$. In Fig. 5.6 we compare $\langle \bar{B} \rangle$ (for the three functionals) with this experimental point and with the point obtained by averaging the data of

[1]This number is not corrected for thermal diffusive scattering [133] while all the others experimental diffraction data reported in this chapter are corrected for this effect.

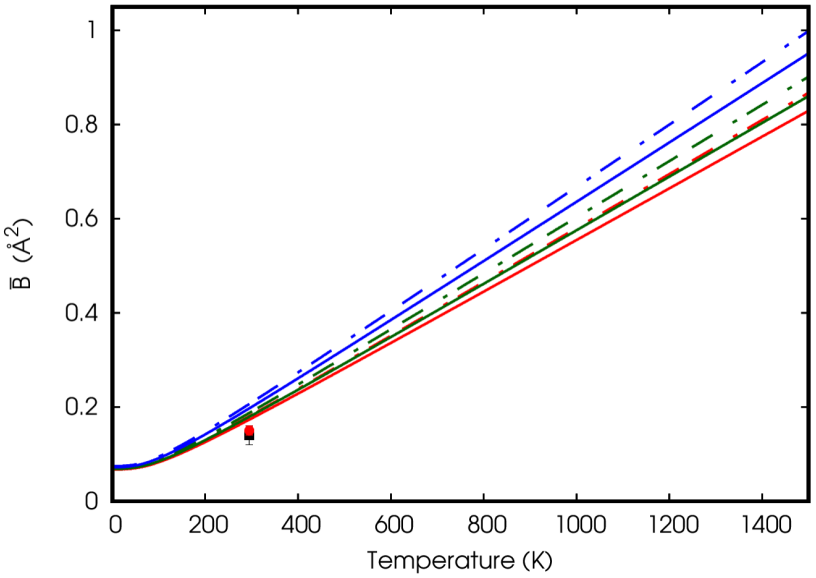

FIGURE 5.5: BFs of Ru: ($\bar{B}_{xx}$ continuous line, and $\bar{B}_{zz}$ dash-dotted line) for different exchange and correlation functionals (LDA red, PBE blue, and PBEsol green). The points are experimental data of Narayana *et al.* [122].

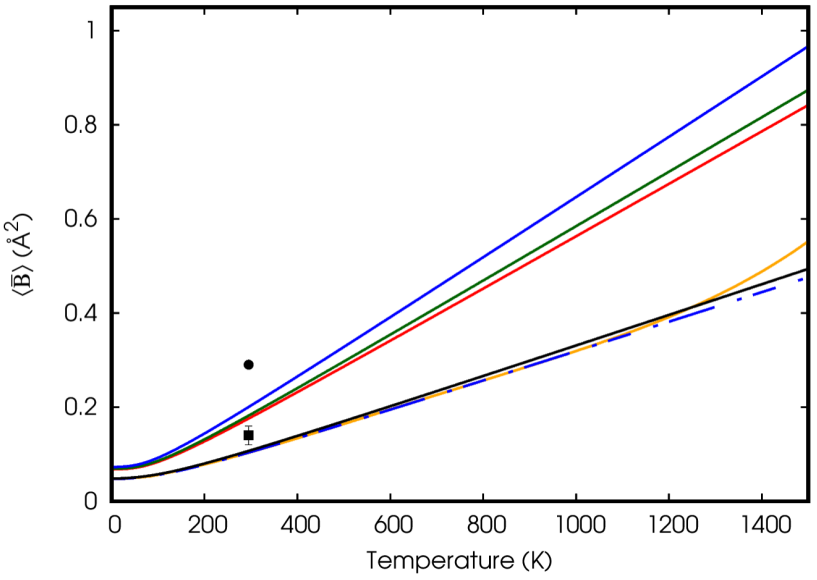

FIGURE 5.6: $\langle \bar{B} \rangle = (2\bar{B}_{xx} + \bar{B}_{zz})/3$ of Ru. The $\langle \bar{B} \rangle$ derived from the LDA (red), PBEsol (green), and PBE (blue) phonon dispersions are compared with the results of a Debye model with Debye temperature $\theta_D = 589$ K, derived from the LDA elastic constants (black), or $\theta_D = 600$ K (blue dash-dotted line). The parameterization [114] of the Debye model result with $\theta_D = 600$ K (orange) is also shown. The points are the experimental data of Krishna and Sirdeshmukh [121] (circle) and Narayana *et al.* [122] (square).

[122]. The theoretical predictions are between the two points slightly closer to the second. In Fig. 5.6 we show also the temperature dependent parameterization of $\langle \bar{B} \rangle$ proposed by Gao and Peng [114]. Such parameterization has been obtained by a fit of the Debye-model BFs calculated with the Debye temperature $\theta_D = 600$ K [134]. This curve is lower than our estimate and of both the experimental points. Within the Debye approximation the phonon density of states is written as $g_D(\omega) = 9N_{at}\omega^2/\omega_D^3$, where N_{at} is the number of atoms in the unit cell and ω_D is the Debye angular frequency related to the Debye temperature by $k_B\theta_D = \hbar\omega_D$. Using this density of states one can evaluate $\langle \bar{B} \rangle$ for systems with one atomic type of mass M, as:

$$\langle \bar{B} \rangle = \frac{12\pi^2\hbar^4}{k_B^3\theta_D^3 M} \int_0^{\omega_D} \omega \coth\left(\frac{\hbar\omega}{2k_BT}\right) d\omega. \tag{5.7}$$

We used this formula to obtain the curves reported in Fig. 5.6. We show the results for $\theta_D = 589$ K, the value obtained by averaging the sound velocities derived from the LDA elastic constants and for $\theta_D = 600$ K, the experimental value. We can see that the fit of Gao and Peng [114] reproduces the Debye model BF quite well until ~ 1300 K, but the Debye model BFs are smaller than the ab-initio lattice dynamics estimates.

In Fig. 5.7 we report $\bar{B}_{xx}$ and $\bar{B}_{zz}$ of Mg calculated with the three functionals. The theoretical PBE and PBEsol results are almost isotropic. LDA predicts a small anisotropy with $\bar{B}_{xx}$ larger than $\bar{B}_{zz}$, opposite to what was found in Ru and opposite to the experimental anisotropy reported in the figure [123]. Actually experimental data for $\bar{B}_{xx}$ are quite close to the PBE theoretical values but the theoretical underestimation of the anisotropy leads to too small values of $\bar{B}_{zz}$. In Fig. 5.8 we compare our results for $\langle \bar{B} \rangle$ with the parameterization of Gao and Peng [114] obtained from the experimental phonon density of states. Our results are lower than these data

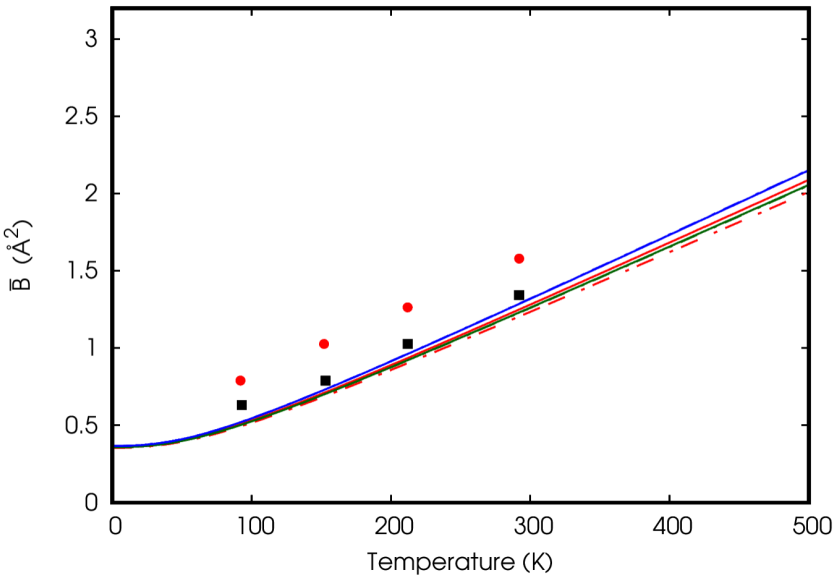

FIGURE 5.7: BF of Mg: ($\bar{B}_{xx}$ continuous line, and $\bar{B}_{zz}$ dashed line) for different exchange and correlation functionals (LDA red, PBE blue, and PBEsol green). The points are experimental data [123] (squares $\bar{B}_{xx}$, circles $\bar{B}_{zz}$).

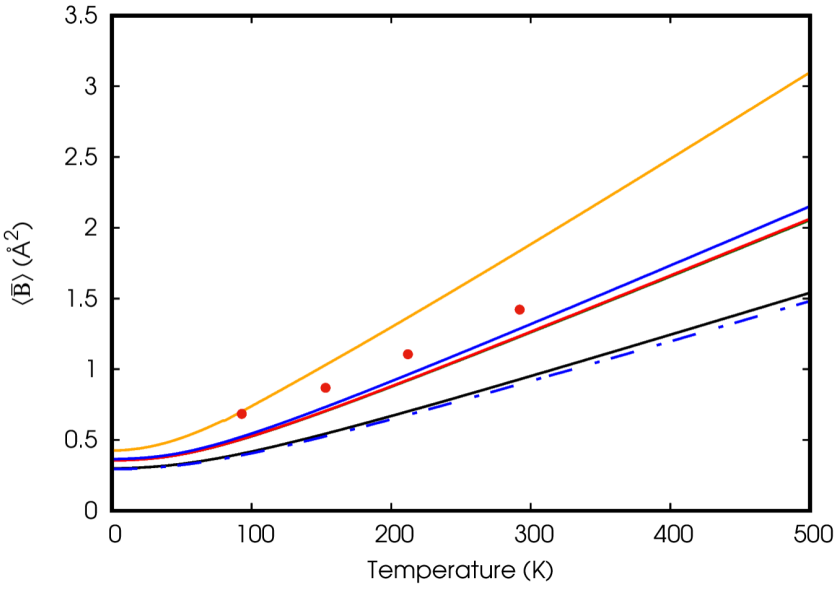

FIGURE 5.8: $\langle \bar{B} \rangle = (2\bar{B}_{xx} + \bar{B}_{zz})/3$ of Mg. The $\langle \bar{B} \rangle$ derived from the LDA (red), PBEsol (green), and PBE (blue) phonon dispersions are compared with the results of a Debye model with Debye temperature $\theta_D = 395$ K derived from the LDA elastic constants (black), or the experimental Debye temperature $\theta_D = 403$ K (blue dashed line). The parameterization [114] of the BF derived from the experimental phonon density of states (orange) is also shown. The points are derived from the experimental data [123].

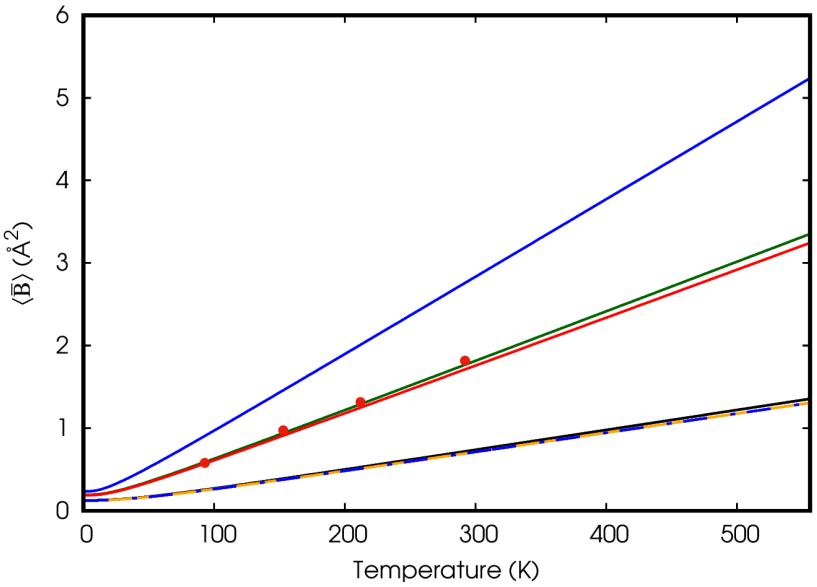

FIGURE 5.9: $\langle \bar{B} \rangle = (2\bar{B}_{xx} + \bar{B}_{zz})/3$ of Cd. The $\langle \bar{B} \rangle$ derived from the LDA (red), PBEsol (green), and PBE (blue) phonon dispersions are compared with the results of a Debye model with Debye temperature $\theta_D = 205$ K derived from the LDA elastic constants (black), or the experimental Debye temperature $\theta_D = 209$ K (blue dashed line). The parameterization [114] of the BF derived the Debye model with $\theta_D = 209K$ (orange) is also shown. The red points are derived from the experimental data [123].

and the discrepancy increases with temperature. The points deduced from the experimental data of Watanabe *et al.* [123] are instead closer to our theoretical values and have a similar temperature dependence. In the same figure we also report $\langle \bar{B} \rangle$ calculated from a Debye model with $\theta_D = 395$ K the value derived from the LDA elastic constants which is quite close to the experimental one $\theta_D = 403$ K. Also for Mg the $\langle \bar{B} \rangle$ derived from the Debye model is smaller than the one derived from the ab-initio lattice dynamics and hence even more distant from experiment.

In Fig. 5.9 we report $\bar{B}_{xx}$ and $\bar{B}_{zz}$ of Cd calculated with the three functionals. All three functionals predict a quite large BF anisotropy with LDA and PBEsol giving similar results. PBE predicts a larger anisotropy so that although $\bar{B}_{xx}$ is similar to the other functionals, $\bar{B}_{zz}$ is higher. Experimental values of the BF [123] are reported in the figure. The LDA and PBEsol BFs reproduce better experiments than

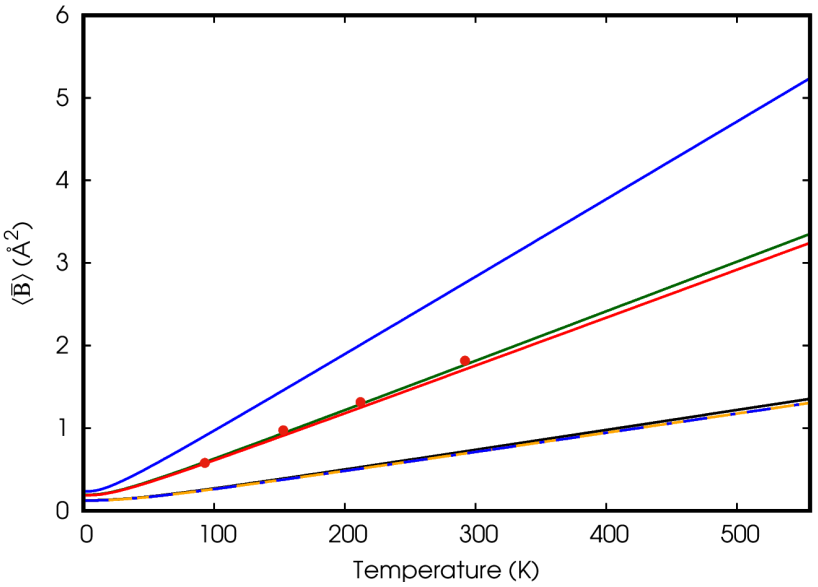

FIGURE 5.10: $\langle \bar{B} \rangle = (2\bar{B}_{xx} + \bar{B}_{zz})/3$ of Cd. The $\langle \bar{B} \rangle$ derived from the LDA (red), PBEsol (green), and PBE (blue) phonon dispersions are compared with the results of a Debye model with Debye temperature $\theta_D = 205$ K derived from the LDA elastic constants (black), or the experimental Debye temperature $\theta_D = 209$ K (blue dashed line). The parameterization [114] of the BF derived the Debye model with $\theta_D = 209K$ (orange) is also shown. The red points are derived from the experimental data [123].

the PBE (especially for the $\bar{B}_{zz}$). In Fig. 5.11 we show the temperature dependence of $\langle \bar{B} \rangle$ computed from our phonon dispersion curves and compared with a Debye model BF calculated at $\theta_D = 205$ K deduced from the LDA elastic constants and at $\theta_D = 209$ K, the experimental value. Gao and Peng's parameterization (also shown in the figure) is made on the Debye-model BF and coincides in all the temperature range. Also for Cd the Debye model BF is lower than the ab-initio one.

Watanabe *et al.* [123] showed that there is a correlation between the anisotropy of the BFs ($\bar{B}_{zz}/\bar{B}_{xx}$) and the c/a parameter of the h.c.p. structure. We compare in Fig. 5.11 our estimates of BF anisotropies at 292 K with the reported experimental values. On the large scale of this figure differences between different functionals are small and there is a reasonable agreement between theory and experiment.

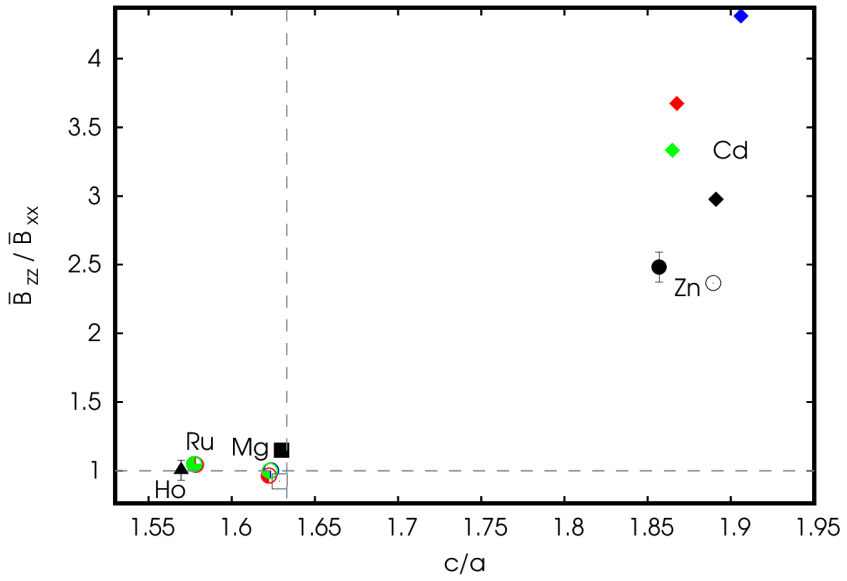

FIGURE 5.11: B_{zz}/B_{xx} as a function of c/a for the hcp metals. Black points are data reported by Watanabe *et al.* (full and empty points have different references). Red, blue, and green points indicate our LDA, PBE, and PBEsol theoretical estimates within the harmonic approximation at $T = 292$ K. The vertical dashed line indicates the ideal ratio $c/a = 1.633$.

5.5 Quasi-harmonic B-factor

Eqs. 5.2 and 5.4 depend explicitly on temperature while the phonon frequencies and the atomic displacements are assumed to be temperature independent. However the results depend on the geometry chosen to compute the phonon dispersions. The BFs shown so far have been computed within the HA, *i.e.* at the $T = 0$ K equilibrium structure neglecting both the zero point motion and thermal expansion. In this section we estimate the importance of this approximation on the final result. We compute within the QHA the temperature dependent crystal parameters and the thermal expansion as described in Chapter 2. Moreover, we compute the BFs at the same geometries used to evaluate the thermal expansion: 9 values for the lattice constant a for Si and a 5×5 grid of values for a and c/a for the h.c.p. metals. The grids are centered on the crystal parameters used in the previous section.

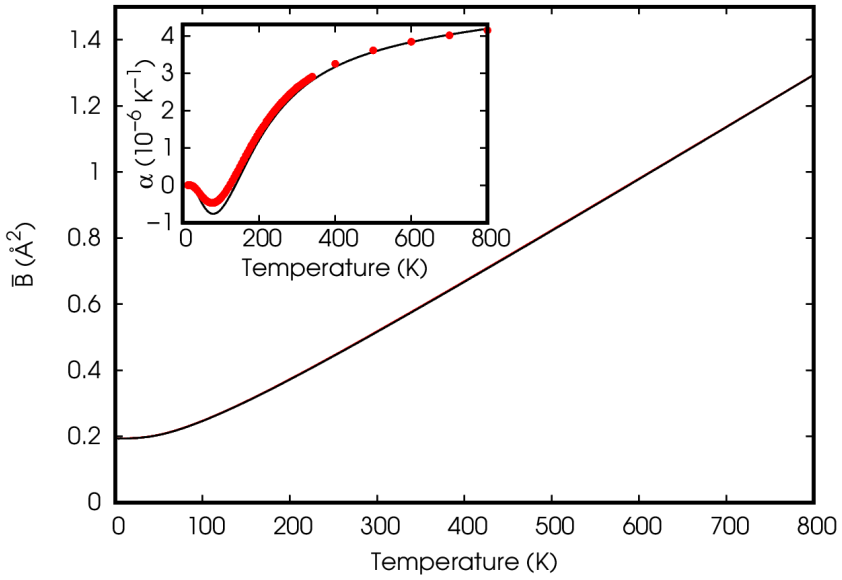

FIGURE 5.12: LDA BF of Si within the QHA (black) compared with the HA BF (red): the two results overlap. In the inset, the thermal expansion of silicon is compared with the experimental data (points) [76, 77].

The BFs computed in these geometries are interpolated by a quartic polynomial of the crystal parameters at each temperature. This polynomial is then used to calculate the BFs at the geometry that corresponds to that temperature.

In the following figures we compare the BFs computed within the HA with those computed as described above that we call QHA BFs. For simplicity we compare only the LDA results. In Fig. 5.12 the example of Si is reported. The thermal expansion of Si is also shown for reference and compared with the experiments [76, 77]. Since this thermal expansion is quite small the HA and the QHA BFs are indistinguishable on the scale of the figure.

In Fig. 5.13 we compare the HA and QHA BFs of Ru. Thermal expansion increases slightly the BFs and the effect becomes noticeable above room temperature. Moreover, within the QHA the increase of the anisotropy with temperature is larger than within the HA (reflecting also the behavior of thermal expansion tensor). Our theoretical LDA thermal expansion is smaller than experiment and therefore the effect

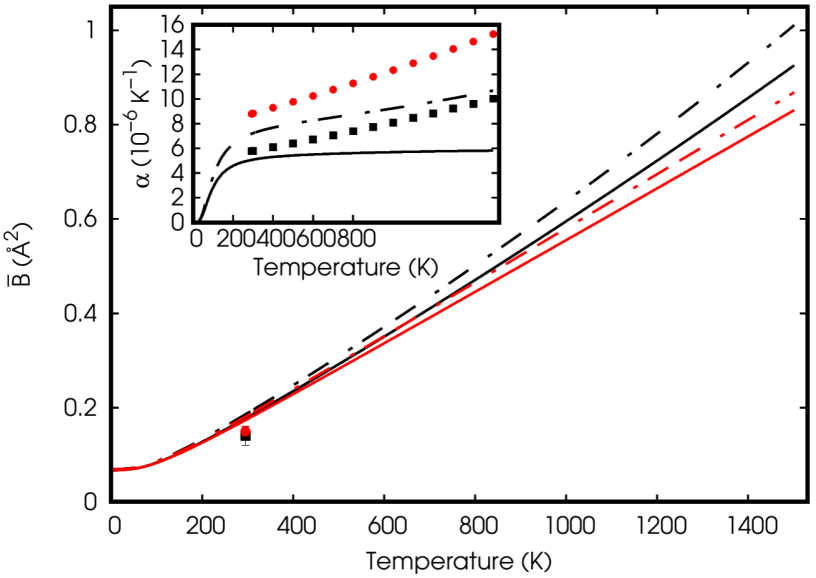

FIGURE 5.13: LDA BF of Ru within QHA (black) compared with the HA BF (red): the continuous lines represent $\bar{B}_{xx}$, while the dash-dotted lines indicate $\bar{B}_{zz}$. The points are experimental data of Narayana *et al.* 2001. On the inset, the theoretical LDA linear thermal expansion of Ru (α_{xx} continuous line, α_{zz} dash-dotted line) is compared with the experimental data [135] (α_{xx} black squares, α_{zz} red circles).

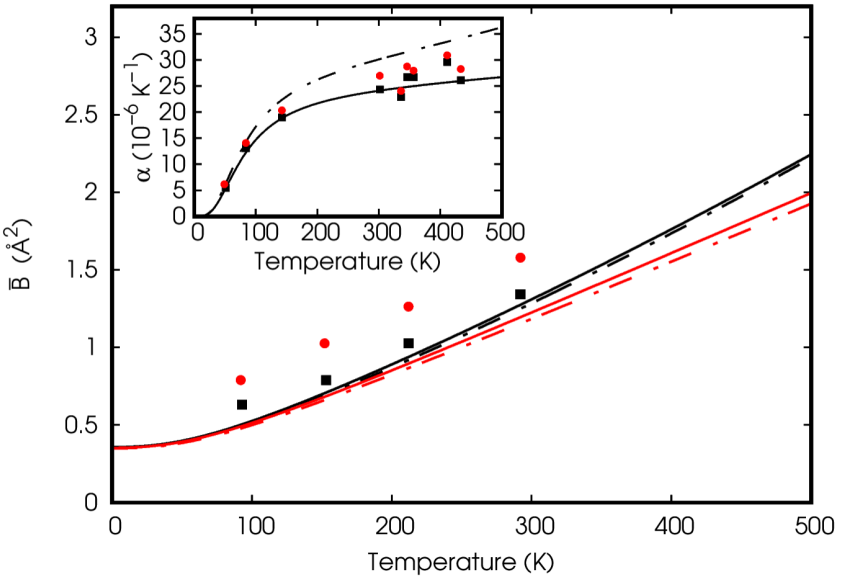

FIGURE 5.14: DA BF of Mg within the QHA (black) compared with the HA BF (red): the continuous lines represent $\bar{B}_{xx}$, while the dash-dotted lines indicate $\bar{B}_{zz}$. The comparison with experiment [123] is presented ($\bar{B}_{xx}$ black squares, $\bar{B}_{zz}$ red circles). In the inset, the theoretical linear thermal expansion of Mg (α_{xx} continuous line, α_{zz} dash-dotted line) is compared with the experimental points [136] (α_{xx} black squares, α_{zz} red circles).

of thermal expansion on the BF could be slightly underestimated.

Finally, in Fig. 5.14, we present the comparison between the HA and the QHA BFs of Mg. The difference between the two approximations is more significant in Mg then in Ru because of the larger thermal expansion of Mg (Fig. 5.14). Note also that our thermal expansion is more anisotropic than in experiment, suggesting that the thermal expansion effect alone is not sufficient to recover the experimental BF anisotropy.

In the previous paragraphs we presented our implementation of the BFs in the `thermo_pw` code which is also described in the paper of Ref. [4]. BF tensors can be computed for an arbitrary crystal using a Debye model or ab-initio within the HA and the QHA. Now, we use it to address the BF of BAs within the QHA, whose thermoelastic and several thermodynamic properties were investigated in Section 3.4.

Until now we have seen only examples of crystals with identical atoms in the unit cell providing the same BF for both. In BAs we have two different atoms and, hence,

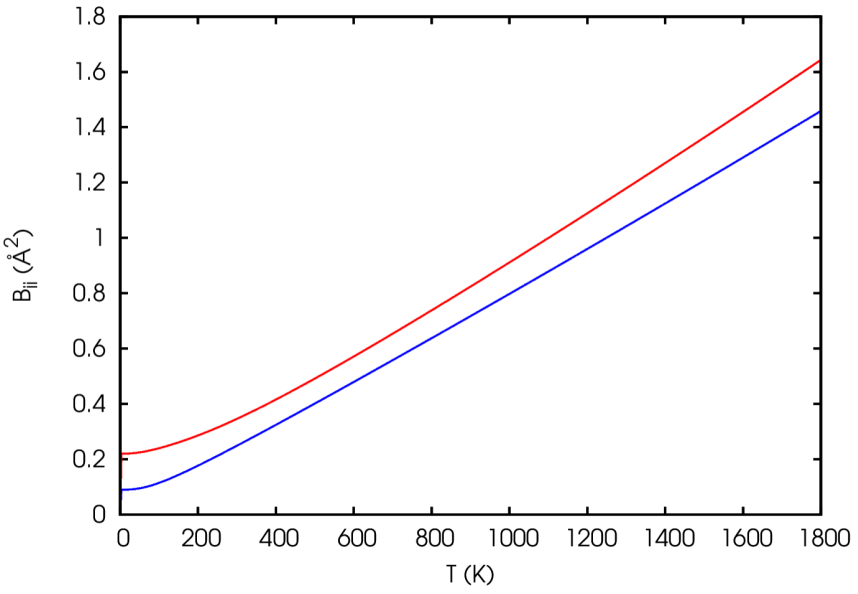

FIGURE 5.15: Temperature dependent atomic B-factor for the cubic BAs: B (red), As (blue).

two different BFs matrices that are diagonal with only one independent component (because BAs is cubic). In Fig. 5.15 we show the BF for B (red) and As (blue). The former is 0.35 $\mathring{A}^2$ at $T = 300$ K and grows up to 0.74 $\mathring{A}^2$ at $T = 800$ K. The latter is smaller because of the larger mass: 0.25 $\mathring{A}^2$ at $T = 300$ K and 0.64 $\mathring{A}^2$ at $T = 800$ K. They are smaller than the BFs of Si (Fig. 5.12) which has 0.52 $\mathring{A}^2$ at $T = 300$ K and 1.29 $\mathring{A}^2$ at $T = 800$ K.

Conclusions

In this thesis, we have worked on the thermodynamic properties of materials computed within the frameworks of DFT and DFPT.

In particular we focused on the calculation of the TDECs. We compared the QSA and the QHA approaches. The first method is less computationally demanding and takes into account only the TE effect. The second method, more accurate, obtains the ECs from the derivatives of the Helmholtz free-energy with respect to the strain and requires the calculation of the phonon dispersions in many strained geometries. The two methods were applied to compute the TDECs of three cubic crystals: Si, Al, and Ag. The ECs were systematically compared with experiment. It was found that the experimental temperature dependence agrees very well with QHA while QSA gives less accurate results. The actual values of the ECs depend on the exchange and correlation functional: with our choices the values are usually within 10% from experiment but for some elements and ECs the error can be even lower. As a further check we used the TDECs to estimate the TE using the formula based on mode Grüneisen parameters. The TDECs computed within the QHA allow to reproduce with remarkable accuracy the TE given by differentiation of the temperature dependent lattice constant.

We addressed the role of the exchange and correlation functionals in the simple metals Pd, Pt, Cu and Au: LDA and GGA give almost the same softenings but differ in the zero temperature values. This work shows that PBEsol is the best choice for Pd, Pt, and Au. PBE is the best for Cu. On the same metals we studied the effect of thermal electronic excitations. We found a negligible contribution on all the ECs of Cu and Au and on the ECs C_{11} and C_{12} of Pd and Pt. Instead they

lead to an improvement in the agreement with the experimental C_{44} of Pd and Pt. Even though the softenings computed for all ECs are in reasonable agreement with the experimental ones, we could not reproduce the precise behavior of the anomalies in Pd and Pt. In Pt, we further investigated the effects of the change of the phonon frequencies induced by the finite temperature thermal electronic excitations, finding that it is small, even at the highest studied temperature $T = 1000$ K. At the current stage the discrepancy between theory and experiment in Pd and Pt is not solved and might require a more sophisticated functional than LDA or GGA. Also a method that includes the anharmonic effects beyond the QHA could be useful although probably only at high temperatures. Since the experimental data are quite old, also a novel measurement of the TDECs could be useful. Moreover, in the previous section we investigated the ECs of Al and Ag without the electronic contribution which is, however, negligible as found for Cu and Au not presenting partially filled d bands.

We studied the thermodynamic properties of BAs, a semiconductor of technological interest that exhibits ultra-high thermal conductivity and is under investigation for thermal management in electronics. We found a good agreement with experimental data and previous calculations. We provided the first information about the temperature dependence of its ECs from which we have estimated the temperature variation of the longitudinal sound velocity along the [111] direction and compared with recent experiments.

In Si and BAs the atoms relax when the rhombohedral strain is applied to get the C_{44} EC. We estimate the effect of the atomic relaxation at finite temperature by means of the internal-strain method dealing with the derivatives of the Helmholtz free-energy with respect to both displacements and strain. We showed that there is a non-negligible effect in Si which produces a temperature variation of $C_{44} \sim 4\%$

smaller than the one obtained with the zero-temperature relaxation in the range of temperatures $0 - 1200$ K. This effect is smaller in BAs, with a difference of $\sim 1\%$ for the C_{44} variation in the same range of temperatures between the results obtained with finite-temperature and zero-temperature relaxations. The differences introduced by the finite-temperature relaxation increase with temperature.

The tools used to evaluate the TDECs within the QSA and QHA were implemented in the open source `thermo_pw` code for a generic crystal and carefully tested for the cubic materials presented in the work described above and in Refs. [1–3]. Despite the recent release of the papers, new works based on this program are already appearing in the literature. For example, a study of the TDECs of cubic ZrC and HfC has been presented in Ref. [137] by using the QSA and QHA for possible applications on hypersonic vehicles. The treatment of finite-temperature atomic relaxations is still at an experimental stage, presently limited to diamond and zincblende structures and not yet publicly available.

Finally, we focused on the calculation of the temperature dependent BF. It accounts for the effects of temperature and quantum fluctuations on the lattice dynamics and defines the Debye-Waller factor which, in turn, explains the temperature dependence of the intensities of X-ray or neutron diffraction peaks in crystallography. We compared the harmonic with the QHA. The quasi-harmonic corrections were studied in Si, Ru and Mg: they are important when the thermal expansion is large such as for Mg, less relevant for Si and Ru where the thermal expansion is small. We showed that in some cases also the choice of the exchange and correlation functional can give significant differences in the BFs. This calculation is implemented in the `thermo_pw` code as well. The BF tensors can be computed using a Debye model or within the ab-initio harmonic or quasi-harmonic approximations. This work was presented in Ref. [4].

Appendix A

Elastic constants in a solid with stress

In this appendix we discuss in more details the theory of elastic constants under stress, mainly following Ref. [138].

A.1 The strain

We consider a solid under a particular deformation which brings it from a reference-starting configuration to a new configuration. The reference configuration may or may not be an equilibrium configuration, for instance a pressure (or generic stress) might be present in the initial system. We indicate the generic point in the reference configuration with $\mathbf{X}$. The applied deformation acts as a function that brings the coordinates of the starting point $\mathbf{X}$ in the new point $\mathbf{x}(\mathbf{X})$ (indicated with lowercase $\mathbf{x}$). The displacement of the new point from its reference position is:

$$\mathbf{u}(\mathbf{X}) = \mathbf{x}(\mathbf{X}) - \mathbf{X}, \tag{A.1}$$

which we write in terms of the Cartesian components as:

$$u_\alpha(\mathbf{X}) = x_\alpha(\mathbf{X}) - X_\alpha. \tag{A.2}$$

Let us take its derivative with respect to the generic direction X_β:

$$u_{\alpha\beta}(\mathbf{X}) = \frac{\partial u_\alpha(\mathbf{X})}{\partial X_\beta} = \frac{\partial x_\alpha(\mathbf{X})}{\partial X_\beta} - \delta_{\alpha\beta}. \tag{A.3}$$

When $u_{\alpha\beta}$ is constant, namely, in the case of homogeneous strain[1] we can rearrange and integrate Eq. A.3 to obtain:

$$x_\alpha = \sum_\beta (\delta_{\alpha\beta} + u_{\alpha\beta}) X_\beta. \tag{A.4}$$

Hence, the homogeneous strain imply a linear transformation: straight lines in the reference configuration remain straight in the strained configuration.

The strain defined in Eq. A.3 is not symmetric and might include rotations. Nevertheless, it can be written as a sum of a symmetric part $\epsilon_{\alpha\beta}$ and an antisymmetric part $\omega_{\alpha\beta}$:

$$u_{\alpha\beta} = \epsilon_{\alpha\beta} + \omega_{\alpha\beta}, \tag{A.5}$$

$$\epsilon_{\alpha\beta} = \frac{1}{2}(u_{\alpha\beta} + u_{\beta\alpha}), \tag{A.6}$$

$$\omega_{\alpha\beta} = \frac{1}{2}(u_{\alpha\beta} - u_{\beta\alpha}), \tag{A.7}$$

[1] As an example of homogeneous strain, let us take an example of a bar under deformation along the x direction. Its left edge is at $x = 0$ and firstly the right one is at the position $x = l_0$ which is the bar length without deformation. Then a deformation is applied which brings the right edge in the new position $x = l$. The strain is the relative length variation $(l - l_0)/l$. Considering an homogeneous strain means that if we consider, for example, the middle point of in the unstrained bar $x = l_0/2$, after the deformation it will be in the point $x = l/2$.

the rotations are included in $\omega_{\alpha\beta}$.

A.1.1 Lagrangian strain

The strain can also be described from the change of the square of the distances from the origin of the strained position $\mathbf{x}$ and the original position $\mathbf{X}$:

$$\mathbf{x}^2 - \mathbf{X}^2 = 2\sum_{\alpha\beta}\eta_{\alpha\beta}X_\alpha X_\beta, \tag{A.8}$$

that defines the Lagrangian strains $\eta_{\alpha\beta}$. By using Eq. A.4 to compute $\mathbf{x}^2 = \sum_\gamma x_\gamma^2$ we get the Lagrangian strains $\eta_{\alpha\beta}$ in terms of $u_{\alpha\beta}$:

$$\eta_{\alpha\beta} = \frac{1}{2}\left(u_{\alpha\beta} + u_{\beta\alpha} + \sum_\gamma u_{\gamma\alpha}u_{\gamma\beta}\right). \tag{A.9}$$

The Lagrangian strains are always symmetric and to the first order equal to $\epsilon_{\alpha\beta}$ (for sufficiently small strains).

A.2 The energy expansion

A given thermodynamic potential E [2] can be Taylor expanded in terms of the strain to quantify the change of the energy due to the application of the strain itself. For the total strain $u_{\alpha\beta}$ of Eq. A.3 we have:

$$E(\{u_{\alpha\beta}\}) = E(0) + \Omega_0\sum_{\alpha\beta}S_{\alpha\beta}u_{\alpha\beta} + \frac{\Omega_0}{2}\sum_{\alpha\beta\sigma\tau}S_{\alpha\beta\sigma\tau}u_{\alpha\beta}u_{\sigma\tau}, \tag{A.10}$$

[2] The thermodynamic potential can be, for example, the total energy E for the zero-temperature properties, the Helmholtz free-energy F for finite temperature ones and Gibbs free-energy G for finite temperature and pressure ones.

where:

$$\begin{aligned} S_{\alpha\beta} &= \frac{1}{\Omega_0}\left(\frac{\partial E}{\partial u_{\alpha\beta}}\right)_0, \\ S_{\alpha\beta\sigma\tau} &= \frac{1}{\Omega_0}\left(\frac{\partial E}{\partial u_{\alpha\beta}\partial u_{\sigma\tau}}\right)_0, \end{aligned} \tag{A.11}$$

are evaluated at zero strain $\{u_{\alpha\beta}\} = 0$. The second-order constants have only the following symmetry:[3]

$$S_{\alpha\beta\sigma\tau} = S_{\sigma\tau\alpha\beta}. \tag{A.12}$$

Similarly the Taylor expansion of a thermodynamic potential in terms of the Lagrangian strains A.9 (up to the second order term) is:

$$E(\{\eta_{\alpha\beta}\}) = E(0) + \Omega_0 \sum_{\alpha\beta} L_{\alpha\beta}\eta_{\alpha\beta} + \frac{\Omega_0}{2}\sum_{\alpha\beta\sigma\tau} L_{\alpha\beta\sigma\tau}\eta_{\alpha\beta}\eta_{\sigma\tau}, \tag{A.13}$$

where:

$$\begin{aligned} L_{\alpha\beta} &= \frac{1}{\Omega_0}\left(\frac{\partial E}{\partial \eta_{\alpha\beta}}\right)_0, \\ L_{\alpha\beta\sigma\tau} &= \frac{1}{\Omega_0}\left(\frac{\partial E}{\partial \eta_{\alpha\beta}\partial \eta_{\sigma\tau}}\right)_0. \end{aligned} \tag{A.14}$$

Both computed at $\{\eta_{\alpha\beta}\} = 0$. Now the second-order coefficients have the full symmetries:

$$L_{\alpha\beta\sigma\tau} = L_{\beta\alpha\sigma\tau} = L_{\alpha\beta\tau\sigma} = L_{\beta\alpha\tau\sigma} = L_{\sigma\tau\alpha\beta}, \tag{A.15}$$

[3]This is so because in the second order term of the expansion A.10 the matrix elements $u_{\alpha\beta}$ and $u_{\sigma\tau}$ can be commuted while the indices of the single element cannot be switched because $u_{\alpha\beta}$ is not symmetric.

because the Lagrangian strains are symmetric. By substitution of the Lagrangian strain of Eq. A.9 into the expansion A.13 we get an expansion in terms of the total strain $u_{\alpha\beta}$ with the Lagrangian constants $L_{\alpha\beta}$ and $L_{\alpha\beta\sigma\tau}$ and by comparing the terms of the same order with the expansion A.10 we have:

$$\begin{aligned} S_{\alpha\beta} &= L_{\alpha\beta}. \\ S_{\alpha\beta\sigma\tau} &= L_{\alpha\beta\sigma\tau} + L_{\beta\tau}\delta_{\alpha\sigma}. \end{aligned} \tag{A.16}$$

Hence, the first order terms (the stresses) of the two expansions are equal to each other while the second order terms are equal only when the solid is in unstrained configuration otherwise they differ by a quantity proportional to the stress.

A.2.1 Link to ab-initio calculations

In the *ab-initio* calculations the symmetric part A.6 is used. The strain changes the primitive vectors of the cell as shown in Eq. 2.27. The Taylor expansion in terms of it reads as:

$$E(\{\epsilon_{\alpha\beta}\}) = E(0) + \Omega_0 \sum_{\alpha\beta} \tilde{C}_{\alpha\beta}\epsilon_{\alpha\beta} + \frac{\Omega_0}{2} \sum_{\alpha\beta\sigma\tau} \tilde{C}_{\alpha\beta\sigma\tau}\epsilon_{\alpha\beta}\epsilon_{\sigma\tau} \tag{A.17}$$

where:

$$\begin{aligned} \tilde{C}_{\alpha\beta} &= \frac{1}{\Omega_0}\left(\frac{\partial E}{\partial \epsilon_{\alpha\beta}}\right)_0, \\ \tilde{C}_{\alpha\beta\sigma\tau} &= \frac{1}{\Omega_0}\left(\frac{\partial E}{\partial \epsilon_{\alpha\beta}\partial \epsilon_{\sigma\tau}}\right)_0. \end{aligned} \tag{A.18}$$

By substitution of Eq. A.5 into the expansion A.10, neglecting all the rotational terms and comparing with expansion A.17 we see that the initial stresses into the

three expansion are equal so, from now, the initial stress will be addressed as $\sigma^0_{\alpha\beta}$:

$$S_{\alpha\beta} = L_{\alpha\beta} = \tilde{C}_{\alpha\beta} = \sigma^0_{\alpha\beta}. \tag{A.19}$$

For the second order constants we find $\tilde{C}_{\alpha\beta\sigma\tau} = S_{\alpha\beta\sigma\tau}$. However, the $\tilde{C}_{\alpha\beta\sigma\tau}$ can be chosen more symmetric than $S_{\alpha\beta\sigma\tau}$, to have the full symmetry A.15 as a consequence of the symmetry of $\epsilon_{\alpha\beta}$ (A.6). To work out a symmetric expression for it, we start with the A.16: $\tilde{C}_{\alpha\beta\sigma\tau} = L_{\alpha\beta\sigma\tau} + \sigma^0_{\beta\tau}\delta_{\alpha\sigma}$ where the first term in the right hand side has already the whole symmetry. So, let us focus on the second term. Taking advantage of the symmetry of $\epsilon_{\alpha\beta}$ we have the following identity:

$$\sum_{\alpha\beta\sigma\tau} \sigma^0_{\beta\tau}\delta_{\alpha\sigma}\epsilon_{\alpha\beta}\epsilon_{\sigma\tau} = \frac{1}{4}\sum_{\alpha\beta\sigma\tau} \left(\sigma^0_{\beta\tau}\delta_{\alpha\sigma} + \sigma^0_{\alpha\tau}\delta_{\beta\sigma} + \sigma^0_{\beta\sigma}\delta_{\alpha\tau} + \sigma^0_{\alpha\sigma}\delta_{\beta\tau}\right)\epsilon_{\alpha\beta}\epsilon_{\sigma\tau}. \tag{A.20}$$

So, the second order constants of A.17 with the required symmetry can be written as:

$$\tilde{C}_{\alpha\beta\sigma\tau} = L_{\alpha\beta\sigma\tau} + \frac{1}{4}\left(\sigma^0_{\beta\tau}\delta_{\alpha\sigma} + \sigma^0_{\alpha\tau}\delta_{\beta\sigma} + \sigma^0_{\beta\sigma}\delta_{\alpha\tau} + \sigma^0_{\alpha\sigma}\delta_{\beta\tau}\right). \tag{A.21}$$

A.2.2 Elastic constants with stress

We consider a system with an initial stress and an initial strain $\{u_{\alpha\beta}\}$. The strained system is described by Eq. A.4 that we write with new indices for the sake of clarity in the following discussion as $x_\beta = \sum_\gamma (\delta_{\beta\gamma} + u_{\beta\gamma})X_\gamma$. This represents our new reference configuration. To obtain the elastic constants we must now apply to this system a new strain v and measure the stress, starting from the previous strained point x_β:

$$x_\alpha = \sum_\beta (\delta_{\alpha\beta} + v_{\beta\gamma})x_\beta = \sum_{\beta\gamma} (\delta_{\alpha\beta} + v_{\beta\gamma})(\delta_{\beta\gamma} + u_{\beta\gamma})X_\gamma \tag{A.22}$$

where in the last equality we made use again of Eq. A.4. So, rearranging Eq. A.22, the final system will be described by the transformation:

$$x_\alpha = \sum_\gamma (\delta_{\alpha\gamma} + w_{\alpha\gamma}) X_\gamma, \tag{A.23}$$

where w is the composition of the two strains:

$$w_{\alpha\gamma} = v_{\alpha\gamma} + u_{\alpha\gamma} + \sum_\beta v_{\alpha\beta}\ u_{\beta\gamma}, \tag{A.24}$$

and is the sum of the two strains with an additional term that couples them.

The elastic constants of a solid are defined as the derivatives of the stress with respect to the strain as presented in Eq. 2.29. Here, we find a relation between those elastic constants with the second-order energy-constants defined in the Taylor expansions of the previous section. The stress is given by:

$$\sigma_{ij}(u) = \frac{1}{\Omega(u)} \left. \frac{\partial E(w)}{\partial v_{ij}} \right|_0, \tag{A.25}$$

where $\Omega(u)$ is the volume of the reference configuration with the initial strain u and $E(w)$ is the energy of the system with both strains and its derivative is with respect to the second strain v_{ij} computed for $\{v_{ij}\} = 0$. We build $E(w)$ taking the expansion A.10 with the substitution of the strain $u \to w$ and using A.24 for $w_{\alpha\gamma}$. We get:

$$\begin{aligned} E(w) = E(0) &+ \omega_0 \sum_{\alpha\beta} \sigma^0_{\alpha\beta} \left(v_{\alpha\beta} + u_{\alpha\beta} + \sum_\gamma v_{\alpha\gamma} u_{\gamma\beta} \right) + \\ &+ \frac{1}{2} \Omega_0 \sum_{\alpha\beta\sigma\tau} S_{\alpha\beta\sigma\tau} \left(v_{\alpha\beta} + u_{\alpha\beta} + \sum_\gamma v_{\alpha\gamma} u_{\gamma\beta} \right) \left(v_{\sigma\tau} + u_{\sigma\tau} + \sum_\gamma v_{\sigma\tau} u_{\delta\tau} \right). \end{aligned} \tag{A.26}$$

Now the derivative A.25 has to be computed. After taking the derivative, all terms multiplied by v goes to zero because the derivative itself is evaluated at $v = 0$. Then we neglect the terms $\propto u^2$ because we are interested in the linear relation between stress and strain. We have:

$$\sigma_{ij}(u) = \frac{\Omega_0}{\Omega(u)} \left[\sigma^0_{ij} + \sum_{\alpha\beta} \sigma^0_{i\beta}\delta_{j\alpha}u_{\alpha\beta} + \frac{1}{2}\left(\sum_{\sigma\tau} S_{ij\sigma\tau}u_{\sigma\tau} + \sum_{\alpha\beta} S_{\alpha\beta ij}u_{\alpha\beta} \right) \right] \tag{A.27}$$

The first two terms came from the first order term of expansion A.26, the remaining part is related to the second order term whose two contributions are equal: this can be proved by renaming the summed indices and using Eq. A.12. So, we have:

$$\sigma_{ij}(u) = \frac{\Omega_0}{\Omega(u)} \left[\sigma^0_{ij} + \sum_{\alpha\beta} \sigma^0_{i\beta}\delta_{j\alpha}u_{\alpha\beta} + \sum_{\alpha\beta} S_{\alpha\beta ij}u_{\alpha\beta} \right]. \tag{A.28}$$

Since the volume of the reference system (strained with u) is, up to the first order, $\Omega(u) = \Omega_0 + \sum_{\alpha\beta} u_{\alpha\beta}\delta_{\alpha\beta}$, we have:

$$\frac{\Omega_0}{\Omega(u)} = \left(1 + \sum_{\alpha\beta} u_{\alpha\beta}\delta_{\alpha\beta} \right)^{-1} \approx 1 - \sum_{\alpha\beta} u_{\alpha\beta}\delta_{\alpha\beta}. \tag{A.29}$$

By using this expression in Eq. A.28 and, again, neglecting all terms $\propto u^2$ we get the final expression:

$$\sigma_{ij} = \sigma^0_{ij} + \sum_{\alpha\beta} \left(S_{ij\alpha\beta} - \sigma^0_{ij}\delta_{\alpha\beta} + \sigma^0_{i\beta}\delta_{j\alpha} \right) u_{\alpha\beta}. \tag{A.30}$$

The part multiplying the strain defines the elastic constants in a system with initial stress σ^0_{ij} in terms of the second derivatives of the energy with respect to strain u.

We can write it in terms of the Lagrangian ECs via Eq. A.16 and then we symmetrize with respect to the interchanges (i, j) and (α, β):

$$C_{ij\alpha\beta} = L_{ij\alpha\beta} - \frac{1}{2}\left(2\sigma^0_{ij}\delta_{\alpha\beta} - \sigma^0_{i\alpha}\delta_{j\beta} - \sigma^0_{i\beta}\delta_{j\alpha} - \sigma^0_{j\beta}\delta_{i\alpha} - \sigma^0_{j\alpha}\delta_{\alpha\beta}\right). \tag{A.31}$$

If we substitute $L_{ij\alpha\beta}$ from Eq. A.21 and rearranging the indices we get Eq. 2.33 and finally, for an isotropic pressure, Eq. 2.34 of Chapter 2.

A.2.3 Anisitropic solids: the hexagonal system

As an example of an anisotropic solid, we focus on the hexagonal system. In Voigt notation the independent elastic constants for an hexagonal solid are C_{11}, C_{12}, C_{13}, C_{33} and C_{44}. There is a further $C_{66} = \frac{1}{2}(C_{11} - C_{12})$. In the extended notation we can write the independent elastic constants as C_{1111}, C_{1122}, C_{1133}, C_{3333}, C_{2323}, respectively. Let us consider a diagonal stress with the non-zero components σ^0_{11}, $\sigma^0_{22} = \sigma^0_{11}$ and σ^0_{33}. The presence of the stress breaks the symmetry of the stress-strain elastic constants. For instance, the equivalences $C_{1133} = C_{3311}$ and $C_{1122} = C_{2211}$ are lost and the Voigt notation is not longer valid. By using Eq. 2.33 for an hexagonal solid we have:

$$
\begin{aligned}
C_{1111} &= \tilde{C}_{1111} \\
C_{1122} &= \tilde{C}_{1122} - \sigma^0_{11} \\
C_{1133} &= \tilde{C}_{1133} - \sigma^0_{11} \\
C_{2211} &= \tilde{C}_{2211} - \sigma^0_{22} \\
C_{2222} &= \tilde{C}_{2222} \\
C_{2233} &= \tilde{C}_{2233} - \sigma^0_{22} \\
C_{3311} &= \tilde{C}_{3311} - \sigma^0_{33} \\
C_{3322} &= \tilde{C}_{3322} - \sigma^0_{33} \\
C_{3333} &= \tilde{C}_{3333} \\
C_{2323} &= \tilde{C}_{2323} + \frac{1}{4}\left(\sigma^0_{11} + \sigma^0_{33}\right)
\end{aligned}
\tag{A.32}
$$

Appendix B

Zero-temperature elastic constants

Some tests of the ECs calculation by using the `thermo_pw` code can be found in Ref. [34]. In this section we investigate a few other examples. As in Ref. [13] we considered In, TiO_2 rutile, and Al_2O_3 and computed the ECs at $T = 0$ K from the second derivatives of the total energy with respect to strain (Eq. 2.32), after minimizing the total energy with respect to the crystal parameters and finding the equilibrium geometry. We also verified the result computing the ECs from the stress-strain relation (Eq. 2.29). Moreover, we computed some properties of macroscopic elasticity. In these tables we compare our results with those obtained in Ref. [13] and with the experimental data reported in the same paper.

B.0.1 Indium

We used the Wu-Cohen (WC) exchange-correlation functional [139] and the pseudopotential `In.wc-dn-kjpaw_psl.1.0.0.UPF` from `pslibrary`. The cutoff for the wave functions was 70 Ry, the one for the charge density 500 Ry, the **k**-point mesh was $48 \times 48 \times 32$. The presence of the Fermi surface has been dealt with by the

TABLE B.1: Elastic properties of indium. Crystal parameters are in units of the Bohr radius. The elastic constants C_{ij} are in kbar. Bulk modulus B (kbar), shear modulus S (kbar) and Young's modulus Y (kbar) and Poisson's ratio V are calculated within the Voigt (V) and Reuss (R) approximations. The average of the two according to the Voigt-Reuss-Hill (H) method is also reported. Transverse elastic wave velocity v_t, longitudinal elastic wave velocity v_l and the average wave velocity v_m are reported in m/s and the Debye temperature Θ_D in K.

	This work	Other theoretical	Expt.
Method	PAW-PP	FP-LAPW	
Functional	WC	WC	
a_0	6.0956	6.0491	6.1439
c_0	9.3414	9.4324	9.3479
C_{11}	617	589	525
C_{12}	302	332	368
C_{13}	424	374	371
C_{33}	500	448	530
C_{44}	70	58	78
C_{66}	54	25	147
B_V	448	421	422
B_R	448	414	422
B_H	448	418	422
S_V	78	65	92
S_R	62	50	86
S_H	70	57	89
Y_V	220	185	257
Y_R	178	143	242
Y_H	199	164	250
V_V	0.418	0.426	0.398
V_R	0.434	0.442	0.404
V_H	0.425	0.434	0.401
v_t	971	875.2	1105.2
v_l	2702	2573.2	2723.6
v_m	1103.1	995.4	1251.4
Θ_D	109	100.6	125.5

MP [41] smearing technique with a value of the smearing parameter $\sigma = 0.02$. The equilibrium configuration was obtained by interpolating the total energy computed in a 5×5 grid of a and c/a crystal parameters with a 2-dimensional fourth-degree polynomial and by minimizing it ($\Delta a = 0.05$ a.u., $\Delta(c/a) = 0.02$). The results are reported in Table B.1.

B.0.2 Rutile TiO_2

We used the Perdew-Burke-Ernzerhof (PBE) exchange-correlation functional (J. P. Perdew *et al.*,, Phys. Rev. Lett. **77**, 3865, 1996) and the pseudopotentials `Ti.pbe-spn-kjpaw_psl.1.0.0.UPF` and `O.pbe-nl-kjpaw_psl.1.0.0.UPF` from `pslibrary`. The cutoff for the wave functions was 50 Ry, the one for the charge density 350 Ry, the **k**-point mesh was $12 \times 12 \times 20$. The equilibrium configuration was obtained by interpolating the total energy computed in a 5×5 grid of a and c/a crystal parameters with a 2-dimensional fourth-degree polynomial and by minimizing it ($\Delta a = 0.05$ a.u., $\Delta(c/a) = 0.02$). The results are reported in Table C.1.

B.0.3 Rhombohedral Al_2O_3

We used the Perdew-Burke-Ernzerhof (PBE) exchange-correlation functional and the pseudopotentials `Al.pbe-nl-kjpaw_psl.1.0.0.UPF` and `O.pbe-n-kjpaw_psl.1.0.0.UPF` from `pslibrary`. The cutoff for the wave functions was 70 Ry, the one for the charge density 500 Ry, the **k**-point mesh was $12 \times 12 \times 12$. The equilibrium configuration was obtained by interpolating the total energy computed in a 5×5 grid of the lattice constant a and angle α with a 2-dimensional fourth-degree polynomial and by minimizing it ($\Delta a = 0.05$ a.u., $\Delta\alpha = 0.5$). The results are reported in Table C.2.

TABLE B.2: Elastic properties of rutile TiO_2. Crystal parameters are in units of the Bohr radius. The elastic constants C_{ij} are in kbar. Bulk modulus B (kbar), shear modulus S (kbar) and Young's modulus Y (kbar) and Poisson's ratio V are calculated within the Voigt (V) and Reuss (R) approximations. The average of the two according to the Voigt-Reuss-Hill (H) method is also reported. Transverse elastic wave velocity v_t, longitudinal elastic wave velocity v_l and the average wave velocity v_m are reported in m/s and the Debye temperature Θ_D in K.

	This work	Other theoretical	Expt.
Method	PAW-PP	FP-LAPW	
Functional	PBE	PBE	
a_0	8.7860	8.6809	8.6806
c_0	5.6138	5.5900	5.5911
C_{11}	2566	2683	2690
C_{12}	1677	1802	1770
C_{13}	1465	1464	1460
C_{33}	4693	4779	4800
C_{44}	1148	1223	1240
C_{66}	2111	2236	1920
B_V	2116	2178	2173
B_R	2012	2094	2086
B_H	2064	2136	2130
S_V	1229	1298	1246
S_R	947	978	986
S_H	1088	1138	1116
Y_V	3090	3248	3138
Y_R	2456	2538	2556
Y_H	2773	2898	2851
V_V	0.257	0.251	0.259
V_R	0.297	0.298	0.295
V_H	0.274	0.273	0.276
v_t	5133.0	5174.2	5125.8
v_l	9224.5	9272.1	9228.0
v_m	5716.2	5760.8	5709.0
Θ_D	754.7	785.6	778.5

TABLE B.3: Elastic properties of rhombohedral Al_2O_3. Crystal parameters are in units of the Bohr radius. The elastic constants C_{ij} are in kbar. Bulk modulus B (kbar), shear modulus S (kbar) and Young's modulus Y (kbar) and Poisson's ratio V are calculated within the Voigt (V) and Reuss (R) approximations. The average of the two according to the Voigt-Reuss-Hill (H) method is also reported. Transvers elastic wave velocity v_t, longitudinal elastic wave velocity v_l and the average wave velocity v_m are reported in m/s and the Debye temperature Θ_D in K.

	This work	Other theoretical	Expt.
Method	PAW-PP	FP-LAPW	
Functional	PBE	PBE	
a_0	9.0924	9.0928	8.9916
c_0	24.8081	24.8253	24.5498
C_{11}	4516	4656	4974
C_{12}	1510	1383	1640
C_{13}	1091	1036	1122
C_{33}	4537	4588	4991
C_{44}	1319	1363	1474
C_{14}	−200	−24	−236
B_V	2328	2312	2523
B_R	2325	2308	2518
B_H	2326	2310	2521
S_V	1487	1569	1660
S_R	1443	1547	1606
S_H	1465	1558	1633
Y_V	3677	3838	4084
Y_R	3587	3793	3974
Y_H	3632	3816	4029
V_V	0.237	0.223	0.230
V_R	0.242	0.226	0.236
V_H	0.240	0.224	0.233
v_t	6160.5	6355.4	6399.3
v_l	10529.9	10665.7	10853.7
v_m	6831.3	7035.3	7090.9
Θ_D	979.4	1015.3	1034.8

Appendix C

Some tests for palladium, platinum, copper and gold

C.1 Convergence tests

In this section we discuss some convergence tests of the zero-temperature ECs with respect to the energy cutoffs, smearing parameters and **k**-points meshes taking as examples the materials of Section 3.3. The ECs are computed by fitting the energy-strain data. We used 6 values of the strain: a reasonably compromise between accuracy and the need to reduce the number of phonon calculations. To fit them, a second-degree polynomial was selected that, in the previous literature, was found to be the best polynomial to give the ECs for a small set of points [140, 141]. A higher polynomial degree, like fourth, requires larger energy cutoffs to converge the ECs. We discuss below the choice of the polynomial and the interval $\Delta\epsilon$ between strained configurations. For the following tests we used $\Delta\epsilon = 0.005$ which was found to be a

good choice for many materials (see, for example, the materials of Section 3.2, those of Appendix A and Ref. [34]).

In Table C.1 the ECs as well as the lattice parameters and the bulk moduli are reported for increasing cutoffs. We started with the cutoffs needed to converge the phonon frequencies [86]. We ensure that C_{11} and C_{12} are converged within at least ≈ 20 kbar and a few kbar for the C_{44}. The chosen cutoffs are written in bold type. The tests in the tables are for the LDA functional but the final cutoffs were chosen also considering the tests with the other functionals.

With the converged cutoffs we test the smearing parameter and the **k**-points grids for each material. These tests are reported in Fig. C.1. The final set of ECs are

TABLE C.1: Convergence test of zero-temperature ECs vs. energy cutoffs with unconverged smearing parameter ($\sigma = 0.02$ Ry) and **k**-points grid ($16 \times 16 \times 16$) computed within LDA. The ECs and the bulk moduli B are in kbar. The bulk modulus is $B = \frac{1}{3}(C_{11} + 2C_{12})$.

ecut_wf (ecut_rho)	a_0	C_{11}	C_{12}	C_{44}	B
Palladium					
45(300)	7.275	2725	2071	874	2289
60(400)	7.274	2699	2062	864	2274
100(800)	7.274	2723	2069	868	2287
Platinum					
45(300)	7.373	3819	2740	891	3100
60(400)	7.373	3811	2748	892	3102
100(800)	7.372	3818	2743	892	3101
Copper					
45(1200)	6.651	2359	1651	1005	1887
60(1200)	6.651	2376	1656	1008	1896
60(1600)	6.651	2373	1660	1010	1898
100(2000)	6.651	2372	1668	1010	1903
Gold					
45(300)	7.663	2162	1846	428	1951
60(400)	7.662	2138	1860	426	1953
100(800)	7.662	2168	1842	427	1951

those obtained with the parameters declared in the paper ($\sigma = 0.005$ Ry for Pd and Pt, $\sigma = 0.02$ Ry for Cu and Au and $N_k = 40$ for all systems).

In order to further check the ECs we compute them as the derivatives of the stress with respect to the strain. For this purpose we compute directly the stress (by using the stress theorem as implemented in *QuantumESPRESSO*, see the note in Section 3.1.1) in four strained configurations around the equilibrium and then fit with respect to the strain with a second-degree polynomial and evaluate the analytic first derivative. The results are collected in Table C.2. The ECs computed within the two methods are in good agreement with differences usually less than 1%, only in the C_{11} and C_{12} ECs of Cu the differences are $\approx 2\%$ but the agreement is still satisfactory.

TABLE C.2: Comparison between ECs computed from the second derivatives of the total energy and those computed from the first derivatives of the stress with respect to the strain. We used the converged parameters discussed in Table C.1 and Fig. C.1. The functional is LDA. The ECs and the bulk moduli B are in kbar. The bulk modulus is $B = \frac{1}{3}(C_{11} + 2C_{12})$.

Method	C_{11}	C_{12}	C_{44}	B
Palladium				
Energy	2696	2071	788	2279
Stress	2705	2070	782	2282
Platinum				
Energy	3800	2759	802	3106
Stress	3788	2754	790	3099
Copper				
Energy	2349	1666	998	1894
Stress	2293	1625	998	1848
Gold				
Energy	2120	1873	373	1955
Stress	2130	1849	374	1943

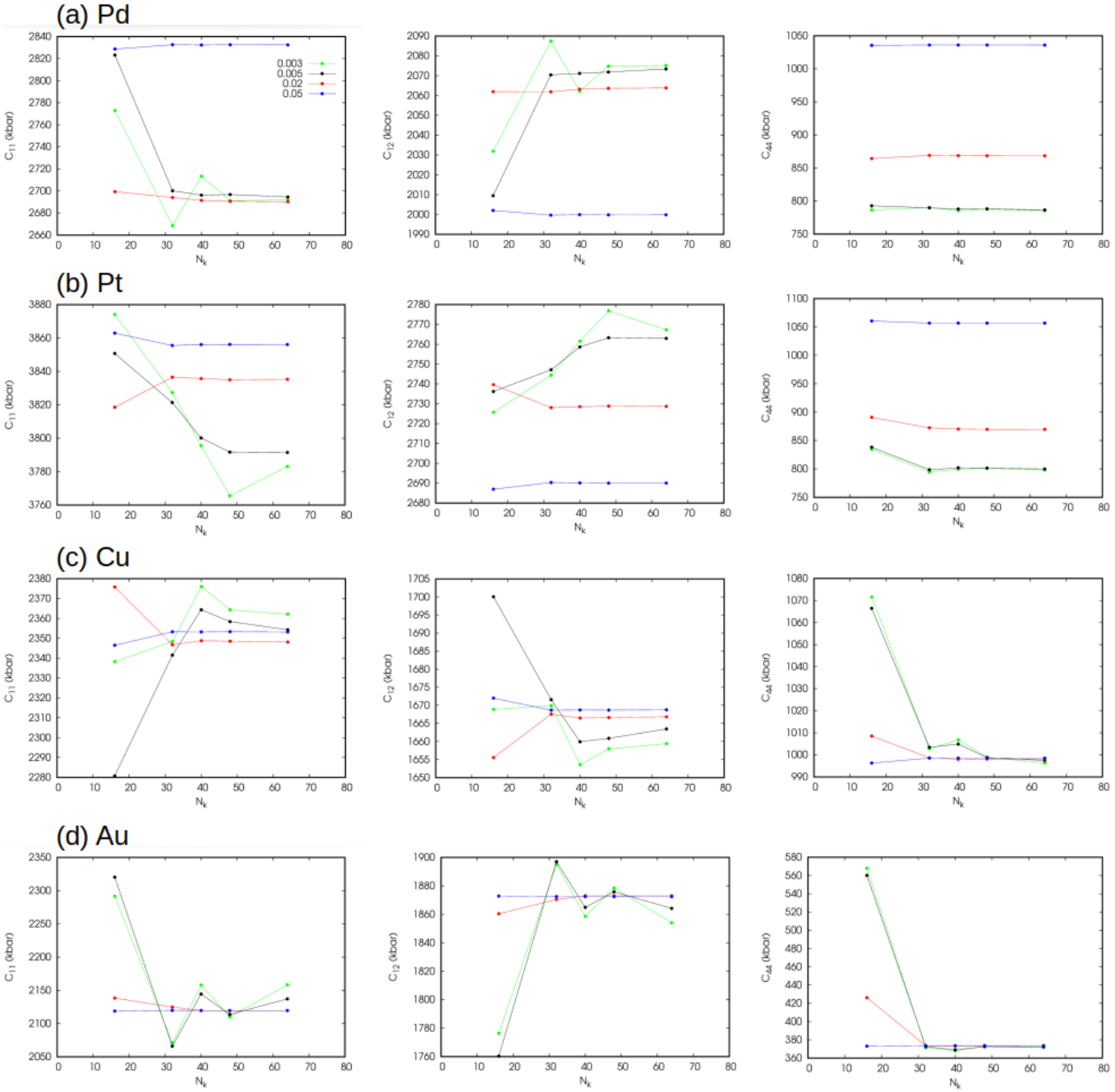

FIGURE C.1: Tests of the zero temperature ECs vs. the smearing parameters and the k-points grid $N_k \times N_k \times N_k$ for each material. The color indicates the smearing parameter: $\sigma = 0.003$ Ry (green), $\sigma = 0.005$ Ry (black), $\sigma = 0.02$ Ry (red) and $\sigma = 0.05$ Ry (blue) The final set of parameters is $\sigma = 0.005$ Ry for Pd and Pt, $\sigma = 0.02$ Ry for Cu and Au and $N_k = 40$ for all systems.

Finally, we check the parameters $\Delta\epsilon$ and the degree of the polynomial in Figure C.2. The second degree polynomial (red) provides ECs equal or very similar ECs to those computed with the third degree polynomial (green): their values are the same in a reasonably large interval of $\Delta\epsilon$ around $\Delta\epsilon = 0.005$. The fourth degree polynomial (blue) reaches the plateau for larger values of $\Delta\epsilon$. In any case the differences are usually very small, the largest differences between the second and fourth degree polynomial are found in the C_{44} ECs of Pd and Pt that are however of the order of $32 - 34$ kbar with $\Delta\epsilon = 0.005$. This difference reduces if the ECs obtained from the fourth degree polynomial are computed with a larger cutoff. For example in Pd becomes 19 kbar with a cutoff equal to 110 Ry and 800 Ry for the wave functions and charge density, respectively.

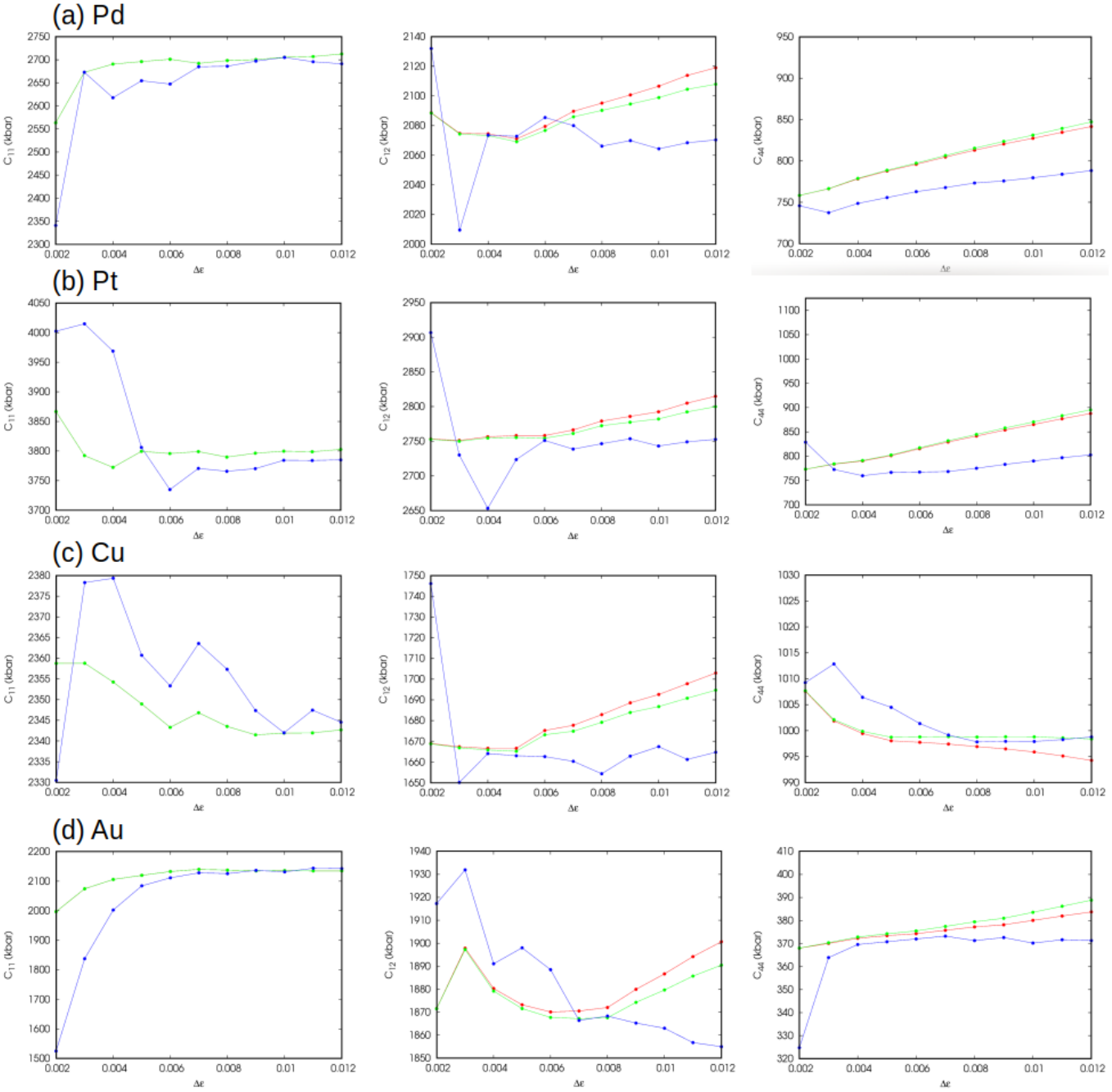

FIGURE C.2: Tests as a function of the interval $\Delta\epsilon$ between two strained configuration for each EC of each material. The number of points is fixed at 6. The maximum applied strain can be obtained as $\epsilon_{max} = 2.5\Delta\epsilon$. Second degree (red), third degree (green) and fourth degree (blue) fitting polynomials are compared. The value chosen for the calculation is $\Delta\epsilon = 0.005$.

Appendix D

Anisotropic thermal expansion at finite pressure

At finite pressure the equilibrium geometry is determined by minimizing the enthalpy H instead of the total-energy E:

$$H(X) = E(X) + P\Omega, \tag{D.1}$$

where P is the pressure and Ω the volume of the cell. For an hexagonal crystal $X = (a, \frac{c}{a})$ where a and c are the lattice parameters. Once we determine such parameters at a given pressure P we can apply the theory of Chapter 2 to address the anisotropic thermal expansion including the vibrational and electronic contributions to the free-energy. In this study we determine the equilibrium structure of hexagonal iron at different pressures from 0 to 400 GPa. Then we will address the anisotropic thermal expansion at 350 GPa.

D.0.1 Computational parameters

The pseudopotential was selected following the tests described in Ref. [43] for which `Fe.pbe-spn-rrkjus_psl.0.2.1.UPF` turns out to be the best for the α-phase of iron. The wave functions (charge density) were expanded in a plane waves basis with a kinetic energy cut-off of 90 Ry (1100 Ry), and a $24 \times 24 \times 16$ mesh of **k**-points has been used for the Brillouin zone integration. For the calculation of the anisotropic thermal expansion at 350 GPa the number of reference geometries for phonons and band structures calculations were 25 with separation between crystal parameters equal to $\Delta a = 0.052$ *a.u.* and $\Delta(c/a) = 0.022$ a.u.. The central geometry was $a = 4.00559$a.u. and $c/a = 1.59477$. DFPT [14] [54] was used to calculate the dynamical matrices on a $6 \times 6 \times 4$ **q**-points grid. The dynamical matrices have been Fourier interpolated on a $200 \times 200 \times 200$ **q**-points mesh to evaluate the free-energy. The **k**-point mesh for the electronic DOS calculations was $48 \times 48 \times 48$. We use a Gaussian smearing with a smearing parameter of 0.01 Ry.

D.0.2 Results

In Fig. D.1 the equilibrium lattice parameter a is plotted as a function of the pressure. As example, we report in the inset the minimization of enthalpy as contour lines as a function of both crystal parameters for three pressures: 50 GPa, 200 GPa, and 350 GPa. In Fig. D.2 the parameter c/a is reported as a function of the pressure and compared with experimental and theoretical data: the agreement is good with both. Finally, in Fig. D.3 we report the anisotropic thermal expansion at 350 GPa. The thermal expansion coefficient are reported with the electronic contribution in blue (α_{xx}) and light-blue (α_{zz}). This is compared with the thermal expansion computed

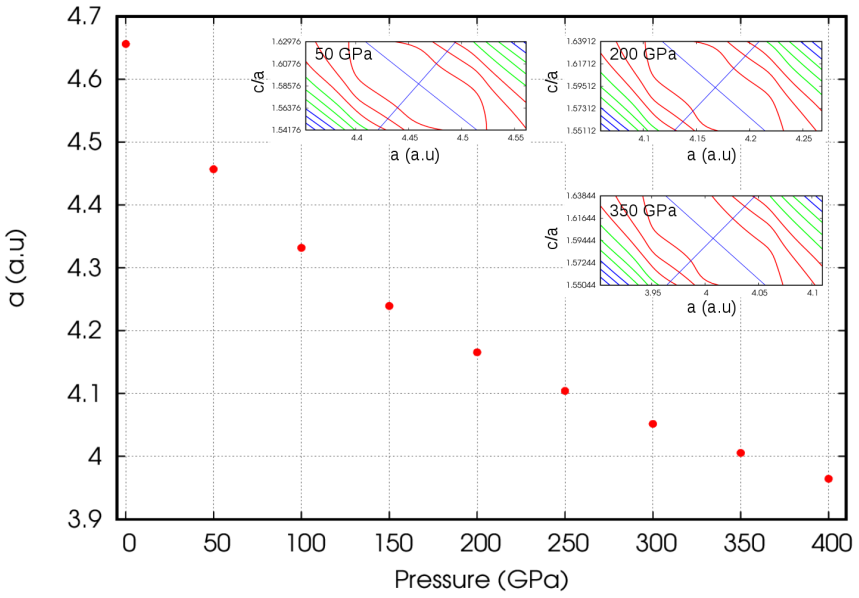

FIGURE D.1: Lattice constant a of hexagonal iron as a function of pressure. In the inset the minimization of enthalpy with respect the parameters $X = (a, c/a)$ is reported for three pressures: 50 GPa, 200 GPa, 350 GPa.

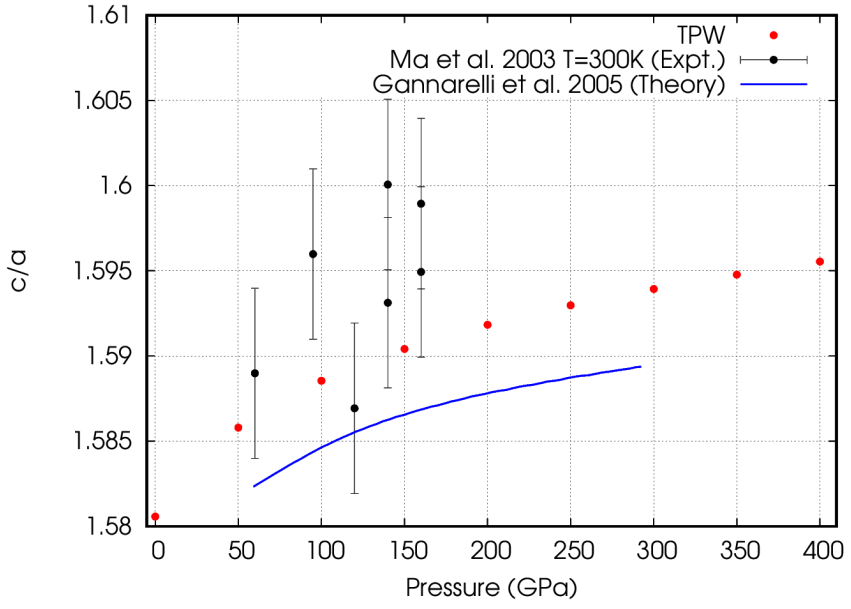

FIGURE D.2: Parameter c/a of hexagonal iron as a function of pressure (red points) compared with experiment [142] (black points) and an other theoretical calculation [143] (blue line).

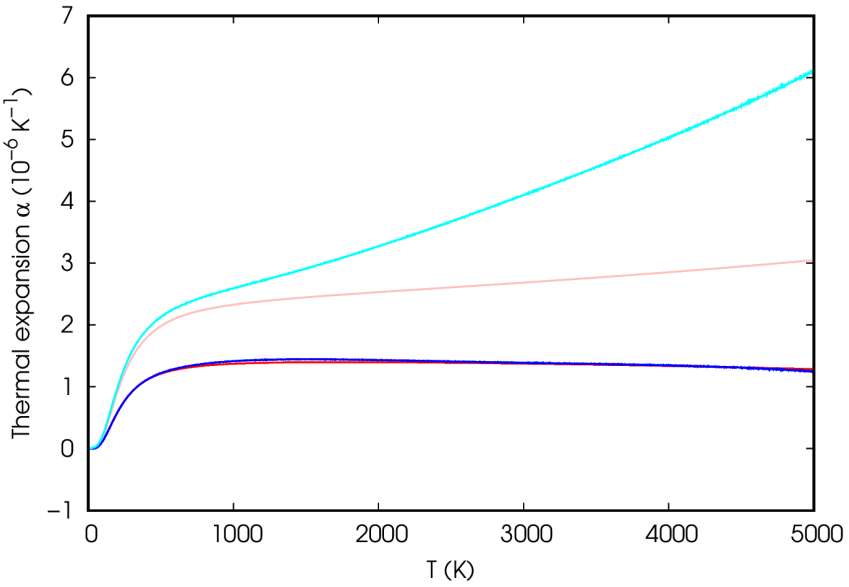

FIGURE D.3: Anisotropic thermal expansion of hexagonal iron at 350 GPa. α_{xx} is reported in red (without the contribution of the electronic free-energy F_{el}) and blue (including F_{el}), α_{zz} is reported in pink (excluding F_{el}) and light-blue (including F_{el}).

without the electronic contribution in red (α_{xx}) and pink (α_{zz}). We see that the electronic thermal excitation do not affect α_{xx}, while are crucial for α_{zz}.

References

[1] Cristiano Malica and Andrea Dal Corso. Quasi-harmonic temperature dependent elastic constants: applications to silicon, aluminum, and silver. *Journal of Physics: Condensed Matter*, 32(31):315902, may 2020. doi: 10.1088/1361-648x/ab8426. URL https://doi.org/10.1088/1361-648x/ab8426.

[2] Cristiano Malica and Andrea Dal Corso. Quasi-harmonic thermoelasticity of palladium, platinum, copper, and gold from first principles. *Journal of Physics: Condensed Matter*, 33(47):475901, sep 2021. doi: 10.1088/1361-648x/ac2041. URL https://doi.org/10.1088/1361-648x/ac2041.

[3] Cristiano Malica and Andrea Dal Corso. Temperature dependent elastic constants and thermodynamic properties of bas: An ab initio investigation. *Journal of Applied Physics*, 127(24):245103, 2020. doi: 10.1063/5.0011111. URL https://doi.org/10.1063/5.0011111.

[4] Cristiano Malica and Andrea Dal Corso. Temperature-dependent atomic B factor: an *ab initio* calculation. *Acta Crystallographica Section A*, 75(4):624–632, Jul 2019. doi: 10.1107/S205327331900514X. URL https://doi.org/10.1107/S205327331900514X.

[5] W. Kohn and L. J. Sham. *Phys. Rev.*, 140:1133, 1965.

[6] Stefano Baroni, Paolo Giannozzi, and Andrea Testa. *Phys. Rev. Lett.*, 59:2662, 1987.

[7] Xifan Wu, David Vanderbilt, and D. R. Hamann. *Phys. Rev. B*, 72:035105, 2005.

[8] Jijun Zhao, J. M. Winey, and Y. M. Gupta. *Phys. Rev. B*, 75:094105, 2007.

[9] Hao Wang and Mo Li. *Phys. Rev. B*, 79:224102, 2009.

[10] W.F. Perger, J. Criswell, B. Civalleri, and R. Dovesi. *Comput. Phys. Commun.*, 180:1753, 2009.

[11] R. Golesorkhtabar, P. Pavone, J. Spitaler, P. Puschnig, and C. Draxl. *Comput. Phys. Commun.*, 184:1861, 2013.

[12] M. Jamal, S. Jalali Asadabadi, Iftikhar Ahmad, and H.A. Rahnamaye Aliabad. *Computational Materials Science*, 95:592–599, 2014.

[13] M. Jamal, M. Bilal, Iftikhar Ahmad, and S. Jalali-Asadabadi. *J. Alloys Compd.*, 735:569, 2018.

[14] S. Baroni, S. de Gironcoli, A. Dal Corso, and P. Giannozzi. *Rev. Mod. Phys.*, 73:515, 2001.

[15] R. Car and M. Parrinello. *Phys. Rev. Lett.*, 55:2471, 1985.

[16] J. Zhuang, H. Wang, Q. Zhang, and R. M. Wentzcovitch. *Phys. Rev. B*, 103: 144102, 2021.

[17] S. Baroni, P. Giannozzi, and E. Isaev. *Reviews in Mineralogy and Geochemistry*, 71(1):39, 2010.

[18] Ethan T. Ritz and Nicole A. Benedek. *Phys. Rev. Lett.*, 121:255901, 2018.

[19] Alessandro Erba, Jefferson Maul, Raffaella Demichelis, and Roberto Dovesi. *Phys. Chem. Chem. Phys.*, 17:11670, 2015.

[20] N. Shulumba, O. Hellman, L. Rogström, Z. Raza, F. Tasnádi, I. A. Abrikosov, and M. Odén. *Applied Physics Letters*, 107(23):231901, 2015.

[21] Lorenzo Monacelli, Raffaello Bianco, Marco Cherubini, Matteo Calandra, Ion Errea, and Francesco Mauri. 33(36):363001, 2021.

[22] https://materialsproject.org.

[23] S. Curtarolo, W. Setyawan, G.L.W. Hart, M. Jahnatek, R. V. Chepulskii, R. H. Taylor, S. Wang, J. Xue, K. Yang, O. Levy, M. J. Mehl, H. T. Stokes, D. O. Demchenko, and D. Morgan. *Comput. Mater. Sci.*, 58:218, 2012.

[24] https://github.com/dalcorso/pslibrary.

[25] G. Kresse and D. Joubert. *Phys. Rev. B*, 59:1758, 1999.

[26] D. R. Hamann. *Phys. Rev. B*, 88:085117, 2013.

[27] Kevin F. Garrity, Joseph W. Bennett, Karin M. Rabe, and David Vanderbilt. *Comput. Mater. Sci.*, 81:446, 2014.

[28] N. Saunders A.P. Miodownik. *CALPHAD*. Pergamon, 1998.

[29] B. Grabowski, T. Hickel, and J. Neugebauer. *Phys. Rev. B*, 76:024309, 2007.

[30] H. L. Lukas, S. G. Fries, and B. Sundman. *Computational thermodynamics*. Cambridge University Press, 2007.

[31] https://dalcoroso.github.io/thermo_pw.

[32] P. Giannozzi, S. Baroni, N. Bonini, M. Calandra, R. Car, C. Cavazzoni, D. Ceresoli, G. L. Chiarotti, M. Cococcioni, I. Dabo, et al. *J. Phys.: Condens. Matter*, 21:395502, 2009.

[33] P. Giannozzi, O. Andreussi, T. Brumme, O. Bunau, M. Buongiorno Nardelli, M. Calandra, R. Car, C. Cavazzoni, D. Ceresoli, M. Cococcioni, et al. *J. Phys.: Condens. Matter*, 29:465901, 2017.

[34] A. Dal Corso. *J. of Phys.: Condens. Matter*, 28(7):075401, 2016.

[35] M. Palumbo and A. Dal Corso. *J. Phys.: Condens. Matter*, 29:395401, 2017.

[36] M. Palumbo and A. Dal Corso. *Phys. Status Solidi B*, 254:1700101, 2017.

[37] C. Luo, X. Deng, W. Wang, G. Shukla, Z. Wu, and R. M. Wentzcovitch. *Comput. Phys. Commun.*, 267:108067, 2021.

[38] Y Wang, J J Wang, H Zhang, V R Manga, S L Shang, L-Q Chen, and Z-K Liu. *J. Phys.: Condens. Matter*, 22:225404, 2010.

[39] S-L. Shang, H. Zhang, Y. Wang, and Z-K. Liu. *J. Phys.: Condens. Matter*, 22:375403, 2010.

[40] K. Kádas, L. Vitos, R. Ahuja, B. Johansson, and J. Kollár. *Phys. Rev. B*, 76: 235109, 2007.

[41] B. B. Karki, R. M. Wentzcovitch, S. de Gironcoli, and S. Baroni. *Phys. Rev. B*, 61:8793, 2000.

[42] T. Shao, B. Wen, R. Melnik, S. Yao, Y. Kawazoe, and Y. Tian. *J. Appl. Phys.*, 111:083525, 2012.

[43] Daniele Dragoni, Davide Ceresoli, and Nicola Marzari. *Phys. Rev. B*, 91: 104105, 2015.

[44] X. Yan, Y. Lin, L. Li, and F. Sun. *Phys. Status Solidi B*, 253:2236, 2016.

[45] L. N. Kantorovich. *Phys. Rev. B*, 51:3520, 1995.

[46] L. N. Kantorovich. *Phys. Rev. B*, 51:3535, 1995.

[47] P. Hohenberg and W. Kohn. *Phys. Rev.*, 136:864, 1964.

[48] J. P. Perdew and A. Zunger. *Phys. Rev. B*, 23:5048, 1981.

[49] J. P. Perdew, K. Burke, and M. Ernzerhof. *Phys. Rev. Lett.*, 77:3865, 1996.

[50] John P. Perdew, Adrienn Ruzsinszky, Gábor I. Csonka, Oleg A. Vydrov, G E. Scuseria, L A Constantin, Xiaolan Zhou, and Kieron Burke. *Phys. Rev. Lett.*, 100:136406, 2008.

[51] M. Methfessel and A. T. Paxton. *Phys. Rev. B*, 40:3616–3621, 1989.

[52] P. E. Blöchl. *Phys. Rev. B*, 50:17953, 1994.

[53] A. Dal Corso. *Phys. Rev. B*, 64:235118, 2001.

[54] A. Dal Corso. *Phys. Rev. B*, 82:075123, 2010.

[55] D. C. Wallace. *Thermodynamics of Crystals.* John Wiley and Sons, 1972.

[56] J. F. Nye. *Physical properties of crystals.* Oxford science publications, 1985.

[57] J. A. Rayne. *Phys. Rev.*, 118:1545, 1960.

[58] C. Weinmann and S. Steinemann. *Solid State Comm.*, 15:281, 1974.

[59] M. Yoshihara, R.B. McLellan, and F.R. Brotzen. *Acta metall.*, 35:775, 1987.

[60] S. M. Collard and R. B. McLellan. *Acta metall. mater.*, 40:699, 1992.

[61] Philipp Keuter, Denis Music, Volker Schnabel, Michael Stuer, and Jochen M Schneider. *J. Phys.: Condens. Matter*, 31:225402, 2019.

[62] Zhong-Li Liu, Jie-Hui Yang, Ling-Cang Cai, Fu-Qian Jing, and Dario Alfè. *Phys. Rev. B*, 83:144113, 2011.

[63] J. S. Kang, H. Wu, and Y. Hu. *Nano Lett.*, 17:7507, 2017.

[64] J. S. Kang, M. Li, H. Wu, H. Nguyen, and Y. Hu. *Science*, 361:575, 2018.

[65] S. Li, Q. Zheng, Y. Lv, X. Liu, X. Wang, P. Y. Huang, D. G. Cahill, and B. Lv. *Science*, 361:579, 2018.

[66] F. Tian, B. Song, X. Chen, N. K. Ravichandran, Y. Lv, K. Chen, S. Sullivan, and J. Kim. *Science*, 361:582, 2018.

[67] O. H. Nielsen and Richard M. Martin. *Phys. Rev. B*, 32:3780, 1985.

[68] R. W. G. Wyckoff. *Crystal structure 1.* Interscience Publishers New York, 1963.

[69] J. P. Perdew and Y. Wang. *Phys. Rev. B*, 45:13244, 1992.

[70] O. H. Nielsen and Richard M. Martin. *Phys. Rev. B*, 32:3792, 1985.

[71] M. Rasander and M. A. Moram. *J. Chem. Phys.*, 143:144104, 2015.

[72] Weixue Li and Tzuchiang Wang. *J. Phys.: Condens. Matter*, 10:9889, 1998.

[73] H J. McSkimin. *J. Appl. Phys.*, 24:988, 1953.

[74] G. N. Kamm and G. A. Alers. *J. App. Phys.*, 35:327, 1964.

[75] J. R. Neighbours and G. A. Alers. *Phys. Rev.*, 111:707, 1958.

[76] K. G. Lyon, G. L. Salinger, C. A. Swenson, and G. K. White. *J. Appl. Phys.*, 48:865, 1977.

[77] R. Hull. *Properties of crystalline silicon.* INSPEC London, 1999.

[78] G.-M. Rignanese, J.-P. Michenaud, and X. Gonze. *Phys. Rev. B*, 53:4488, 1996.

[79] P. M. Sutton. *Phys. Rev.*, 91:816, 1953.

[80] D. Gerlich and E. S. Fisher. *J. Phys. Chem. Solids*, 30:1197, 1969.

[81] J. L. Tallon and A. Wolfenden. *J. Phys. Chem. Solids*, 40:831, 1979.

[82] Hieu H. Pham, Michael E. Williams, Patrick Mahaffey, Miladin Radovic, Raymundo Arroyave, and Tahir Cagin. *Phys. Rev. B*, 84:064101, 2011.

[83] Y. S. Touloukian, R. K. Kirby, R. E. Taylor, and P. D. Desai. *Thermal expansion: Metallic elements and alloys.* IFI/Plenum, 1975.

[84] P. Mohazzabi. *J. Phys. Chem. Solids*, 46:147, 1985.

[85] Y. A. Chang and L. Himmel. *J. Appl. Phys.*, 37:3567, 1966.

[86] Andrea Dal Corso. *J. Phys.: Condens. Matter*, 25(14):145401, mar 2013.

[87] Tianyu Gao and John R. Kitchin. *Catalysis Today*, 312:132, 2018.

[88] V.I. Razumovskiy, E.I. Isaev, A.V. Ruban, and P.A. Korzhavyi. *Intermetallics*, 16(8):982–986, 2008.

[89] Seiji Kamada, Hiroshi Fukui, Akira Yoneda, Hitoshi Gomi, Fumiya Maeda, Satoshi Tsutsui, Hiroshi Uchiyama, Naohisa Hirao, Daisuke Ishikawa, and Alfred Q. R. Baron. *Comptes Rendus Geoscience*, 351(2-3):236, 2019.

[90] Liu Yue-Lin, Gui Li-Jiang, and Jin Shuo. 21(9):096102, 2012.

[91] Michal Jahnátek, Jürgen Hafner, and Marián Krajčí. *Phys. Rev. B*, 79:224103, 2009.

[92] Philipp Haas, Fabien Tran, and Peter Blaha. *Phys. Rev. B*, 79:085104, 2009.

[93] W. C. Overton Jr and J. Gaffney. *Phys. Rev.*, 98:969, 1955.

[94] Ge-Xing Kong, Xiao-Juan Ma, Qi-Jun Liu, Yong Li, and Zheng-Tang Liu. *Physica B: Condensed Matter*, 533:58–62.

[95] Ihsan Barin. *Thermochemical data of pure substances*. VCH (Weinheim and New York), 1995.

[96] F. Tian, K. Luo, C. Xie, B. Liu, X. Liang, L. Wang, G. A. Gamage, H. Sun, H. Ziyaee, J. Sun, Z. Zhao, B. Xu, G. Gao, X-F. Zhou, and Z. Ren. *Appl. Phys. Lett.*, 114:131903, 2019.

[97] J. S. Kang, M. Li, H. Wu, H. Nguyen, and Y. Hu. *Appl. Phys. Lett.*, 115: 122103, 2019.

[98] Xi Chen, Chunhua Li, Fei Tian, Geethal Amila Gamage, Sean Sullivan, Jianshi Zhou, David Broido, Zhifeng Ren, and Li Shi. *Phys. Rev. Appl.*, 11(6), 2019.

[99] S. Daoud, N. Bioud, and N. Bouarissa. *Mater. Sci. Semicond. Process.*, 31: 124, 2015.

[100] L. Bing, L. R. Feng, and Y. X. Dong. *Chin. Phys. B.*, 19:076201, 2010.

[101] H. Meradji, S. Drablia, S. Ghemid, H. Belkhir, B. Bouhafs, and A. Tadjer. *Phys. Status Solidi B*, 241:2881, 2004.

[102] S. Q. Wang and H. Q. Ye. *Phys. Status Solidi B*, 240:45, 2003.

[103] F El Haj Hassan, H Akbarzadeh, and M Zoaeter. *J. Phys.: Condens. Matter*, 16:293, 2004.

[104] C. Kittel. *Introduction to Solid State Physics*. Wiley, New York, 1976.

[105] H. Ma, C. Li, S. Tang, J. Yan, A. Alatas, L. Lindsay, B. C. Sales, and Z. Tian. *Phys. Rev. B*, 94:220303, 2016.

[106] R. G. Greene, H. Luo, and A. L. Ruoff. *Phys. Rev. Lett.*, 73:2476, 1994.

[107] D. A. Broido, L. Lindsay, and T. L. Reinecke. *PRB*, 88:214303, 2013.

[108] F. Benkabou, C. Chikr.Z, H. Aourag, Pierre J. Becker, and M. Certier. *Phys. Lett. A*, 252:71, 1999.

[109] S. Daoud, N. Bioud, and N. Lebga. *Chinese J. Phys.*, 57:165, 2019.

[110] K. Karch, P. Pavone, W. Windl, O. Schütt, and D. Strauch. *Phys. Rev. B*, 50: 17054, 1994.

[111] W. R. L. Lambrecht, B. Segall, M. Methfessel, and M. van Schilfgaarde. *Phys. Rev. B*, 44:3685, 1991.

[112] B. T. M. Willis and A. W. Pryor. *Thermal Vibrations in Crystallography*. Cambridge University Press, 1975.

[113] M. Schowalter, A. Rosenauer, J. T. Titantah, and D. Lamoen. *Acta Cryst.*, A65:5, 2009.

[114] H. X. Gao and L.-M. Peng. *Acta Cryst.*, A55:926, 1999.

[115] C. Lee and X. Gonze. *Phys. Rev. B*, 51:8610, 1995.

[116] M. Schowalter, A. Rosenauer, J. T. Titantah, and D. Lamoen. *Acta Cryst.*, A65:227, 2009.

[117] M. Schowalter, A. Rosenauer, and K. Volz. *Acta Cryst.*, A68:319, 2012.

[118] Anders Østergaard Madsen, Bartolomeo Civalleri, Matteo Ferrabone, Fabien Pascale, and Alessandro Erba. *Acta Cryst.*, A69:309, 2013.

[119] Janine George, Ai Wang, Volker L. Deringer, Ruimin Wang, Richard Dronskowski, and Ulli Englert. *CrystEngComm*, 17:7414, 2015.

[120] Florian F. Krause, Dennis Bredemeier, Marco Schowalter, Thorsten Mehrtens, Tim Grieb, and Andreas Rosenauer. *Ultramicroscopy*, 189:124, 2018.

[121] N. G. Krishna and D. B. Sirdeshmukh. *Acta Cryst.*, A54:513, 1998.

[122] M. Shankar Narayana, N. Gopi Krishna, and D. B. Sirdeshmukh. *Acta Cryst.*, A57:217, 2001.

[123] Y. Watanabe, H. Iwasaki, and S. Ogawa. *Jap. J. Appl. Phys.*, 10:786, 1970.

[124] W. J. A. M. Peterse and J. H. Palm. *Acta Cryst.*, 20:147, 1966.

[125] D. Vanderbilt. *Phys. Rev. B*, 41:7892, 1990.

[126] Claus Flensburg and Robert F. Stewart. *Phys. Rev. B*, 60:284, 1999.

[127] M. A. Spackman. *Acta Cryst.*, A42:271, 1986.

[128] T. Saka and N. Kato. *Acta Cryst.*, A42:469, 1986.

[129] F. Favot and A. Dal Corso. *Phys. Rev. B*, 60:11427, 1999.

[130] J. L. Warren, J. L. Yarnell, G. Dolling, and R. A. Cowley. *Phys. Rev.*, 158: 805, 1967.

[131] J. S. Reid and J. D. Pirie. *Acta Cryst.*, A36:957, 1980.

[132] R. W. G. Wyckoff. *Crystal structure 1.* Interscience Publishers New York, 1963.

[133] Nanna Wahlberg and Anders Østergaard Madsen. *J. Appl. Cryst.*, 50:1791, Dec 2017.

[134] L.-M. Peng, G. Ren, S. Dudarev, and M. Whelan. *Acta Cryst.*, A52:456, 1996.

[135] J. Arblaster. *Platinum Met. Rev.*, 57:127, 2013.

[136] B. G. Childs. *Rev. Mod. Phys.*, 25:665, 1953.

[137] J. Zhang and Jeffrey M. McMahon. *J. Mater. Sci.*, 56:4266, 2021.

[138] T. H. K. Barron and M. L. Klein. *Proc. Phys. Soc.*, 85:523, 1965.

[139] Zhigang Wu and R. E. Cohen. *Phys. Rev. B*, 73:235116, 2006.

[140] David Holec, Martin Friák, Jörg Neugebauer, and Paul H. Mayrhofer. *Phys. Rev. B*, 85:064101, 2012.

[141] Rostam Golesorkhtabar, Pasquale Pavone, Jürgen Spitaler, Peter Puschnig, and Claudia Draxl. *Computer Physics Communications*, 184(8):1861, 2013.

[142] Y. Ma, M. Somayazulu, G. Shen, H k Mao, J. Shu, and R. J. Hemley. *Phys. Earth Planet. Inter.*, 143:455, 2004.

[143] C.M. S. Gannarelli, D. Alfè, and M.J. Gillan. *Phys. Earth Planet. Inter.*, 152: 67, 2005.

[144] Erik Torrontegui, Sara Ibánez, Sofia Martínez-Garaot, Michele Modugno, Adolfo del Campo, David Guéry-Odelin, Andreas Ruschhaupt, Xi Chen, and Juan Gonzalo Muga. In *Advances in atomic, molecular, and optical physics*, volume 62, page 117. 2013.

[145] MS Stern. *IEE Proceedings J (Optoelectronics)*, 135(5):333–, 1988.

[146] MD Feit and JA Fleck. *Applied optics*, 17(24):3990, 1978.

[147] P-L Liu and B-J Li. *IEEE photonics technology letters*, 3(10):913–915, 1991.

[148] Maurizio Destefanis, Corentin Ravoux, Alessandro Cossard, and Alessandro Erba. *Minerals*, 9:16, 2019.